

Novel methods for recording and reconstructing images in digital holographic microscopy



MAYNOOTH UNIVERSITY

Xin Fan

Supervisor: Dr. Bryan Hennelly

Head of Department: Dr. Ronan Farrell

Department of Engineering
Maynooth University

This dissertation is submitted for the degree of
Doctor of Philosophy

NUIM

Mar 2019

I would like to dedicate this thesis to my loving family.

Declaration

I hereby certify that the material contained within this thesis is entirely my own work, does not to the best of my knowledge breach any law of copyright, and has not been taken from the work of others save and to the extent that such work has been cited and acknowledged within the text of my work.

Signed:

ID Number:

Date:

Xin Fan
March 2019

Acknowledgements

Undertaking this PhD has been a truly life-changing experience for me and it would not have been possible without great support from others. It has been a period of intense learning for me, not only in the scientific arena, but also on a personal level.

Primarily, I would like to thank my supervisor, Dr. Bryan Hennelly, for the patient guidance, encouragement and advice he has provided throughout my time as his student. I have been extremely lucky to have a supervisor who cared so much about my work, and who responded to my questions and queries so promptly. He has shown me, by his example, what a good scientist and person should be.

Thanks to Dr. John Healy for his encouragement and valuable suggestions and also Kevin o' Dwyer for helping with some last minute experiments. And a special thank you to Sinead Barton for all helps.

An additional thank you to all of the students, interns, and staff at Department of Electronic Engineering, who have helped make every day a brighter experience. This work would not have been possible without the financial support of the John Pat Hume scholarship, Maynooth University.

Nobody has been more important to me in the pursuit of this research project than the members of my family. I would like to thanks my parents, whose love and guidance are with me in whatever I pursue. They are the ultimate role models. And finally, a massive thank you to Shilan Lu.

Abstract

The difficulty in visualizing unstained biological cells using brightfield microscopy has resulted in the development of several specialized imaging techniques that can enhance the contrast of subcellular features without the need for labeling. Examples include phase contrast, differential interference microscopy, dark field microscopy, and Rheinberg illumination. However, these techniques are qualitative in nature and do not provide any direct measurement of cellular morphology in terms of thickness or refractive index. Quantitative phase imaging refers to a set of emerging methods with the potential to provide quantitative real-time measurement of the phase delay introduced by the specimen with nanometric accuracy and with the same spatial resolution afforded by brightfield microscopy. Quantitative phase imaging, therefore, provides a powerful means to study cellular dynamics. Several methods exist for implementing quantitative phase imaging, which include coherent approaches based on interferometry known as digital holographic microscopy.

Digital holographic microscopy is an optic-electronic technique that enables the numerical reconstruction of the complex wave-field reflected from, or transmitted through, a target with a single capture. Together with phase unwrapping, this method permits a height profile, a thickness profile, and/or a refractive index profile, to be extracted, in addition to the reconstruction of the image intensity. Digital holographic microscopy is unlike classical imaging systems in that one can obtain the focused image without situating the camera in the focal plane; indeed, it is possible to recover the complex wave-field at any distance from the camera plane. Therefore, the focus distance from the image plane to the camera plane can be estimated automatically by using a focus metric.

The aim of the work presented in this thesis is to develop novel methods for digital holographic microscopy in order to improve the quantitative analysis of cellular morphology and detect the nucleus *in vivo*, together with a number of numerical process techniques both in amplitude and phase profile. This thesis includes a number of separate contributions, some relating to novel optical systems that can be used to record the holograms, and some relating to method of processing the recorded holograms in order to generate meaningful images.

A low-cost compact portable module is proposed that can be easily integrated with a brightfield microscope in order to record quantitative phase images. This is the first of two contributions on novel methods to optically record digital holograms.

The second optical system that is proposed is a novel optical architecture for off-axis digital holographic microscopy, which allows for continuous change in magnification and numerical aperture by simply moving the sample. There are also three separate contributions that deal with numerical methods for the reconstruction of images recorded using digital holographic microscopy. The first relates to a thorough examination of the potential for sparsity metrics to be used for autofocusing in digital holographic microscopy. The last two contributions both relate to new image processing techniques for label-free color staining of subcellular features using the quantitative phase image as input. The first method is based on simulated Rheinberg illumination, while the second method is purely digital and can be related to the concept of local spatial frequency in the image. Both are shown to provide high quality color images of diatom cells.

Table of contents

List of figures	xiii
List of tables	xxi
1 Introduction	3
1.1 Microscopic imaging of biological samples	3
1.2 Digital holography: state of the art	5
1.3 Thesis outline	8
2 Background theory	13
2.1 Introduction	13
2.2 Fourier transform	13
2.3 Scalar diffraction theory	15
2.3.1 Historical introduction	16
2.3.2 The wave nature of light	17
2.3.3 Fresnel transform	17
2.3.4 Angular spectrum	19
2.4 The ray transfer matrix and its relationship to the integral transformations of wave optics	20
2.5 Phase delay of a sample	22
2.6 Digital holographic microscopy	23
2.6.1 Digital hologram recording	23
2.6.2 Sampling	25
2.6.3 In-line and off-axis DHM	25
2.6.4 Numerical reconstruction	26
2.6.5 Phase unwrapping	27
2.6.6 Focus detection	29
2.6.7 Aberration compensation	30
2.7 Digital in-line holographic microscopy	31
2.7.1 Methods for digital in-line holographic microscopy	31
2.7.2 Recording and reconstruction of an in-line digital hologram	32
2.8 Lensless microscopy	35
2.9 White light techniques	36

3	Inexpensive portable module for digital holographic microscopy	37
3.1	Introduction	37
3.2	Off-axis DHM module	40
3.2.1	Experimental System	43
3.3	Results	44
3.4	Conclusion	47
4	Off-axis DHM with continuous variable magnification, field of view and numerical aperture	49
4.1	Introduction	49
4.2	The principle of off-axis DHM with variable magnification	50
4.3	Experimental System	51
4.4	Numerical reconstruction	55
4.5	Numerical aperture, field of view, magnification	57
4.6	Results	60
4.7	Conclusion	63
5	An investigation of sparsity metrics for autofocusing in DHM	65
5.1	Introduction	65
5.2	Sparsity metrics	66
5.3	Results	69
5.3.1	Application of sparsity metrics to DHM of a diatom cell with 20× magnification	70
5.3.2	Grouping	73
5.3.3	Application of sparsity metrics to DHM of a diatom cell with 63× magnification	76
5.4	Discussion	78
5.4.1	Classification of sparsity metrics for autofocusing	80
5.4.2	Quantitative evaluations in terms of depth of field	81
5.4.3	Comparisons with the commonly used autofocusing metrics	82
5.5	Conclusion	83
6	Label-free color staining of quantitative phase images of biological cells by simulated Rheinberg illumination	85
6.1	Introduction	85
6.2	Theory of optical Rheinberg illumination	86
6.3	Digital simulation of Rheinberg illumination	90
6.3.1	The general case	91
6.3.2	The special case: simulation of optical Rheinberg illumination of the original transmittance $t(x)$	92
6.4	Results	94
6.4.1	Recording of quantitative phase images	94

6.4.2	The general case: simulation of Rheinberg illumination to complex transmittance recorded from a diatom cell with $20\times/0.4$ magnification	95
6.4.3	The general case: simulation of Rheinberg illumination to complex transmittance recorded from a diatom cell with $63\times/1.3$ magnification	101
6.4.4	The special case: simulation of optical Rheinberg illumination of the original sample	103
6.5	Discussion	107
7	Label-free color staining of quantitative phase images	109
7.1	Introduction	109
7.2	Proposed algorithm and optical analogue	110
7.2.1	Algorithm	110
7.2.2	Notes on computation	112
7.2.3	Optical analogue	113
7.3	Interpretation of the algorithm in terms of local spatial frequency	113
7.3.1	Local spatial frequencies in a microlens array	113
7.3.2	Color staining the QPI of a microlens array	115
7.4	Results	118
7.4.1	Initial results for a number of biological samples	119
7.4.2	Color coding different spatial frequencies and edge boundaries within cells	121
7.5	Conclusion	124
8	Conclusion	127
8.1	Summary of Thesis Achievements	127
8.2	Future Work	129
	References	131

List of figures

1.1	(a) Wavefront reconstruction of in-line holography. (b) Wavefront reconstruction in off-axis holography. d is the distance from image plane to camera plane; θ is the shift angle between object beam and reference beam.	6
-----	--	---

2.1	(a) (x, y, z) coordinate system for the ray \vec{k}_l . (b) (x, y, z) coordinate system for the plane wave vector \vec{k}	14
2.2	Illustration of preliminary for observing light diffraction.	16
2.3	Huygens' envelope construction.	16
2.4	The aperture plane and observation plane. (x, y) and (x_0, y_0) represent two co-ordinate systems in two planes.	17
2.5	Illustration of the limited bandwidth in the propagation.	21
2.6	Optical setup of off-axis digital holographic microscopy. MO: Microscope Object; PBS: Polarizing Beam Splitter; CCD: Charged Coupled Device Camera.	24
2.7	(a), (b),(c) and (d) show the amplitude, wrapped phase, unwrapped phase, and depth map of a quantitative phase image of a microlens array respectively, recorded using the DHM system described in Section 2.6.	28
2.8	The physical set-up is a Gabor set-up with a spherical diverging beam, $r(x)$, emerging from a pinhole, illuminating an object, $f(x)$, a distance d_1 away. Immediately behind this plane there is an object wave $o(x)r(x)$. The interference pattern, $H(x')$, between the propagated reference wave, $R(x')$, and the propagated object wave, $O(x')$, is captured on a CCD a further d_2 away. This captured pattern is the input to the numerical reconstruction part of the imaging system which is described in Section 2.7.2.	33
3.1	Optical setup of off-axis digital holographic microscopy using the common-path module proposed in this chapter. L: Lens; P: Polarizer; BS: Beam Splitter; M: Mirror; WP: Wedge Prism. The module is placed at the output port of an existing microscope and an inexpensive laser is used to illuminate the sample.	39
3.2	(a) This figure illustrates the components and light paths within the module. Two wedge-prism pairs are used to shift the object and reference beams in opposing directions in the Fourier domain. A pinhole is used to obtain a plane reference wavefield which interferes with the object wavefield on the camera face. (b) Intensity pattern recorded by the camera and (c) the discrete Fourier transform of this intensity pattern showing the separation of the twin image terms. This separation is proportional to the distance between the wedge prism pairs and can be adjusted to match any particular camera pixel size.	41
3.3	Image of the experimental setup for the off-axis DHM module proposed in this chapter. L: Lens; P: Polarizer; BS: Beam Splitter; M: Mirror; WP: Wedge prism Pair.	43

3.4	Results for a microlens array using a 20x/0.46 microscope objective. The resolution bar represents $50\mu m$. (a) and (b) are the reconstructed amplitude and phase; (c) shows the phase image recorded from a reference hologram and (d) shows the phase image of the object following aberration compensation using this reference hologram; (e) is the unwrapped phase and (f) is a three-dimensional image of the thickness profile of the object.	45
3.5	(a) phase image and (b) thickness profile of a birefringent resolution chart recorded using a 10x/0.3 MO; (c) phase image and (d) thickness profile of human cheek cells recorded using a 20x/0.46 MO; (e) phase image and (f) thickness profile of a human cheek cell with 50x/0.8 MO; in all cases the resolution bar represents $10\mu m$	46
4.1	The physical set-up shown in (a) is a Gabor set-up with a spherical diverging beam, $r(x)$, emerging from a pinhole, illuminating an object, $f(x)$, a distance d_1 away. Immediately behind this plane there is an object wave $o(x)r(x)$. The interference pattern, $H(x')$, between the propagated reference wave, $R(x')$, and the propagated object wave, $O(x')$, is captured on a CCD a further d_2 away. This capture is the input to the numerical reconstruction part of the imaging system which is described in detail later.	51
4.2	Optical setup of off-axis digital holographic microscopy with variable magnification. L: Lens; FC: Fiber Coupler; FS: Fiber Splitter; P: Polarizer; MO: Microscope Objective; TL: Tube Lens; PBS: Beam Splitter; OB: Object beam; RB: Reference beam.	52
4.3	Experimental setup of off-axis digital holographic microscopy with variable magnification in our lab.	54
4.4	Illustration of the optical system that maps the input sample plane to the output camera plane; S, Sample; C, Complex lens; MO, Microscope objective; TL, Tube lens; L, Fourier transforming convex lens. Here, the divergent spherical illumination is represented as a convex lens of focal length d in the plane immediately after the sample plane and coherent plane wave illumination is assumed.	55
4.5	The relationships between magnification M , field of view FoV and numerical aperture NA for the setup shown in Fig. 4.2; (a) shows the variation in M , FoV , and NA as a function of sample position d in the set-up; (b) M and FoV both plotted as a function of NA ; and (c) the relationship between M and NA for a range of different sensor sizes, w	58
4.6	Raw amplitude and wrapped phase images of microlens array for different magnifications.	61

4.7	Amplitude and wrapped phase image of microlens array after compensation with same magnifications shown in Fig. 4.6.	62
5.1	Hologram 1($20 \times /0.5$): the reconstructed intensity and unwrapped phase of Hologram 1 on the plane before, at, and after, the focus plane; the distances are $-12.5\mu\text{m}$, $-6.75\mu\text{m}$, and $0\mu\text{m}$ respectively. A scale bar is shown that is equal to $10\mu\text{m}$	71
5.2	Hologram 1 ($20 \times /0.5$): the intensity and phase reconstructed images of the diatom cell hologram over a range of propagation distances; the propagation distance is shown in the top left with units of μm	72
5.3	Hologram 1($20 \times /0.5$): results of 16 sparsity metrics in Table 5.1 applied to the reconstructed intensity images of the Diatom cell before and after subtraction of the smoothed signal. The blue lines are the raw autofocusing curves and the black lines are the autofocusing curves after subtraction of the smoothed signal.	73
5.4	Results for Hologram 1($20 \times /0.5$) using $I = o ^2$. Grouping of the 15 sparsity metrics in Fig. 5.3 is possible after high pass filtering. (a) Group A produces the most similar results; from top to bottom: $\frac{\ell_2}{\ell_1}$, $-\log$, Shannon Entropy, Modified Shannon Entropy, Hoyer, pq -mean, Gini index, $-\ell^p$ norm, Gaussian Entropy and ℓ_ϵ^0 ; (b) Group B contains $-\tanh_{a,b}$ and u_Θ ; (c) Group C contains those metrics that are not similar to any other metrics; from top to bottom, they are $-\ell^p$ norm, $-\ell^1$ and Kurtosis.	75
5.5	Hologram 1 ($20 \times /0.5$): the intensity and phase reconstructed images of a second diatom cell hologram over a range of propagation distances; the propagation distance is shown in the top left with units of μm	76
5.6	Hologram 2 ($20 \times /0.5$): (a) and (b) are the reconstructed intensity and unwrapped phase of a second Diatom cell. The scale bar represents $10\mu\text{m}$. (c) The result for Group A are shown for this hologram.	77
5.7	Hologram 3 ($63 \times /1.3$): the intensity and phase reconstructed images of the diatom cell hologram over a range of propagation distances; the propagation distance is shown in the top left with units of μm	78
5.8	Hologram 3 ($63 \times /1.3$): (a) and (b) are the reconstructed intensity and unwrapped phase of a diatom cell hologram. The scale bar represents $5\mu\text{m}$. (c) The results for Group A are shown, indicating two global minima as discussed in the text.	79

5.9	+ donates to the focal position detected by 32 sparsity metrics, listed in Tab. 5.3; the positions of the red line, the green line, the blue box are the mean value, median value, and the standard deviation of the focus distances detected by 32 sparsity metrics respectively; the cyan line represents the depth of field of each hologram; the magenta spots represent the focal positions detected by three commonly used auto-focusing metrics: the asterisk, cross, and circle, denote the variance of the intensity, cumulated edge detection by gradient calculation, and weighted spectral analysis respectively.	82
5.10	Results of 3 commonly used metrics applied to the reconstructed intensity images of the three holograms investigated in this chapter before and after subtraction of the smoothed signal. The blue lines are the raw results, and the black lines are the same results after subtraction of the smoothed signal.	83
6.1	(a) Illustration of optical Rheinberg illumination. Three color filters are placed at the back focal plane of the condenser lens. (b) Each of the three point sources illustrated in Fig. 6.1 (a) independently contribute to image formation. In each of these three cases image formation results from bilinear contributions from within the supports shown in the spatial frequency domain. The radius of the circular supports shown in the figure is related to the pupil function of the microscope[1]. The dashed line represents the fundamental limit of resolution.	87
6.2	Description of the algorithm that simulates optical Rheinberg illumination. Input to the algorithm is the quantitative phase image. The user selects the pinhole locations and the pupil radius for the optical microscope under simulation. A single DFT is calculated and stored for use as input to all of the remaining steps in the algorithm. For the red image this DFT is multiplied by a sequence of different binary masks, each one associated with a different point source (pinhole) in the filter plane. In each case an inverse DFT is calculated and the resultant intensity is stored. All of these intensities are superimposed to generate the final red image. The same procedure is applied for the red and green cases, each with their own set of unique pinhole positions.	93

- 6.3 Results for quantitative phase image of a diatom cell recorded with $20 \times /0.4$ MO; (a) and (b) are the intensity and phase images of the recorded complex transmittance. (c) is an illustration of the Rheinberg filter that is simulated to be in the back focal plane of a microscope condenser lens, which is made up of eight red point sources located around a centre green point source; (d) The resulting image from simulated Rheinberg illumination; (e) illustrates the filtering process that takes place in the DFT domain, for each of the independent point sources in the filter. This filtering process is illustrated in more detail in Fig. 6.4(a). 96
- 6.4 Illustration of the color filtering that takes place in simulating Rheinberg illumination. (a) The general case: this image relates to the results shown in Fig. 6.3. The DFT of the complex transmittance that is input to the color staining algorithm is shown in the figure; the signal energy is contained in the center. The simulated color filter is shown as large red and green spots in the image, which represent point sources in the spatial frequency domain that are selected by the user. The user selects the radius of the circular filters, r_s , to be applied in the DFT domain. In this simulation, $r_s = r$. For each of the red masks, only a part of the spatial frequency support of the complex transmittance will contribute to the resulting intensity. The centre positions of the red filters are chosen such that none of the red masks will overlap with the center of the DFT, which guarantees that regions with only low frequency content, such as the background will appear as green. (b) Illustrates the special case where each of the masks lies entirely within the spatial frequency support of the complex transmittance; the resulting image is shown later in Fig. 6.9 and discussed in Section 6.4.3. 97
- 6.5 Results of different simulated Rheinberg illumination applied to the same QPI shown in the previous example. The color filter used in each simulation is shown in the top left of each image, and the corresponding filters that are applied in the DFT domain are illustrated in the bottom right corner of each image. The individual parts, (a), (b), (c), and (d) are discussed in the text. The subsections from each of these images are shown in Fig. 6.6. 99
- 6.6 Sections of images taken from Fig. 6.5 allowing for clearer inspection of the color staining of subcellular features, for each of the four color filters. 100

- 6.7 Results for quantitative phase image of a diatom cell recorded with $63 \times /1.3$ MO; (a) and (b) are the intensity and phase images of the recorded complex transmittance. (c) is an illustration of the Rheinberg filter used in the simulation; (d) The color stained image; (e) Illustration of the filtering process that takes place in the DFT domain, for each of the independent point sources in the filter. . . . 102
- 6.8 Results of different simulated Rheinberg illumination applied to the same QPI shown in the previous example. The color filter used in each simulation is shown in the top left of each image, and the corresponding filters that are applied in the DFT domain are illustrated in the bottom right corner of each image. 103
- 6.9 (a) The result of color staining of the first QPI under the conditions of the special case. The color filter is shown in the top left corner and the corresponding filtering masks applied to the DFT are illustrated in the bottom right corner (note: these masks are more accurately illustrated in Fig. 6.4(b)); (b) shows a similar result except in this case a large number of green pinholes are used; due to the (partial) independence of the corresponding masks in the DFT domain, a reduction in spatial coherence is expected; (c) and (d) show the same set of results for the second QPI. 105
- 6.10 Sections taken from corresponding images shown in the previous figure, highlighting a reduction in spatial coherence (but not resolution) due to the inclusion of additional independent filters. 106
- 7.1 (a) Flowchart of the proposed algorithm. A complex valued QPI is input to a DFT operation and the resultant complex image is separately multiplied by three different real valued filter masks before an inverse DFT operation is applied to each case. The intensity of the three resultant images make up the three RGB color components of the final image. (b) An optical analogue of the proposed algorithm in which three monochromatic coherent plane waves (red, green, and blue) are incident on a hologram representing the complex valued QPI. An OFT is used to transform the QPI to the spatial frequency domain where a multi band absorption filter is located, which contains different spectral responses for the three different wavelengths. A second OFT is used to transform back to the space domain. A color camera can be used to record the final image 111

- 7.2 A set of initial results using a QPI of a microlens array (recorded using a $20 \times /0.4$ microscope objective) that assist in describing and interpreting the proposed algorithm. (a), (b), and (c) show the amplitude, unwrapped phase, and depth map of the QPI that is input to the algorithm; (d), (e), and (f) are the color stained images resulting from the filters shown in the top left of each image; (g), (h), and (i) show the same set of results for the case where the amplitude of the QPI is normalized before processing. 116
- 7.3 Results for quantitative phase image of a diatom cell recorded with $20 \times /0.4$ MO; (a) and (b) are the intensity and phase images of the recorded complex transmittance. (c) shows the result of color staining using the circularly symmetrical filter illustrated in the bottom right corner and (d) shows the result of staining using the red, green, and blue filter. The white resolution bar in part (c) signifies a length of $10\mu m$ 120
- 7.4 Results for QPIs of a variety of different biological samples; (a) is a diatom recorded using a $63 \times 1.3NA$ MO (resolution bar is $5\mu m$); (b) an insect recorded using a $2.5 \times 0.08NA$ (resolution bar is $100\mu m$); (c) a barley awn recorded using a $10 \times 0.3NA$ MO (resolution bar is $20\mu m$) and (d) a diatom cell recorded using a $20 \times 0.4NA$ MO (resolution bar is $10\mu m$). The color filters used in each case are illustrated in the bottom corner of the image. For cases (a) and (d) the inner circle in the filter has a radius of 40 samples and the outer circle has a radius of 150 samples. For cases (b) and (c) the inner circle in the filter has a radius of 20 samples and the outer circle has a radius of 150 samples. 122
- 7.5 Results for a QPI of a diatom sample containing a prominent spatial frequency; (a)-(d) show the result of four different color filters applied to the QPI is a diatom recorded using a $20 \times 0.4NA$ MO (resolution bar is $10\mu m$); The color filters used in each case are illustrated in the bottom corner of the image. For cases (a) and (d) the inner circle in the filter has a radius of 40 samples and the outer circle has a radius of 150 samples, which extends over the full support of the DFT. 123

7.6 Results of color staining applied to two QPIs of part of a diatom cell recorded using a $63 \times / 1.3$ MO (a)-(d) (resolution bar is $10\mu m$) and the legs of an insect recorded using a $10 \times / 0.3$ MO (e)-(h) (resolution bar is $20\mu m$). The color filters used in each column are illustrated in the top corner of each image in the first row. For cases (a)-(d) the inner circle in the filter has a radius of 40 samples and the outer circle has a radius of 150 samples, which extends over the full support of the DFT. For cases (e)-(h) the inner circle in the filter has a radius of 20 samples and the outer circle has a radius of 150 samples, which also extends over the full support of the DFT. . . . 125

List of tables

5.1	Full list of sparsity metrics applied in this chapter for autofocusing in digital holographic microscopy. Note these metrics are based on those found in the work of Hurley <i>et al</i> [2] , and have been adapted for two dimensional real valued images.	68
5.2	Two inputs for the metrics that are listed in Tab. 5.1.	69
5.3	The focus positions detected by the metrics that are listed in Tab. 5.1 and Tab. 5.2. Here, * denotes to the estimated focus position for each hologram based on the mean value of the results.	74
5.4	The grouping for the 32 sparsity metrics based on 10 different diatom cells recorded using the $20\times$ and $63\times$ MOs. * denotes a slight difference shown in this metric compared to others in the same group; - denotes these metrics that failed to return the focus curve and X denotes the metrics that return a global minimum at an incorrect location.	80

List of symbols and abbreviations

The following list gives a short description of the symbols and abbreviations used throughout this thesis.

*	Complex conjugate or convolution
\bar{I}	Mean value
∇^2	Laplacian
α	Shift in Fourier domain
$\alpha_l, \beta_l, \gamma_l$	Local direction cosines
α_{RN}	Pinhole position
δ	Dirac delta function
$\delta_x, \delta_y, \Delta_x, \Delta_y$	Sampling intervals
θ	Angle of incidence
λ	Wavelength
φ	Phase delay
A	Real value amplitude or angular spectrum
c	Speed of light in vacuum
CCD	Charged coupled device
<i>circ</i>	Circ function
d, z	Distance
DCG	Dichromated gelatin
DFT	Discrete Fourier transform
DIC	Differential interference contrast
DIHM	Digital in-line holographic microscopy
DHM	Digital holographic microscopy
DoF	Depth of Field
\vec{E}	Electronic field vector
$E(x, y)$	Complex optical field
f	Focal length
FFT	Fast Fourier transform
FT, F	Fourier transform
FoV	Field of view
$FQPI$	Discrete Fourier transform of the quantitative phase image
F_z	Fresnel transform
g	Complex function

GUI	Graphical user interface
h	Impulse response or coherent point spread function of the optical system
H&E	Hematoxylin and eosin stain
i	Index
I	Reconstructed 2D image intensity or magnitude
IDFT	Inverse discrete Fourier transform
I_m	Intensity pattern
j	$\sqrt{-1}$
J	Bessel function
\vec{k}	plane wave vector
k_x, k_y	Two-dimensional spatial frequency coordinates
k_{lX}, k_{lY}	Two-dimensional local spatial frequency
LED	Light Emitting Diode
InSAR	Interferometric Synthetic Aperture Radar
M	Magnification or color mask
MO	Microscope object
MRI	Magnetic Resonance Imaging
NA	Numerical aperture
N_x, N_y	Numbers of samples
o	Reconstructed complex objective wavefield
O	Complex objective wavefield
OFT	Optical Fourier transform
P	Pupil function
PBS	Polarsing beam splitter
QPI	Quantitative phase imaging
r	Radius
\vec{r}	Spatial vector
R	Complex reference wavefield
R,G,B	Red,Green,Blue
S	Intensity distribution of illumination
SLIM	Spatial light interference microscopy
t	Complex transmission function or time
TCC	Transmission cross-coefficient
TIE	Transport of intensity equation
U, U_0	complex amplitude
W	wavefront aberration

Chapter 1

Introduction

1.1 Microscopic imaging of biological samples

The nucleus of the cell is an important focal point for the cytology. For a cancerous cell the morphology of the nucleus can become larger and less uniform and it can appear darker. This physical change, resulting from altered DNA activity, can often be identified by qualitative inspection of microscopic images of the cell. Since the 1950s, the Nobel prizes in physiology or medicine are mostly awarded to scientists in the field of cell biology. The development of the cell biology relies heavily on developments in microscopic imaging. In this thesis, several new contributions are made on methods to record and process images of microscopic objects[3]. The history of the microscopic imaging begins with the British scientist, Robert Hooke who designed and built a microscope to initially observe a thin slice of oak bark. He discovered empty spaces contained by walls, and termed them “cells” in 1665. The British telescopicist, John Dollond invented the achromatic microscope in 1752. The Scottish scientist, Sir David Brewster invented the oil immersion objective in 1812. Ernst Abbe invented the apochromatic microscope and significantly improved the oil immersion objective[4]. His contributions to understanding image formation and his collaboration with the Zeiss company resulted in a leap in microscope design. His work formed the basis for the modern microscope. In the latter part of the nineteenth century, advances in optical microscopy technology and the emergence of techniques to immobilize and stain cells, enabled insight into cell microstructure and the discovery of various cell organelles. The electron microscopy technique was developed in the 1930s, further enhancing the study of cellular morphology. Max Knoll and Ernst August Friedrich Ruska proposed the initial electron microscope in 1932 and produced a commercialized electron microscope in 1940, with the resolution of $0.2nm$. Gerd Binnig and Heinrich Rohrer in Zurich Research Center invented the scanning tunneling microscope in 1981 and was awarded the Nobel prize in 1986 with the inventor of the electron microscope, Ruska. Microscopy continues to be an active area of research - recently, in 2014, Stefan Hell was awarded the Nobel

prize in chemistry for the development of stimulated emission depletion microscopy, a fluorescence based approach that enables imaging of living cells in the order of 10nm. These examples highlight the ongoing importance of the developments in microscopy to the life-science community. In the paragraphs that follow, the discussion focuses on techniques that can be used to image living cells. In many cases cells or other biological samples can appear to be effectively transparent and to compensate for this, staining is often required in order to enhance the image contrast. The cell nucleus is an important focal point for cytology; the morphology of the carcinoma nucleus can become larger, less uniform, and darker. This physical change, resulting from altered DNA activity, can often be identified by qualitative inspection of microscopic images; staining is required to enhance image contrast without which, the nucleus is difficult to identify. Labelling the nucleus is of particular importance for diagnostics as well as for basic research, and typically relies on some type of dye that binds to nucleic acids, and depending on how much distinction is needed between DNA and RNA, and whether or not the cells being labelled are live or fixed, the choice of stains will vary. Some stains, such as hematoxylin and eosin stain (H&E), will add color contrast to the nucleus, while others will fluoresce which is the basis for fluorescence microscopy. There are several methods of creating a fluorescent sample including most commonly the cell is tailored to express a fluorescent protein or sometimes a fluorescent molecule is binded to a biomolecule within the cell structure. A common goal in the area of life-science is the dynamic observation and quantitative measurement of unstained biological samples in vivo, especially cells growing on a culture on glassware. Observation of cells in real time, as they grow and multiply, and/or as they interact with drugs, significantly advances our understanding of cellular dynamics and the effect of pharmaceutical intervention. Label-free imaging of for subcellular features is, therefore, an important part of life-science imaging. In 1932, Frits Zernike designed the phase contrast microscope to observe unstained tissue and cell samples, work for which he was awarded the Nobel prize[5]. Resulting from the spatial variation in the specimens refractive index and/or thickness, transparent “phase-only” objects such as biological cells induce a spatially varying phase delay on the illuminating optical wavefield. Zernike postulated that although the cells did not absorb or scatter the light so as to render a useful intensity image, they may induce a phase delay in the wavefront of light that pass through the sample. This phase delay cannot be detected by our eyes or by using ordinary bright-field microscopy, the development of which had not changed significantly since the work of Abb in the previous century. Zernike’s phase contrast microscope utilized the diffraction and interference of the light in order to indirectly view the variation in phase delay as a variation in image intensity and, therefore, enable a direct visualization of cellular features. However, the quantitative information is still missing in the phase contrast imaging, i.e. it was not yet possible to precisely measure the exact phase delay induced at each point in the sample.

In recent years, digital holographic microscopy, and other white light quantitative phase image techniques, have shown great potential for the investigation of unstained biological cells in vivo[6–12].

1.2 Digital holography: state of the art

An overview on digital holographic microscopy can be found in Chapter 2.6. Here, we provide a brief history on the foundations of digital holography.

The technique of holography was invented by Dennis Gabor in 1948, who initially set out to improve the resolution of the electron microscope[13]. The principle of holography is to record an interference pattern between an unknown complex wavefield that has been scattered/diffracted by an object, and a known complex reference wavefield. This interference pattern encodes both the amplitude and phase information of the unknown wavefield. The complex wavefield of the object can be optically reconstructed by illuminating the photographic film on which the intensity pattern was recorded, by the same reference wavefield. Dennis Gabor and his assistant implemented the recording and reconstruction by use of a mercury lamp and he was awarded the Nobel prize in physics in 1971 for this invention. A thorough description of the set-up used by Gabor and the underlying physical and mathematical principles is provided in Section 2.7 for the specific case of recording the intensity pattern on a digital sensor and reconstructing by numerically simulating the aforementioned process of optical reply. However, it must be noted that Gabor's work was severely limited by the an in-line geometry because highly coherent light sources were not yet available. This leads to the twin images and, DC, term overlapping with the desired complex wavefield, which contribute to significant noise in the reconstructed image. The invention of the laser, a highly coherent light source, promoted a widespread application of holography. The truly important breakthrough in holography came in form of the off-axis geometry in 1962 by American scientists Emmett Norman Leith and Juris Upatnieks. Their contribution was to use a reference beam and object beam that interfered at an angle in the recording media plane when recording the hologram[14]. Therefore, the DC term and the twin images are shifted and separated in the spatial frequency domain, in an analogous fashion to frequency modulation in the area of radio communication; indeed it was this principle that inspired Emmett Norman Leith and Juris Upatnieks. In this way it became possible to separate the complex real image from the other unwanted terms in the spatial domain and the image of the object could be reconstructed clearly. The illustration of the wavefront reconstruction of inline and off-axis holography is shown in Fig. 1.1.

A traditional hologram is recorded in dichromated gelatin (DCG), silver halide or photoresist. The tedious and time-consuming process limited its application in the practical measurement. In recent years, a great numbers of novel recording materials, such as photoconductive thermoplastic plate, multiple quantum wells materials and

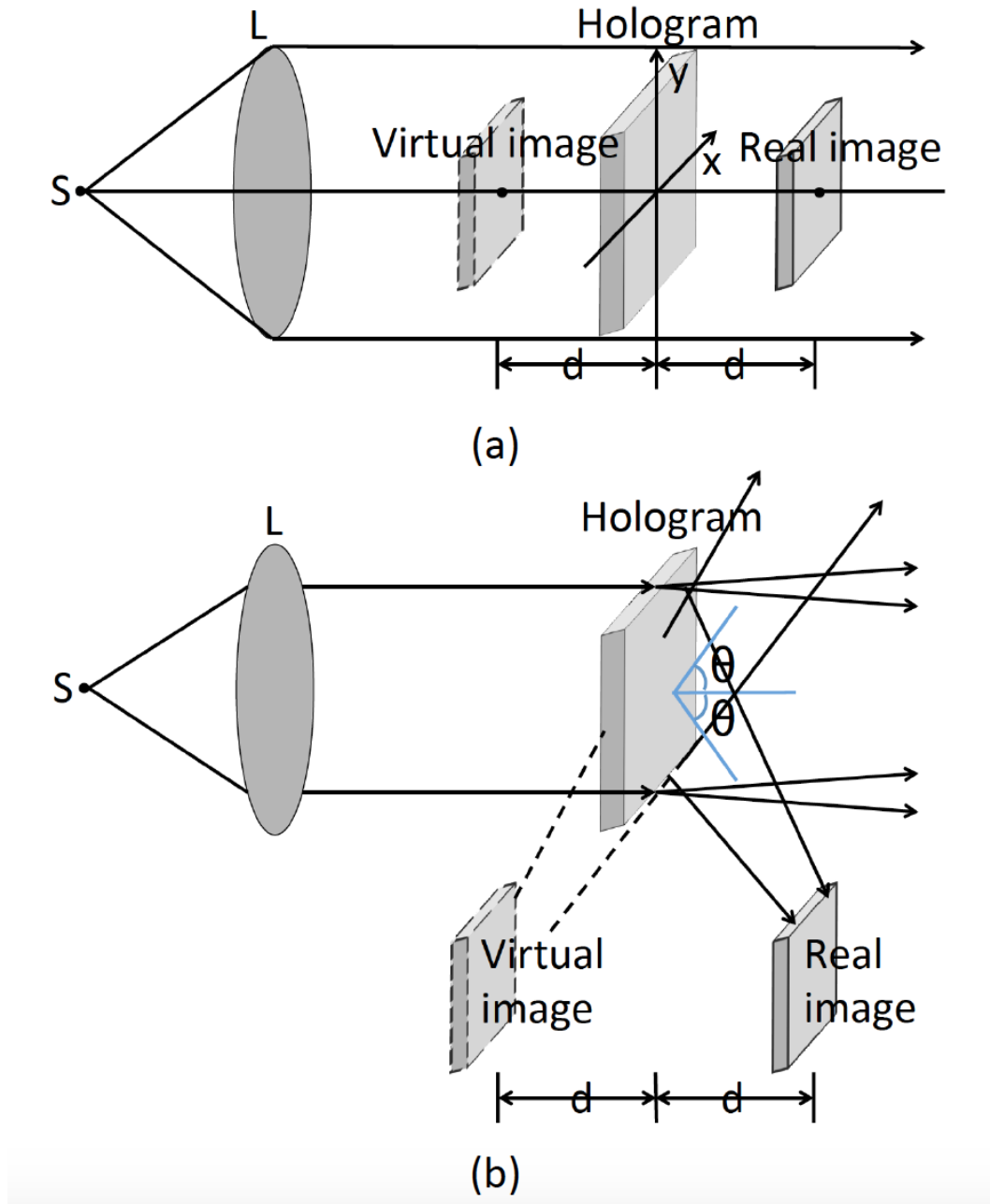


Fig. 1.1 (a) Wavefront reconstruction of in-line holography. (b) Wavefront reconstruction in off-axis holography. d is the distance from image plane to camera plane; θ is the shift angle between object beam and reference beam.

photorefractive crystal. They not only leave out the chemical process, but also have a great performance in large restore capacity and high diffraction efficiency.

Digital holography is a mixture of conventional holography, computer science and photoelectric detection technology. It is based on recording the hologram using a photoelectric detection device, such as CCD, instead of photographic materials. The digital hologram is then numerically processed to recover the complex object wave field, which is input to a numerical reconstruction algorithm that simulates the inverse of optical diffraction. The resulting reconstructed image permits access to both the phase and intensity information of the object wave field at any distance from the camera plane. The initial idea of digital holography was initially proposed in 1967 by Goodman and Lawrence[15] who were the first to record a digital Fourier hologram using a camera and to implement reconstruction using a computer. This work was extended by Yaroslavskii *et al.* in the early 1970[16]. However, it would be many decades later before a complete digital holographic setup in the modern sense of digital recording and reconstruction was achieved by Ulf Schnars and Werner J'uptner, when they introduced a high resolution CCD camera to record Fresnel holograms[17]. This development was a byproduct of the rapid development in CCD and CMOS sensors in the late 1990s and early 2000s.

As described above, digital holography differs from classical imaging systems in that it is possible to record both the intensity and phase information of an object, even when the camera is not located in the imaging plane of the system. In digital holography, a reference beam is directed towards a digital camera, where it forms an interference pattern with the diffraction pattern of an object; the latter having been illuminated by the same light source and for the case of digital holographic microscopy, this is also magnified by a microscope objective. The recorded "image" is known as a digital hologram, which is then digitally processed to recover the complex object diffraction pattern at the camera plane by using spatial filtering[18] or phase shifting techniques[19], which are discussed in more detail in Section 2.6, which provides a detailed overview of the techniques of modern off-axis digital holographic microscopy. The resulting complex image is then input to a numerical reconstruction algorithm that simulates the inverse of optical propagation in free space. This imaging modality permits the calculation of both the phase and intensity data of the object wavefield at any arbitrary distance from the plane of the camera, and therefore, the range of reconstructed distance over which digital holographic microscopy can provide an image far exceeds the traditional depth of field provided by conventional imaging systems and microscopes.

In the past decade digital holographic microscopy has become a widespread discipline of modern optics and has found many practical applications. Christian Depeursinge *et al.* measured the physiological parameters of epithelial cells, pollen, live amoebas and neuronal cells of a mouse, including the measurement of the reflective index of cells, analysis of cellular morphology using both reflective and

transmission off-axis pre-amplify digital holographic microscopy[6, 20, 7]. Bj'orn Kemper *et al.* also provided some early contributions on the analysis of biological cells using digital holographic microscopy[9, 8, 21, 10, 11, 22]. The work of Myung K. Kim *et al.* has also made several contributions in the application of digital holographic microscopy for cellular analysis[23–26]. Pietro Ferraro *et al.* in the area of phase aberration correction, lateral shear interferometry, three-dimensional color imaging, phase unwrapping and quantitative phase contrast measurement[27–29]. Bahram Javidi *et al.* proposes a great number of methods and algorithms in automatic recognition of biology tissues[30–32]. Cuhe E. *et al.* founded a company named *LyneeTec.* in 2006 and continue to develop commercialized reflective and transmission digital holographic microscopy systems.

1.3 Thesis outline

The aim of the work presented here is to develop novel methods for digital holographic microscopy in order to improve the quantitative analysis of cellular morphology and detect the nucleus in vivo by DHM, together with a number of numerical processing techniques both in the amplitude and phase profile. This thesis includes the following contributions:

1. A low-cost compact portable module is proposed in Chapter 3 that can be easily integrated with a brightfield microscope in order to record quantitative phase images. This is the first of two contributions on novel methods to optically record digital holograms.
2. A novel optical architecture is proposed in Chapter 4 for off-axis digital holographic microscopy. The proposed method allows for continuous change in magnification by simply moving the sample.
3. Chapter 5 is the first of three chapters that deal with numerical methods for the reconstruction of images recorded using digital holographic microscopy. This chapter examines the potential for sparsity metrics to be used for autofocusing in digital holographic microscopy.
4. Chapter 6 is the first of two chapters that develop new image processing techniques for label-free color staining of subcellular features. The first method is based on simulated Rheinberg illumination.
5. The final contribution is in the form of a second image processing algorithm that can be applied to quantitative phase images for the purpose of label-free color staining of subcellular features. This method is purely digital and is not based on Rheinberg illumination.

In the remaining paragraphs the various chapters are previewed with a little more detail.

Chapter 2: Background theory

Chapter 2 provides the background theory and basic experimental procedure that underpin the various contributions in this thesis. We start with a brief definition of the Fourier transform, followed by a very brief overview of scalar diffraction theory in the context of wave propagation; this includes the physical and mathematical descriptions of the angular spectrum and Fresnel transform. Various methods of quantitative phase imaging are discussed, along with the description of the phase delay of a sample. A mathematical description and configuration of a digital holographic microscopy set-up is outlined in detail; the optical system that is described is in-fact the system that was built to provide the holograms for much of the processing work that appears in Chapters 5-7. Additionally, a review of several important numerical techniques in digital holographic microscopy are described including numerical propagation, aberration compensation, and phase unwrapping.

Chapter 3: Inexpensive portable module for digital holographic microscopy

This chapter describes a novel optical system that can be integrated to the image port of an existing brightfield microscope in order to enhance the microscope with the features of digital holographic microscopy. The proposed system is relatively inexpensive and highly robust to vibrations. An additional benefit is that the system does not need to be realigned if the sample is changed, unlike several other architectures. The system was designed and constructed, as part of this thesis, and tested on a range of samples including fresh human cheek cells.

Chapter 4: Off-axis DHM with continuous variable magnification, field of view and numerical aperture

For over 100 years, microscopy set-ups have necessitated a change in magnification objective in order to image at different magnifications. In this chapter, a novel system for off-axis digital holographic microscopy is proposed that has the capability to provide for continuously variable magnification over a range of values from approximately $2\times$ up to infinity, by simply moving the position of the sample in the set-up. The basic principle of the proposed method is discussed and it was shown that the basic principles of this system are identical to the case of digital inline holographic microscopy, which is based on Gabor's original system. Unlike the in-line architecture, however, the proposed system provides full quantitative phase images in a single capture and requires no preconditions on a weakly scattering object. The

experimental system is described in detail and ray tracing is used to calculate the numerical aperture of the system for each sample position and magnification.

Chapter 5: An investigation of sparsity metrics for autofocusing in DHM

While the previous two chapters dealt with novel methods to record digital holograms, this chapter deals with processing the recorded image. It has been mentioned earlier in this introduction that digital holographic microscopy has the unique feature of a large (theoretically infinite) depth of field. Autofocus metrics can be very useful, therefore, in identifying at which depth the sample is located and then using this depth as an input parameter to the reconstruction ‘back-propagation’ algorithm. This chapter investigates the performance of a number of sparsity metrics for autofocusing in digital holographic microscopy. Sparsity metrics are often applied in signal processing for compression [33, 34] and source separation[35, 36]. We apply them to autofocusing of a range of diatom cells, magnification, and numerical apertures and demonstrate that these metrics may be grouped together according to matching behavior following high pass filtering. A core conclusion is that the variance of the image intensity is as good a metric as any that have been proposed to-date.

Chapter 6: Label-free color staining of quantitative phase images of biological cells by simulated Rheinberg illumination

This is the first of two chapters that deal with label-free color staining of subcellular features in quantitative phase images. The approach proposed in this chapter is based on numerically simulating an optical technique known as Rheinberg illumination. Rheinberg illumination, proposed almost a century ago, is an optical technique that applies color contrast to images of phase only objects by introducing a type of optical staining via an amplitude filter placed in the illumination path of a bright field microscope that consists of two or more colors. In this chapter, the complete theory of Rheinberg illumination is derived for the first time, from which an algorithm is proposed that can digitally simulate the technique. Results are shown for a number of quantitative phase images of diatom cells obtained via the digital holographic microscopy set-up that is discussed in Section 2.6. The results clearly demonstrate the potential of the technique for label-free color staining of sub cellular features.

Chapter 7: Label-free color staining of quantitative phase images

In this chapter we describe a second label-free color staining algorithm. In this case the algorithm is simpler and more efficient in design than that presented in the previous chapter. Once again this algorithm takes as input the quantitative phase image, and produces a color image in which subcellular features are clearly highlighted.

The approach is interpreted in terms of the concept of local spatial frequency and results are presented using a microlens array as well as a range of diatom cells.

Chapter 8: Conclusion

A brief conclusion is offered and suggestions are made for future work that could potentially build on the contributions presented herein.

Chapter 2

Background theory

2.1 Introduction

The aim of this chapter is to introduce and review the background theory and experimental procedures that underpin the contributions that are presented in all of the remaining chapters. We begin by very briefly defining the Fourier transform as well as the concept of the local spatial frequency in an image using the approach of Goodman[37] in Section 2.2, followed by a brief review of scalar diffraction theory in Section 2.3 where some relevant mathematical preliminaries are discussed including the angular spectrum and the Fresnel transform. We briefly review the concept of the ray transfer matrix and its relationship to wave optics in Section 4.4. The role of phase delay of a sample in quantitative phase imaging techniques is introduced in Section 2.5. This is followed by a discussion of digital holographic microscopy in Section 2.6, including the recording and reconstructing processes, in-line and off-axis DHM, phase unwrapping, focus detection and aberration compensation. An overview of digital in-line holographic microscopy is provided in Section 2.7. A general description of other quantitative phase imaging techniques is reviewed in Section 2.8 and Section 2.9.

2.2 Fourier transform

The Fourier transform has been widely used as a mathematical tool with great utility in the study of both optical and digital signal processing for both linear and nonlinear phenomena. This section provides the reader with a very brief review of the Fourier transform. More details can be found in Bracewell[38] and Goodman[37]. Our purpose here is limited to introduce a basic operational approach which is generally adopted in the following chapters. The 2D Fourier transform(FT), $F_g(k_x, k_y)$, of a complex function $g(x, y)$, may be defined in terms of the spatial frequency coordinates

k_x and k_y as follows[38, 37]:

$$F_g(k_x, k_y) = \iint_{-\infty}^{\infty} g(x, y) \exp[-j2\pi(xk_x + yk_y)] dx dy, \quad (2.1)$$

where j is defined as $\sqrt{-1}$. The complex function $g(x, y)$ can be written in terms of its real valued amplitude, $A(x, y)$, and the phase delay of the function, $\varphi(x, y)$, as follows:

$$g(x, y) = A(x, y) \exp[\varphi(x, y)], \quad (2.2)$$

The specific spatial frequencies defined by each coordinate (k_x, k_y) in the Fourier domain corresponds to a plane wave $\exp[-j2\pi(xk_x + yk_y)]$ in the spatial domain, which exists everywhere in space. However, for functions with a slowly varying phase $\varphi(x, y)$, the concept of a local spatial frequency can be introduced[37]. The local spatial frequency of the function g , which is given below as a frequency pair (k_{lX}, k_{lY}) using the same approach as Goodman[37], is defined as follows:

$$k_{lX} = \frac{1}{2\pi} \frac{\partial \varphi(x, y)}{\partial x} \quad k_{lY} = \frac{1}{2\pi} \frac{\partial \varphi(x, y)}{\partial y}, \quad (2.3)$$

k_{lX} and k_{lY} are defined to be zero in regions where the function $g(x, y)$ vanishes. This concept of local spatial frequency can in turn be related to the direction of individual rays, in terms of geometrical optics, passing through each point (x, y) . More specifically, the local direction cosines $(\alpha_l, \beta_l, \gamma_l)$ at each point (x, y) on the wavefront can be defined in term of the local spatial frequencies given in Eq. 2.3 as follows:

$$\alpha_l = \lambda k_{lX} \quad \beta_l = \lambda k_{lY} \quad \gamma_l = \sqrt{1 - \alpha_l^2 - \beta_l^2}, \quad (2.4)$$

where λ is the wavelength of the light. The inverse cosine of each of the three terms in Eq. 2.4 is equal to the angle of the geometrical ray with respect to the (x, y, z) coordinate system as illustrated for a ray of light in Fig. 2.1(a)[37].

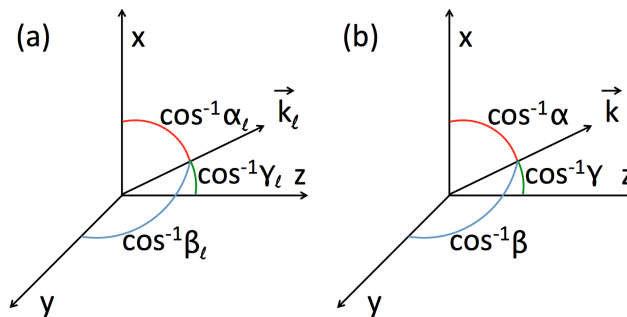


Fig. 2.1 (a) (x, y, z) coordinate system for the ray \vec{k}_l . (b) (x, y, z) coordinate system for the plane wave vector \vec{k} .

The discrete Fourier transform is defined by discretising all of the four continuous variables in Eq. 2.1. Each of these variables is sampled at integer multiples of some sampling interval over infinity

$$\begin{aligned}
 x &\rightarrow n_x \delta_x & -\infty &\rightarrow n_x \rightarrow \infty \\
 y &\rightarrow n_y \delta_y & -\infty &\rightarrow n_y \rightarrow \infty \\
 k_x &\rightarrow m_x \Delta_x & -\infty &\rightarrow m_x \rightarrow \infty \\
 k_y &\rightarrow m_y \Delta_y & -\infty &\rightarrow m_y \rightarrow \infty
 \end{aligned} \tag{2.5}$$

where δ_x , δ_y , Δ_x , and Δ_y are the sampling intervals used in the four dimensions. We assume that the support of $g(x, y)$ is limited to a region defined by $N_x \delta_x$ and $N_y \delta_y$ in the (x, y) plane, and we also assume that the support of $F_g(k_x, k_y)$ is approximately limited to $1/\delta_x$ and $1/\delta_y$ in the (k_x, k_y) plane (this is the well-known Nyquist condition). By selecting the values of the sampling intervals Δ_x , and Δ_y to be given by $1/N_x \delta_x$ and $1/N_y \delta_y$, Eq. 2.1 reduces to the form of the well-known discrete Fourier transform (DFT):

$$DFT g(n_x \delta_x, n_y \delta_y) = \sum_{-N_x/2}^{N_x/2-1} \sum_{-N_y/2}^{N_y/2-1} g(n_x \delta_x, n_y \delta_y) \exp \left[-j2\pi \left(\frac{n_x m_x}{N_x} + \frac{n_y m_y}{N_y} \right) \right], \tag{2.6}$$

The summation is limited to the N_x and N_y samples that make up the support of g and the same number of samples need only be considered for m_x and m_y . Indeed it can be shown [38] that the effect of discretization in the (k_x, k_y) plane results in an infinite periodicity in the (x, y) plane and vice versa. The DFT can be calculated in the order of milliseconds using the fast Fourier transform(FFT) algorithm[38].

2.3 Scalar diffraction theory

The phenomenon of diffraction has been defined as “*any deviation of light rays from rectilinear paths which cannot be interpreted as reflection or refraction*” by Sommerfeld in Ref.[39]. Diffraction theory is essential in order to fully understand wave propagation and the properties of optical systems. The theory of diffraction is particularly pertinent in the context of digital holographic microscopy, since the reconstruction algorithms are heavily based on simulating the inverse of diffraction, which can be more simply described as numerically ‘back-propagating’ the wave-field. This section is divided into four subsections with an emphasis on the angular spectrum and Fresnel transform.

2.3.1 Historical introduction

Diffraction was firstly reported by Grimaldi with an experiment as shown in Fig. 2.2 in the year 1665. A light source illuminated an aperture in a flat opaque object, and the diffraction pattern was observed at the plane that is some distance behind the object. The initial explanation of the diffraction effect was based on the wave theory

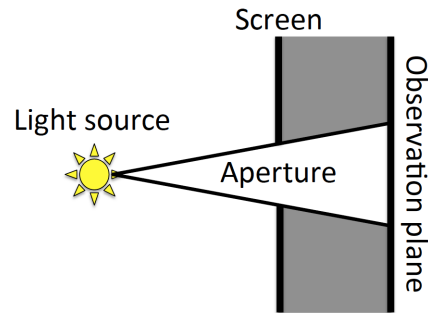


Fig. 2.2 Illustration of preliminary for observing light diffraction.

of light and was proposed by Christian Huygens in the year 1678. Huygens assumed that each point on the wavefront of the light field could be taken as a new source of secondary spherical wavelets. The superposition of these secondary spherical disturbance makes up the diffracted wavefront, as illustrated in Fig. 2.3. In 1818,

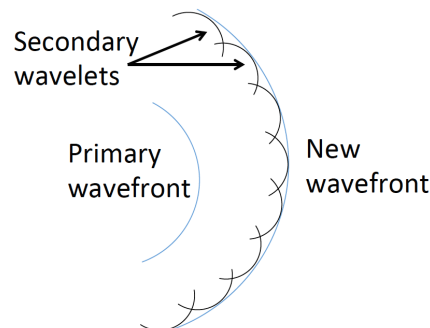


Fig. 2.3 Huygens' envelope construction.

Augustin Jean Fresnel introduced the interference principle proposed by Young into the Huygens assumption, such that the wavefront of light can be considered as the interference of coherent secondary spherical wavelets. Decades later, based on these two assumptions and building on the work of James Clerk Maxwell, Gustav Kirchhoff provided a rigorous mathematical description of the primary optical field expressed as the amplitude and phase of the secondary sources. This led to the Fresnel-Kirchhoff diffraction integral that takes into account the boundary conditions of the light incident on an obstacle surface.

The history of scalar diffraction theory is briefly reviewed in this section. Some other relevant mathematical preliminaries and physical concepts that underpin the work in this thesis are also discussed in the following sections.

2.3.2 The wave nature of light

We begin with the wave equation which can be derived from the Maxwell's equations[40]. If the vector \vec{E} is to represent the electric field at time t , it must satisfy the wave equation:

$$\nabla^2 \vec{E} - \frac{1}{c^2} \frac{\partial^2 \vec{E}}{\partial t^2} = 0, \quad (2.7)$$

where ∇^2 is operator notation for the Laplacian and c is the speed of light in vacuum. For a linearly polarized light, the electric field vibrates only in the plane that is perpendicular to the direction of propagation. Therefore, Eq. 2.7 reduces to the scalar wave equation for the case of a linearly polarized, harmonic plane wave

$$\frac{\partial^2 E}{\partial z^2} - \frac{1}{c^2} \frac{\partial^2 E}{\partial t^2} = 0, \quad (2.8)$$

According to Eq. 2.2, the modulus of the electronic field vector \vec{E} at the point with the spatial vector $\vec{r} = (x, y, z)$ at time t can be written in terms of its real valued amplitude, A , the phase delay, φ , and the angular frequency ω , as follows:

$$E(x, y, z; t) = A \exp[j(\omega t - \vec{k}\vec{r} - \varphi)], \quad (2.9)$$

The physical wave is the real part of Eq. 2.9. The wavenumber is given by the modulus of the propagation vector $|\vec{k}| = 2\pi/\lambda$.

2.3.3 Fresnel transform

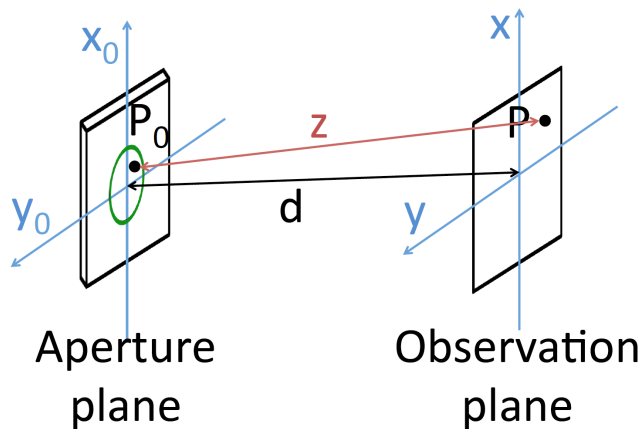


Fig. 2.4 The aperture plane and observation plane. (x, y) and (x_0, y_0) represent two co-ordinate systems in two planes.

Following on from Eq. 2.9 it is possible to derive the Frensel-Kirchoff equation. We begin with an illustration of the problem in Fig. 2.4. The complex optical field $E(x_0, y_0)$ exists at the aperture plane as the input at distance, $d = 0$, and the field $E(x, y)$ exists at the observation plane which is at some propagation distance, d . The relationship between these two fields can be described in terms of the impulse response function, $h(x, y)$, and the distance, z , from point P_0 to point P , is

$$E(x, y) = \iint_{-\infty}^{\infty} E(x_0, y_0) h(x - x_0, y - y_0) dx_0 dy_0 \quad (2.10)$$

$$h(x - x_0, y - y_0) = \frac{1}{j\lambda z} \exp(jkz),$$

Assuming the distance d from the aperture plane to observe plane is much larger than the aperture size, z can be substituted for d by the Fresnel approximation.

$$d = \sqrt{d^2 + (x - x_0)^2 + (y - y_0)^2} \approx z \left[1 + \frac{1}{2} \left(\frac{x - x_0}{d} \right)^2 + \frac{1}{2} \left(\frac{y - y_0}{d} \right)^2 \right], \quad (2.11)$$

Then, the impulse response can be rewritten as

$$h(x - x_0, y - y_0) = \frac{1}{j\lambda d} \exp(jkd) \exp \left\{ j \frac{k}{2d} [(x - x_0)^2 + (y - y_0)^2] \right\}, \quad (2.12)$$

This is the impulse response associated with the Fresnel transform. The Fresnel transform can, therefore, be described as in the same terms as the original Huygens principal. Each point in the input wavefield, contributes to a coherent spherical wave, described mathematically as a chirp function with quadratically varying phase. The amplitude and phase delay associated with each of these chirp functions depends on the amplitude and phase delay at the point of the input wavefield from which the chirp function originates. Explicitly the Fresnel transform is

$$E(x, y) = E(x_0, y_0) * h(x - x_0, y - y_0)$$

$$= \frac{1}{j\lambda d} \exp(jkd) \iint_{-\infty}^{\infty} E(x_0, y_0) \times \exp \left\{ j \frac{k}{2d} [(x - x_0)^2 + (y - y_0)^2] \right\} dx_0 dy_0, \quad (2.13)$$

where the asterisk in the above equation denotes convolution. We also note that it is possible to describe the Fresnel transform in terms of the Fourier transform as follows: Firstly move the term

$$\exp \left[j \frac{k}{2d} (x^2 + y^2) \right]$$

outside the integral sign, therefore, Eq. 2.13 can be rewritten as

$$\begin{aligned}
 E(x, y) &= F_z [E(x_0, y_0)] \\
 &= \frac{\exp jkd}{j\lambda d} \exp \left[j \frac{k}{2d} (x^2 + y^2) \right] \\
 &\quad \iint_{-\infty}^{\infty} \left\{ E(x_0, y_0) \exp \left[j \frac{k}{2d} (x_0^2 + y_0^2) \right] \right\} \exp \left[-j \frac{2\pi}{\lambda d} (xx_0 + yy_0) \right] dx_0 dy_0,
 \end{aligned} \tag{2.14}$$

where F_z denotes the operator for the Fresnel transform. It can be concluded that the Fresnel transform is based on multiplying by a quadratic phase exponential and followed by the Fourier transform. In this thesis the discrete version of Fresnel transform is involved in the numerical reconstruction algorithm. This is discussed in more detail in Section 2.6.4 in which it is pointed out that the Fresnel transform can also be described as a multiplication with a chip function in the Fourier domain, which forms the basis of the preferred numerical algorithm for simulating the Fresnel transform that is used in this thesis. Both forms in Eq. 2.13 and Eq. 2.14 are defined as Fresnel diffraction integral. The reader is referred to Chapter 4 in Ref.[1] for more information of Fresnel transform.

2.3.4 Angular spectrum

The description in the previous section lays the foundation for what is known as ‘scalar diffraction theory’. Alternatively, diffraction can be considered as a linear combination given by numerous monochromatic plane-wave components, propagating in different directions. Conceptually this is a very useful description of diffraction and is important in the context of later chapters, in particular the work on mathematically describing Rheinberg illumination.

Given the complex optical field $E(x, y; 0)$ at $d = 0$, the angular spectrum of this field can be defined by a two-dimensional Fourier transform, as defined in Section 2.2 in terms of the direction cosines (α, β, γ) , which are illustrated in Fig. 2.1(b)

$$A \left(\frac{\alpha}{\lambda}, \frac{\beta}{\lambda}; 0 \right) = \iint_{-\infty}^{\infty} E(x, y; 0) \exp \left[-j2\pi \left(\frac{\alpha}{\lambda} x + \frac{\beta}{\lambda} y \right) \right] dx dy, \tag{2.15}$$

If the direction cosines (α, β) of the plane wave components in the $E(x, y; d)$ field satisfy

$$\alpha^2 + \beta^2 < 1, \tag{2.16}$$

after propagation over a distance d , the angular spectrum of each component can be written in the form

$$A \left(\frac{\alpha}{\lambda}, \frac{\beta}{\lambda}; d \right) = A \left(\frac{\alpha}{\lambda}, \frac{\beta}{\lambda}; 0 \right) \exp \left(j \frac{2\pi}{\lambda} d \sqrt{1 - \alpha^2 - \beta^2} \right), \tag{2.17}$$

This result demonstrates that each plane-wave component travels at a different angle between two parallel planes; therefore, each of them has different propagation distances, no longer equal to d . This leads to the relative phase delay of the angular spectrum. However, in the case of $\alpha^2 + \beta^2 > 1$, Eq. 2.17 can be written as

$$A\left(\frac{\alpha}{\lambda}, \frac{\beta}{\lambda}; d\right) = A\left(\frac{\alpha}{\lambda}, \frac{\beta}{\lambda}; 0\right) \exp(-\mu d) \quad (2.18)$$

$$\mu = \frac{2\pi}{\lambda} \sqrt{\alpha^2 + \beta^2 - 1},$$

Note that these wave components which outside the region defined in Eq. 2.16, are commonly referred to as evanescent waves, are rapidly attenuated during propagation, which is illustrated further in Eq. 2.19. As it can be seen, by applying the inverse transform of Eq. 2.18, the disturbance of the $E(x, y; d)$ field can be expressed in terms of the initial angular spectrum as follows:

$$E(x, y; d) = \iint_{-\infty}^{\infty} A\left(\frac{\alpha}{\lambda}, \frac{\beta}{\lambda}; 0\right) \exp\left(j\frac{2\pi}{\lambda} \sqrt{1 - \alpha^2 - \beta^2} d\right) \times \text{circ}\left(\sqrt{\alpha^2 + \beta^2}\right) \exp\left[j2\pi\left(\frac{\alpha}{\lambda}x + \frac{\beta}{\lambda}y\right)\right] d\frac{\alpha}{\lambda} d\frac{\beta}{\lambda}, \quad (2.19)$$

where the *circ* function describes a cutoff spatial region as defined in Eq. 2.16. This leads to a linear spatial filter with a finite bandwidth in the propagation phenomenon. Furthermore, wave components beyond the circular region of radius $\frac{1}{\lambda}$ in the frequency plane as shown in Fig. 2.5, are zero. Thus, within the frequency bandwidth mentioned above, wave components comprise a circular distribution of the $E(x, y; d)$ field; the modulus of each is still unity, but phase shifts are independently introduced in the Fourier domain. This is a basis for the later simulated Rheinberg illumination in Chapter 6.

2.4 The ray transfer matrix and its relationship to the integral transformations of wave optics

In this section, we briefly review the concept of the ray transfer matrix, also known as the *ABCD* ray transfer matrix, which can be used to trace the direction and position of a geometrical ray as it passes through an optical system[1]. Each optical element in a complex optical system, including a section of free space, can be assigned an *ABCD* matrix. The overall *ABCD* ray transfer matrix for the entire system is given by the product of these individual matrices in the order in which they act on the input ray. The *ABCD* matrix will be used in Section 4.4 in Chapter 4 in order to (i) understand the magnification that results from a diverging spherical wave as well as to identify a suitable reconstruction algorithm for a novel digital holographic

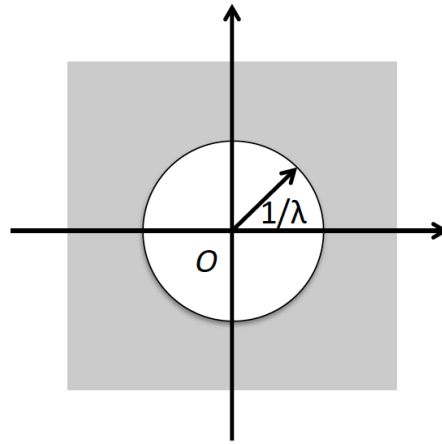


Fig. 2.5 Illustration of the limited bandwidth in the propagation.

microscope optical system and (ii) to estimate the numerical aperture and field of view of that system by tracing rays through the system and identify the maximum ray angle from the object that can be captured by the recording camera. In order to illustrate the concept of the ray transfer matrix we must first familiarise ourselves with simple examples that form the basis of later analysis:

$$\begin{bmatrix} A & B \\ C & D \end{bmatrix} = \begin{bmatrix} 1 & \lambda z \\ 0 & 1 \end{bmatrix}, \quad (2.20a)$$

$$\begin{bmatrix} A & B \\ C & D \end{bmatrix} = \begin{bmatrix} M & 0 \\ 0 & 1/M \end{bmatrix}, \quad (2.20b)$$

$$\begin{bmatrix} A & B \\ C & D \end{bmatrix} = \begin{bmatrix} 0 & 1 \\ -1 & 0 \end{bmatrix}, \quad (2.20c)$$

$$\text{and } \begin{bmatrix} A & B \\ C & D \end{bmatrix} = \begin{bmatrix} 1 & 0 \\ 1/\lambda f & 1 \end{bmatrix}. \quad (2.20d)$$

These four matrices represent the $ABCD$ ray transfer matrices for (i) propagation in free space (equivalent to a Fresnel transform acting on a complex wavefield in the paraxial approximation), (ii) a magnification system (scaling), (iii) a Fourier transform and (iv) a lens where λ is the wavelength, z is the propagation distance, M is a magnification factor and f is the focal length of the lens[1, 41]. It has been shown by Collins[41] that the integral transformation that acts on a complex optical wavefield, which represents the physical effect that relates the input and output

planes of the system, is given by the following equation:

$$F_{ABCD}[g(x)](x') = 1/\sqrt{-j\lambda B} \int_{-\infty}^{+\infty} g(x) \exp\{[j\pi(Ax^2 - 2xx' + Dx'^2)]/(\lambda B)\} dx. \quad (2.21)$$

It is clear that substituting the A , B , C , and D parameters for free space propagation into Equation 2.21 produces the Fresnel transform, see Eq. 2.14 in Section 2.3.3. Using this simple relationship between geometrical optics and waveoptics it is possible to quickly define the transformation integral associated with any optical system; firstly the overall $ABCD$ matrix can be determined, following which the integral transformation can be determined. We refer the reader to [42–44] for a graphical interpretation of these effects based on the Wigner distribution function. We also note that in [42] a method for inventing and investigating new algorithms was proposed for calculating the integral transformation associated with a given optical system. Each ray transfer matrix can be associated with a particular numerical process, eg. the discrete Fourier transform is associated with the Fourier matrix above in Eq. 2.20c. Using this approach the sampling requirements at each step in the algorithm can also be deduced.

2.5 Phase delay of a sample

As discussed in Section 1.1, unstained objects such as biological cells present a unique problem for the light microscopist because their images generate very little contrast and are essentially invisible in ordinary bright-field microscopy[45, 46]. Transparent ‘phase-only’ objects such as biological cells induce a spatially varying phase delay on the illuminating optical wavefield; this phase delay results from spatial variation in the specimen’s refractive index and/or thickness. Phase-only objects remain nearly invisible in the image plane of the microscope, because physical detectors such as the eye, or a camera, cannot detect variation in phase. The diffraction pattern resulting from the phase delay introduced by the sample can be observed in other defocused planes, but such an approach renders the image difficult to interpret[45]. Several specialized imaging techniques[45, 46, 5, 47–57] are commonly employed in light microscopes in order to enhance image contrast and enable a direct visualization of sub cellular features (as well as other types of samples that induce small phase delays) without staining, such as dark field[45, 46], phase contrast[5, 47, 48], differential interference contrast[49–51] (DIC), fluorescence[52, 53], and Rheinberg illumination[54–57]. By exploiting refraction, diffraction, interference, or fluorescence, these methods are applied mainly to make visible objects such as cells and other biological structures that are otherwise invisible. Compared to bright field microscopy, the optical images produced with such contrast techniques usually provide an unnatural appearance to the observed specimens. However, these approaches

have become an essential set of tools for modern life science and material science research.

Techniques such as phase contrast[5, 47, 48] and DIC[49–51] effectively enhance the contrast in images of phase-only objects. However, the information obtained with these techniques is essentially qualitative. Quantitative phase imaging (QPI)[58, 59] provides a powerful means to study cellular dynamics associated with both thickness and refractive index fluctuations. QPI refers to a set of techniques that are capable of recording an accurate quantitative measurement of the phase delay imparted by the sample, and therefore provide the complex transmittance of the sample. For a more detailed description of the various QPI techniques can be found in the next sections. It is notable that this set of techniques includes digital holographic microscopy (DHM)[18, 19, 6, 60, 61, 8, 62, 7, 9], which makes use of a temporally coherent source to record an interference pattern between the image of the sample and a known reference wave field.

2.6 Digital holographic microscopy

As described in Section 1.2, DHM[6–12] has been found particular suitable for simplified quantitative phase imaging of living cells. In this section we briefly review the theory of digital holography as well as the basic construction of the digital holographic microscope in our lab, with an emphasis on the recording and reconstruction processes and several numerical techniques involved in DHM.

2.6.1 Digital hologram recording

Digital holography is based on the recording of an optical interference pattern on a digital camera. A laser source is split into two paths using a beamsplitter; in the first path the laser illuminates an object, which diffracts the light to form an object wavefield; the second path is used to generate a plane wave reference wavefield. Both wavefields are combined by a second beamsplitter and are coincident on a digital camera. The recorded intensity pattern is given by

$$\begin{aligned} I_m(x,y) &= |O(x,y) + R(x,y)|^2 \\ I_m(x,y) &= |O(x,y)|^2 + |R(x,y)|^2 + O(x,y)R^*(x,y) + O^*(x,y)R(x,y) \end{aligned} \quad (2.22)$$

where I_m , O , and R represent the intensity pattern, the complex object wavefield, and the complex reference wavefield at the camera plane, and x and y denote the spatial coordinate system. Extension to discrete variables is discussed later in this continuous section. The accents used in the equation denote the complex conjugate. For simplicity, phasor notation is employed in the mathematical description in this chapter since only the scalar field is of interest. In Fig. 3.1 the optical set up that is custom built in our laboratory is illustrated; in this case a partially coherent laser

diode source (CNI Laser MGL-III-532) operating at a power of 100 *mW* and with a wavelength of 532 *nm* is coupled to a single mode optical fiber (FC532-50B-FC) which splits into two output fibers with a 50/50 power ratio. The first fiber output is collimated by a plano convex lens and passes through a linear polariser and a condenser lens to illuminate the sample. The resultant wavefield then passes through a microscope objective, a tube lens, and a relay doublet to form an image on a plane a short distance in front of the camera (Allied Vision Technology). The second fiber is used to generate the reference; the output of the fiber is collimated and polarised as for the case of the object wavefield. Both wavefields are combined using a polarising beam splitter (PBS) and a third linear polariser is used immediately before the camera to ensure high hologram diffraction efficiency. All optical elements were obtained from Thorlabs with anti-reflection coating for the visible region. The coherence length of the laser is approximately 0.1 *mm*, which ensures that noise from back reflections is reduced; this requires that the path lengths are suitably matched, which is achieved by using different fiber lengths for both paths. By ensuring that the

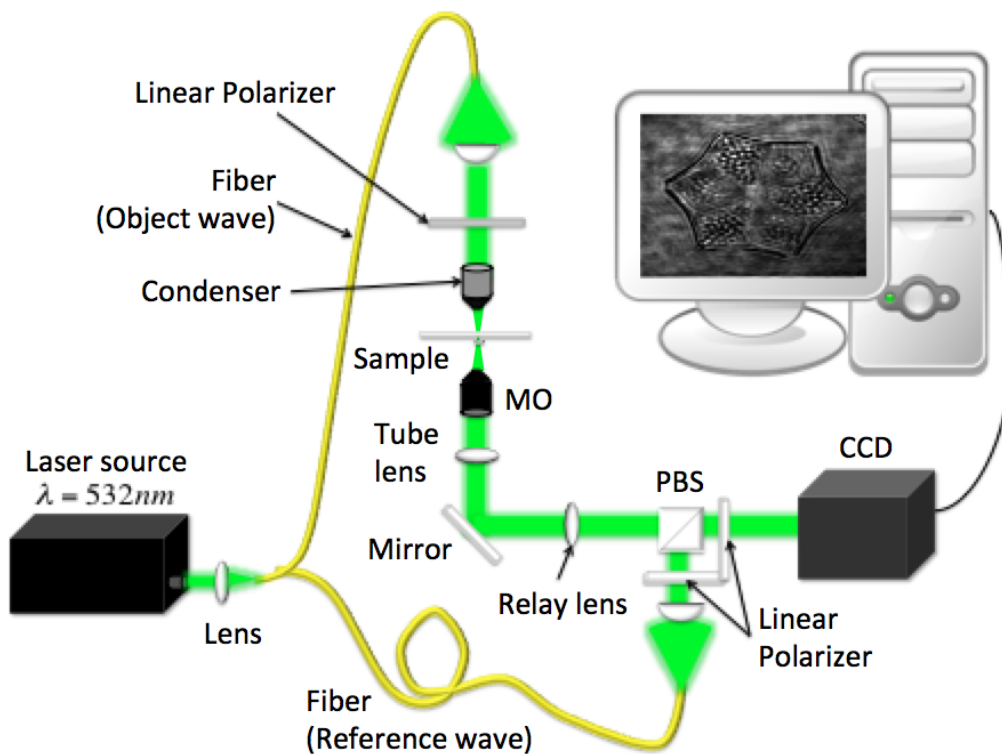


Fig. 2.6 Optical setup of off-axis digital holographic microscopy. MO: Microscope Object; PBS: Polarizing Beam Splitter; CCD: Charged Coupled Device Camera.

reference wave is a plane wave that is propagating at a small angle with respect to the camera normal, as described by the equation below:

$$R(x,y) = \exp(j2\pi[x\sin(\theta_x) + y\sin(\theta_y)]/\lambda), \quad (2.23)$$

where θ_x and θ_y denote the angles with respect to the camera normal in both the x and y directions respectively, and λ denotes the laser wavelength, it can be shown that the latter two terms in Eq. 2.22 become separated from the other terms in the spatial frequency domain[1] and can be isolated by filtering. This is possible if the support of O in the spatial frequency domain is sufficiently limited and the frequency shift imparted by the angle of the reference is sufficiently large; for more details see Chapters 6 and 9 of Goodman[1].

2.6.2 Sampling

All of the variables in the description thus far are continuous. However, the pixelated nature of the camera ensures that these variables can take only discrete values:

$$\begin{aligned} x &= n_x \delta x & n_x &= -N_x/2 \rightarrow N_x/2 - 1 \\ y &= n_y \delta y & n_y &= -N_y/2 \rightarrow N_y/2 - 1 \end{aligned} \quad (2.24)$$

where δx and δy denote the pixels pitch of the camera, which contains N_x and N_y pixels in the x and y directions respectively. Assuming the Nyquist sampling rate is satisfied[1], such that the pixel pitch is less than the inverse of the spatial frequency support of I_m in both the x and y dimensions respectively, the discrete Fourier transform[38] may be applied to the recorded intensity pattern in order to perform the aforementioned spatial filtering using an FFT[38]. The resulting discrete complex image, $O(n_x \delta x, n_y \delta y)$, is often termed a digital hologram.

2.6.3 In-line and off-axis DHM

Digital holography can also be implemented using phase shifting[19], whereby an in-line plane wave reference can be used, i.e. $\theta_x = \theta_y = 0$. In this case the four terms in Eq. 2.22 overlap in the spatial frequency domain. However, $O(n_x \delta x, n_y \delta y)$ can be isolated by recording a sequence of interference patterns whereby a different constant phase shift is introduced into the reference beam in each instance; $O(n_x \delta x, n_y \delta y)$ can then be estimated by solving a set of simultaneous equations for each pixel[19]. The advantage of this approach is that the spatial frequency support of the recovered object wavefield can be significantly greater than that recorded by the off-axis approach described above; the latter requires that we ensure the imaging system produces a sufficiently low frequency object wavefield. In the case of DHM, this is achieved by taking into account the numerical aperture of the microscope objective and the magnification of the overall imaging system, as well as the camera pixel pitch, the result of which is a sacrifice in spatial field. A thorough review of other twin removal techniques can be found in Hennelly *et al.*[63]. Although more limited in terms of bandwidth, the off-axis approach has the distinct advantage of allowing for the recording of dynamic events, as only a single recording is necessary. This

advantage is especially true for the imaging of quickly varying scenes in which the object moves or changes shape appreciably in the axial direction, such that for a traditional microscopy system the image focus would be lost.

2.6.4 Numerical reconstruction

In DHM the image can be refocused computationally by applying numerical reconstruction, which is based on simulating the inverse of the physical process of optical propagation. The reconstruction algorithm takes into account the parameters of the optical recording system. The object has a complex transmission function given by $t(x, y)$ (which essentially describes the optical path length variation of light passing through the object, based on a combination of variation in thickness and/or refractive index) and the condenser lens produces an illumination wavefield of the form $\exp(j\alpha[x^2 + y^2])$ in the object plane, where α is dependent on the wavelength, as well as the properties of the condenser. The combination of the microscope objective and the tube lens produces a magnified image of the form

$$o(x, y) = t\left(\frac{x}{M}, \frac{y}{M}\right) \exp\left(j\alpha\left[\left(\frac{x}{M}\right)^2 + \left(\frac{y}{M}\right)^2\right]\right), \quad (2.25)$$

in a plane a short distance, d , before the camera plane. Here, we have omitted the resolution limiting effect of the magnification system, which is determined by the numerical aperture of the MO. This effect is well described by a convolution of the term on the right hand side of Eq. 2.25, with the point spread function of the imaging system, see Chapter 6 of Goodman[1]. Optical propagation in the paraxial regime, is defined by the Fresnel transform in Section 2.3.3 which allows the complex field in the image plane and the camera plane to be described by a simple convolution operation:

$$o(x, y) = O(x, y) * \exp(-j\pi[x^2 + y^2]/\lambda d), \quad (2.26)$$

where the asterisk in the above equation denotes convolution; a constant phase factor has been omitted from Eq. 2.26 for ease of notation. This convolution can be described as a multiplication in the spatial frequency domain.

$$F\{o(x, y)\}(k_x, k_y) = F\{O(x, y)\} \times \exp(-j\pi\lambda d[k_x^2 + k_y^2]), \quad (2.27)$$

where F is operator notation for the Fourier transform as defined in Section 2.2, from the spatial domain to the corresponding spatial frequency domain, and (k_x, k_y) denote the spatial frequency coordinates. $o(x, y)$ denotes the reconstructed complex object wavefield. Both Eq. 2.26 and 2.27 above can be discretised in order to take into account the discrete nature of the digital hologram $O(n_x\delta x, n_y\delta y)$. Appropriate selection of the sampling rate in the image plane results in an equation that is effectively described by a single DFT operation, can be found in Section 2.3.3

as well; for this algorithm, known as the direct method, the required sampling rate can be problematic for short distances, d . An alternative algorithm can be developed using Eq. 2.27, which enables calculation of the complex field in the image plane $o(n_x\delta x, n_y\delta y)$, for the range of values defined in Eq. 2.24, by using two DFT operations:

$$\begin{aligned} DFT\{o(n_x\delta x, n_y\delta y)\}(m_x\delta k_x, m_y\delta k_y) &= DFT\{O(n_x\delta x, n_y\delta y)\}(m_x\delta k_x, m_y\delta k_y) \\ &\times \exp(j\pi\lambda d[(m_x\delta k_x)^2 + (m_y\delta k_y)^2]) \end{aligned} \quad (2.28)$$

where the m indices take the same integer values as the corresponding n values defined in Eq. 2.24 and $\delta k_x = \frac{1}{(N_x\delta x)}$, $\delta k_y = \frac{1}{(M_y\delta y)}$. The algorithm is therefore based on a first DFT applied to the digital hologram, the result of which is multiplied by a discrete chirp, followed by an inverse DFT to recover $o(n_x\delta x, n_y\delta y)$. Although this algorithm, sometimes called the spectral method, requires the use of two FFT operations, it has the benefit of having a constant output width in both x and y , equal to the camera size, regardless of the distance parameter. For this reason, this is often the algorithm of choice in DHM, and it is the basis for the investigations of all following chapters in this thesis. As discussed in Section 2.3.3, we note that the Fresnel transform is based on the paraxial approximation, which assumes that the propagation distance is appreciably larger than the values of x and y that are under consideration. An alternative method for simulating the propagation of a coherent wavefield between two planes is the angular spectrum method as described in Section 2.3.4. This method makes no assumption about small angles and is similar to the algorithm described by Eq. 2.28 above, with the exception that the chirp has a different form. This method is consistent with the first Rayleigh Sommerfeld solution. For a more detailed description, and comparison, of the various algorithms that can be employed for the reconstruction of digital holograms can be found in Ref.[64] and Ref.[42]. The interested reader can also find a discussion on the correct sampling conditions for digital holograms and their reconstructions in Ref.[65, 66].

2.6.5 Phase unwrapping

The amplitude and phase information can be extracted from the reconstructed complex object wavefield $o(x, y)$, recovered by the numerical reconstruction algorithm discussed in Section 2.6.4. The phase profile $\varphi(x, y)$ can be calculated by the follow equation:

$$\varphi(x, y) = \tan^{-1} \frac{IMAG[o(x, y)]}{REAL[o(x, y)]} \quad (2.29)$$

where $REAL[\]$ represents the function that extracts the real part and $IMAG[\]$ represents the function that extracts the imaginary part from a complex value. Because of the periodicity of trigonometric functions, the phase extracted by the arc-tangent

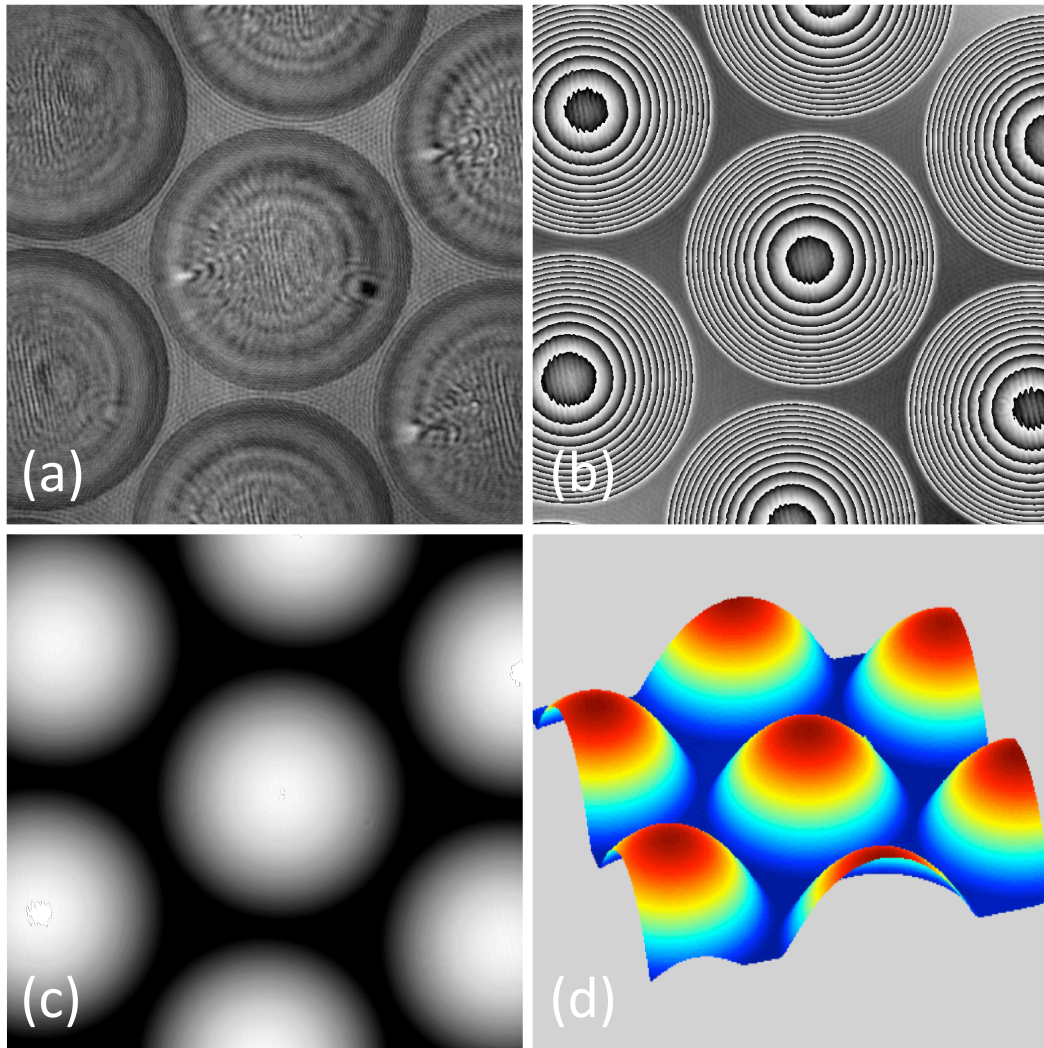


Fig. 2.7 (a), (b), (c) and (d) show the amplitude, wrapped phase, unwrapped phase, and depth map of a quantitative phase image of a microlens array respectively, recorded using the DHM system described in Section 2.6.

function in Eq. 2.29, is wrapped in the range of $[-\pi, \pi]$ [67] and presented as a serrated distribution. The phase profile is wrapped in most of the phase imaging techniques. The physical description is that when the optical variation from the thickness of the sample is larger than the wavelength, it results in the phase discontinuities at every 2π in the phase image. It is notable that the wrapped phase is unable to quantitatively represent the sample thickness; phase unwrapping is a necessary process in order to achieve the accurate height profile, thickness profile, and/or refractive index profile, in addition to the reconstruction of the image intensity. The amplitude, wrapped phase, unwrapped phase, and depth map of a QPI of a microlens array (recorded using a $20\times/0.4MO$) are shown in Fig. 2.7. The same QPI is used for assisting in describing and interpreting the proposed label-free color staining algorithm in Fig. 7.2 in Chapter 7. In this thesis all of the results showing an unwrapped phase were achieved using an algorithm presented in Ref.[68].

Phase unwrapping[67, 69, 70] have resulted in numerous applications including: Interferometric Synthetic Aperture Radar(INSAR)[71], Synthetic Aperture Sonar[72], Magnetic Resonance Imaging(MRI)[73] and optical interference measurement[74]. A number of phase unwrapping algorithms based on different strategies has been proposed[68, 62]. They mainly can be classified into three types. (i) Path-following algorithms. The typical example is the Branch-Cut method in terms of path integrals, proposed by Goldstein in 1988. Wei and Cumming[71] proposed the Region-Growing algorithm that divides the hologram into a number of regions and the path follows the quality of regions from high to low, instead of using the residues and branch-cuts. Other methods, such as the Mask-Cut and Minimum-Discontinuity methods, are also based on a path following algorithm. (ii) Global algorithms. The global algorithms are based on mathematical optimization, including the weighted and unweighted least squares algorithm[75] and minimum L_p norm method[70]. (iii) Minimum cost flow method[76]. This type of method is based on using an auxiliary network, which is computationally efficient and robust to the noise. In this thesis, a residue compensation algorithm proposed by Miguel[68] is applied to unwrap the phase image.

2.6.6 Focus detection

Digital holographic microscopy is unlike classical imaging systems in that one can obtain the focused image without situating the camera in the focal plane; indeed, it is possible to recover the complex wave-field at any distance from the camera plane. In order to reconstruct the image as described in Section 2.6.4, the captured interference pattern is first processed to remove the virtual image and DC component, and then back-propagated using a numerical implementation of the Fresnel transform. A necessary input parameter to this algorithm is the distance from the camera to the image plane, which may be measured independently, estimated by eye following reconstruction at multiple distances, or estimated automatically using a focus metric.

Traditional microscopy uses mechanical adjustment of the microscope objective or sample stage to refocus, while in DHM this is achieved by varying the distance parameter that is input to the reconstruction algorithm. Various metrics exist that can be applied to images in order to compare the degree of focus. In the case of traditional brightfield microscopy these focus metrics can be applied to a sequence of captures that are recorded using a scanning translation stage in order to implement “autofocusing”. In the case of DHM the same approach may be applied, except that in this case, only a single capture is required, and the sequence of image intensities can be generated by repeated numerical reconstruction of this digital hologram[77–81, 10, 82, 83, 11, 84–95]. This functionality enables DHM to record highly varying dynamic scenes at high speeds, since the requirement of mechanical refocusing is eliminated, and autofocusing can be applied post capture.

Autofocusing metrics have been a subject of research in microscopy for numerous decades with arguably the most popular being the variance of the image intensity[96]. In recent years there has been increasing interest in autofocus metrics for DHM with the initial work by Ma *et al.* employing the maximum of the variance in order to focus macroscopic scattering objects using digital holography[77] for 3D shape measurement. Since then, there have been numerous investigations of autofocus metrics in the context of macroscopic digital holography[77–79] as well as DHM[80, 81, 10, 82, 83, 11, 84–89, 97, 90], including the application of the ℓ^1 norm[80] as well as edge detection methods[81, 10, 82, 78, 97], such as the gradient and Laplacian. Other methods make use of the wavelet-transform[79], the total power [83], frequency spectrum-based metrics [11, 84], a correlation coefficient[85], the Tamura coefficient[86, 97], the contrast at the boundary of the reconstruction[87], and a form of modified enclosed energy[88, 89]. There has also been efforts to increase the speed of DHM based autofocusing using graphics processing units[91] and reducing the sampling rate of the hologram[92]. An investigation of the application of sparsity metrics for autofocusing in DHM is provided in Chapter 5.

2.6.7 Aberration compensation

The reconstructed amplitude and phase images recovered from DHM contain aberrations and distortions, including spherical aberration[98], astigmatism[99] and anamorphism[100]. They are mainly introduced by the optical components in imaging systems, such as the microscope objective and the tube lens[101, 102]. Recently, several aberration compensation methods for DHM have been proposed, some of which are used in the work presented in this thesis. These numerical methods are mainly based on multiplying a phase mask by the reconstructed complex wavefield in the image plane or the recorded hologram[101, 103, 98]. Cucho *et al.*[101] demonstrated how an appropriate numerical phase mask could be manually calculated and iteratively adjusted in the reconstruction algorithm in order to correct the wavefront deformation caused by aberrations in the microscope objective and in the reference wavefront. De Nicola *et al.*[100] presented a method to correct the anamorphism by the subtraction of reconstructions in two different distances. Ferraro *et al.*[103] proposed a numerical method to compensate aberrations, achieved by subtracting a reference hologram of a flat area in the object from the original hologram in the Fourier domain. We used this method in Chapter 4 to correct the aberration caused in the optical imaging system. Colomb *et al.*[20, 104, 105] computed a polynomial phase mask directly from the hologram of the phase reconstruction parameters of the phase mask in terms of the Zernike polynomial coefficients, which is placed in the camera plane to remove the phase aberrations. Physical methods of aberration compensation are also possible based on the adjustment of the design of the optical system. Myung K. Kim and Christopher J. Mann[106] placed an identical

microscope objective in the reference path which makes the spherical curvature in both paths equal. This leads to removing the 2nd phase aberrations directly in the recording process. Weijuan Qu *et al.*[107] used an adjustable lens to compensate the quasi-physical phase aberrations in the recording process for both reflection and transmission DHM.

2.7 Digital in-line holographic microscopy

2.7.1 Methods for digital in-line holographic microscopy

As discussed in Section 2.6, holography[13, 108] may be described as an imaging methodology that involves separate processes for recording and replay in order to recover the image. The first process involves recording an interference pattern from the wavefield that is generated by an object beam as well as a known reference wavefield. The second process involves the reconstruction of the object transmission function (the image) by some way using the recorded interference pattern. As discussed in Chapter 1, for several decades, photographic films were required to record the holograms and the reconstruction process was implemented optically; however, in the past two decades this approach has been superseded by the application of a digital area sensor to record the holograms, and the reconstruction process is performed using a set of computer algorithms that simulate optical replay[109, 110].

Several architectures exist for optically recording a digital hologram. The off-axis technique, initially developed for the case of photographic film[108], enables separation of the noisy DC and twin terms that are inherent in holography. This approach, which is described in detail in Section 2.6 above, was first used with digital sensors by CuChe *et al.*[18] whereby spatial filtering was achieved in the discrete Fourier transform domain and is described in detail in Section 2.3.3. However, this architecture as much as quarters the recording resolution of the CCD[111]. Contrarily, an in-line architecture, which was the basis for Gabor's initial discovery as discussed in Chapter 1, allows for full resolution to be maintained [112]. The new microscopic principle originally proposed by Gabor [13] is the basis for the simplest realization of digital holographic microscopy and has been coined digital in-line holographic microscopy (DIHM) [113, 113–116]. An assumption made when using this set-up is that the object wave is weak with respect to the reference wave, which is an accurate approximation in the case of highly transparent objects. However, this limits the applicability of the Gabor hologram as described in Chapter 9 of [1] to a narrower range of samples. In DIHM, a pinhole generates a diverging spherical wave which is incident on a sample some small distance away. The resultant diffraction pattern is captured by a digital sensor and an image of the sample can be reconstructed numerically using a variety of different algorithms [113, 117, 118] that are based on both paraxial and non-paraxial approximations.

DIHM has a number of interesting advantages over off-axis DHM. Firstly, the implementation of the technique is extremely simple and requires only a pinhole of partially coherent light (which can be easily achieved using the output from a single mode fiber) and a digital sensor. This facilitates an inexpensive and easy-to-build system for which magnification is achieved without the use of an expensive microscope objective with numerical apertures in excess of 0.8. The second advantage of the system is that the magnification and field of view of the system are both continuously variable by simply moving the position of the sample in the space between point source and the camera; the ratio of the point-source to object distance relative to the point-source to camera distance equates to the magnification of the system. This advantage is particularly interesting when one considers that for more than a century microscopes have been limited to a discrete number of fixed magnifications by rotating a nosepiece over a set number of microscope objectives. Such a set-up also has the disadvantage of the cost associated with each one of these objectives. Despite these interesting advantages, DIHM has the very significant disadvantage of the overlapping of the two dc terms and the twin image term during reconstruction[112] as discussed in Section 2.6 in this chapter. Under certain conditions, for example if only the intensity image of the sample is required, the deleterious effect of the twin image can be neglected[113]. However, for the more general case of reconstructing the phase of sample, the presence of the twin and DC terms render the phase information unusable.

2.7.2 Recording and reconstruction of an in-line digital hologram

In a Gabor holography/DIHM recording system, an object is illuminated by a diverging spherical wave usually originating from a small pinhole, which scatters some of the light creating the object wave. The undiffracted light, assuming the object is weakly transmissive, provides the reference wave. A typical physical set up for Gabor holography is shown in Fig. 2.8. For simplicity, we consider the one-dimensional case only in the mathematical analysis in this chapter. A spherical beam emerges from a pinhole with a wavelength λ . Following propagation of a distance d this diverging spherical field is incident upon a transmissive object, which introduces a phase delay that we denote as $o(x)$. An intensity pattern is recorded from the resultant wavefield a further distance z away from the object plane.

The diverging wavefield from the point source can be described using phasor notation in both the object plane ($r_d(x)$) and the camera plane ($r_f(x)$) as follows:

$$\begin{aligned} r_d(x) &= \exp\left[\frac{j\pi}{\lambda d}(x^2)\right] \\ r_f(x) &= \exp\left[\frac{j\pi}{\lambda f}(x^2)\right] \end{aligned} \tag{2.30}$$

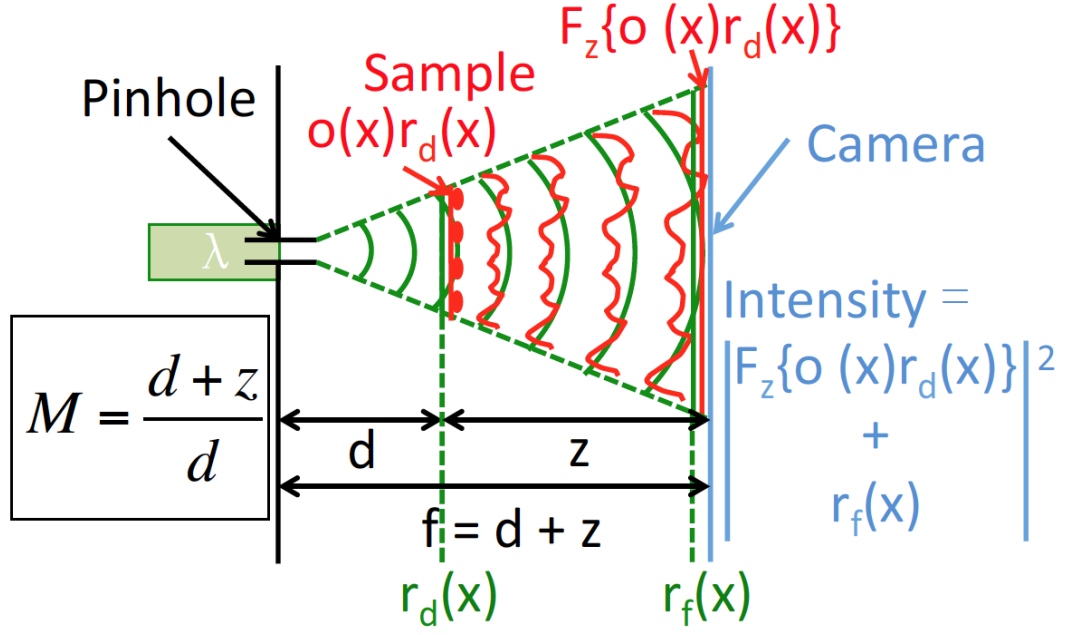


Fig. 2.8 The physical set-up is a Gabor set-up with a spherical diverging beam, $r(x)$, emerging from a pinhole, illuminating an object, $f(x)$, a distance d_1 away. Immediately behind this plane there is an object wave $o(x)r(x)$. The interference pattern, $H(x')$, between the propagated reference wave, $R(x')$, and the propagated object wave, $O(x')$, is captured on a CCD a further d_2 away. This captured pattern is the input to the numerical reconstruction part of the imaging system which is described in Section 2.7.2.

where $f = z + d$. If the object is assumed to be weakly scattering, the object plane can be described as having a transmission function, $t(x)$, as

$$t(x) = 1 + o(x). \quad (2.31)$$

The field in the plane immediately after the object plane can, therefore, be described as $r_d(x) + r_d(x)o(x)$ and, following a Fresnel propagation, the field in the camera plane can be described as $O(x) + r_f(x)$, where $O(x)$ represents the propagated object field as follows:

$$\begin{aligned} O(x) &= F_z[o(x)r_d(x)] \\ &= F_z\left\{o(x)\exp\left[\frac{j\pi}{\lambda d}(x^2)\right]\right\} \end{aligned} \quad (2.32)$$

and where F_z denotes the operator for the Fresnel transform, which is defined in Section 2.3.3, but which is reproduced in the equation below for ease of reading

$$F_z[g(x)] = 1/\sqrt{i\lambda z} \int_{-\infty}^{+\infty} g(x) \exp\{[i\pi(x-x')^2]/(\lambda z)\} dx. \quad (2.33)$$

, which is identical in form to the description of the Fresnel transform given in Eq. 2.14 earlier in the thesis, except that in this case we use only one dimension in the representation for simplicity of analysis. Using one of the properties of the Fresnel transform[64], it is possible to rewrite Equation 2.32 as follows:

$$O(x) = \exp\left[\frac{j\pi}{\lambda dM}(x^2)\right] F_{Mz}[o(x/M)]. \quad (2.34)$$

where $M = (d+z)/d = f/d$. This indicates that the effect of illuminating the sample $o(x)$ with a diverging spherical wavefield (with parameter d) followed by propagation of distance z is equivalent to first magnifying the sample $o(x)$ by a factor M , followed by propagation a distance Mz , and finally followed by multiplying the result by a chirp function with parameter dM . This result can be confirmed using the matrix decomposition as follows:

$$\begin{bmatrix} 1 & z \\ 0 & 1 \end{bmatrix} \begin{bmatrix} 1 & 0 \\ 1/d & 1 \end{bmatrix} = \begin{bmatrix} 1 & 0 \\ 1/dM & 1 \end{bmatrix} \begin{bmatrix} 1 & Mz \\ 0 & 1 \end{bmatrix} \begin{bmatrix} M & 0 \\ 0 & 1/M \end{bmatrix}. \quad (2.35)$$

The matrices on the left of the equals sign in the above equation directly relate to Equation 2.32, while the matrices on the right side relate directly to Equation 2.34. It is clear that the relationship will hold if $M = (d+z)/d$. If the complex valued $O(x)$ could be retrieved from the recorded intensity pattern on the camera, the magnified image $o(x/M)$ could be recovered by first multiplying by a discrete chirp function with parameter $-dM$ followed by computation of the Fresnel transform a distance $-zM$. Several algorithms have been developed for reconstruction that make use of matrix decomposition that are similar to that shown in Equation 2.35[118].

However, it is not possible to recover $O(x)$ in isolation from the recorded intensity pattern, but it is possible to get an approximation. The recorded intensity is given by

$$I_{inline}(x) = |O(x) + r_f(x)|^2 \quad (2.36)$$

Expanding Eq. 2.36 gives an expression with four terms [17]

$$I_{inline}(x) = |O(x)|^2 + |r_f(x)|^2 + O(x)r_f^*(x) + r_f(x)O^*(x). \quad (2.37)$$

If $r_f(x)$ is an ideal spherical wave then $|r_f(x)|^2$ will simply be a constant and can easily be removed. To achieve this, $|r_f(x)|^2$ can be recorded separately and removed by subtraction. Following the analysis described in Section 9.3 of Ref.[1] one may assume that the $|O(x)| \ll R(x)$ and so drop this term, which leaves the two twin image terms. It has been demonstrated that the twin image term is so spread out by the diverging wave that it can be considered insignificant [113]. In this way $O(x)r_f^*(x)$ can be approximately recovered, from which $o(x/M)$ can be approximately reconstructed. In this way it is possible to reconstruct an approximate image

intensity $|o(x/M)|^2$ of the magnified object. The limitations of DIHM systems in terms of magnification, numerical aperture, and field of view have been investigated extensively by other authors[113–116].

Despite the attempts to remove or ignore the three unwanted terms in Eq. 2.36, their residual effect is to render the phase image completely unusable. Numerical techniques have been developed that have improved the quality of the phase image based on iteratively numerically propagating between the camera and object plane and applying a set of constraints in both of these planes[119]. While this technique does improve the phase image it does not in general work well for all samples. Another approach is to record the hologram for several different sample positions, i.e. for several values of d in Fig. 2.8, and to either use an iterative constraint based approach or the transport of intensity equation or both in order to recover meaningful phase images[120, 121]. The purpose of Chapter 4 is to develop an off-axis DHM approach that can retain the key advantage of DIHM in terms of variable magnification, numerical aperture, and field of view, while permitting a single capture that requires no additional phase recovery.

2.8 Lensless microscopy

A variant of DIHM is known as lensless microscopy[122–124]. This is essentially the same as the DIHM approach; however, in this approach the microscope slide is placed directly atop a camera sensor and a pinhole light source such as from an LED or filtered white light is used to generate a diffraction pattern on the sensor. Lensless microscopy can be used to recover the complex transmittance from a wide field area that is equal to that of the sensor using either a multi height approach[122, 123] or more recently using deep learning in neural networks[125]. Lensless microscopy offers an exciting alternative to traditional microscopy that has the advantages of offering a significantly reduced form factor and cost while providing images of complex transmittance over a significantly larger area on the microscope slide than can be achieved using traditional methods and has been shown to be useful with histopathology[123]. However, despite the significant advantages of the approach it is not applicable to dynamically changing scenes - multiple captures are needed and a heavy amount of processing is also required. Multiple captures are required with subpixel shifting[126] in order to render the required sampling rate since sensors with even the smallest pixel sizes (1.5μ) are larger than the minimum resolvable detail, and multiple captures are also required in the direction of propagation if accurate quantitative phase is to be recovered[120, 121].

2.9 White light techniques

In recent years, quantitative phase imaging has been shown to be possible with white light[58, 59, 127–132], which has significantly less noise due to the lower spatio-temporal coherence. The Spatial Light Interference microscopy(SLIM) technique[58, 127] involves capturing a sequence of traditional phase contrast images, in which the phase shift of the unscattered wave is varied using a spatial light modulator; this method has been extended to a single capture implementation[128] that can be applied to dynamically varying specimen. Transport of intensity equation(TIE) methods[129–132] have also been shown to enable recording the quantitative phase using white light. This approach requires the recording of a sequence of defocused images,[129–131] which can be obtained either by refocusing of the microscope objective or passively by using an electronically tunable lens in the imaging path[131]. A single shot approach has also been proposed for dynamically varying specimen[132].

Both the SLIM and TIE approaches can be applied with existing commercial microscopes that are available from vendors such as Zeiss, Olympus, and Nikon; TIE in particular has the advantage of requiring no additional optical elements other than a phase contrast annulus in the condenser arm. White light QPI methods such as these are likely to replace existing phase contrast and DIC functionality in life science microscopes for the reason that the complex transmittance of the sample, available via QPI, permits other optical recording modalities (that do not involve staining or fluorescence) to be effectively simulated by numerically emulating the recording system. For example, high resolution phase contrast and DIC images have been demonstrated to be easily generated using a complex cell image obtained via QPI[130]. We extend this approach to include Rheinberg illumination in Chapter 6.

In Chapter 2, we have introduced and reviewed the background theory behind quantitative phase imaging, with an emphasis on digital holographic microscopy. In the following chapter, we propose a novel compact off-axis DHM module for full-field quantitative phase imaging with low spatial coherence illumination.

Chapter 3

Inexpensive portable module for digital holographic microscopy

3.1 Introduction

In Chapter 2, the principles of off-axis digital holographic microscopy were outlined. In this chapter a method known as ‘common-path interferometry’ is employed in order to record an off-axis hologram. Common path interferometry refers to a technique whereby both the object beam and the reference beam co-propagate for a large part of their optical paths, before being split up towards the end of the system. The result of this approach is that there is a higher temporal stability between both beams and there is also a greater similarity between both beams resulting in less noise. Numerous research groups have proposed setups for common-path or self-interference for the purpose of acquiring quantitative phase images over the past decade. These include the systems of Popescu *et al.* [133, 134], Jang *et al.* [135], Kemper *et al.* [22], Coppola *et al.* [136], Mico *et al.* [137], and Bon *et al.* [138] as well as the work of Shaked *et al.* [139–142]. Some of these systems are based on using a diffraction grating, while others are based on using a Michelson interferometer and work on the precondition that half the object plane is free from any scatterers and can therefore be used as the reference.

The work that is most similar to the contribution proposed in this chapter, is the work of Natan Shaked *et al.* [140–142] also makes use of a Michelson type interferometer, but places no preconditions on the sample plane. Shaked’s group first introduced a common path interferometer, which they called the ‘tau-interferometer’ in 2012 [140]. This method made use of a 4- f imaging system at the output port of a microscope with a refractive beam splitter cube placed after the first lens and two mirrors. A pinhole is inserted in one path close to the mirror in order to filter out the information from the object and leave only a plane wave. The same beamsplitter recombines both beams and the second lens projects the image and the reference beam onto the camera. This common path interferometer had several

advantages over the traditional off-axis architecture described in Section 2.6. Firstly, the fact it has a small form factor and could be added to an existing microscope is attractive. Secondly the device is inexpensive. Thirdly, the device is robust to vibration, which can often degrade the interference pattern. Fourthly, the need to realign the reference due to changing the sample (due to different path delays from different thickness/glass slides etc.) is lessened. Finally, because of the common path architecture, a low coherent source could be used, so long as careful path length matching is achieved for the part of the system over which the reference and object beams do not share a common path.

Although the ‘tau-interferometer’ could partially achieve the off-axis condition by rotation of the beam splitter, it was primarily suited to in-line holography and due to the low coherence of the source used in the experiments (a supercontinuum source with a filter produced a source with a full width half maximum spectral width of approximately 7 nm), off-axis interference could only be achieved at the edges of the image. For this reason the same research group proposed the ‘off-axis tau-interferometer’[141], which could overcome the limitations of the initial design but still retain the features of portability, low cost, and easy alignment, even using a low-coherence source from a super-continuum laser. In this case, rather than use a flat mirror (with a pinhole) to reflect the object beam back towards the beamsplitter, a retroreflector was used instead. A retro-reflector is designed using a pair of mirrors that are attached to each other at a right angle. The effect was to spatially shift the location of the Fourier transform of the object beam. The net effect of this is to generate an off-axis reference wavefield. This can be understood in terms of the properties of the Fourier transform; a shift in the Fourier (spatial frequency) domain (i.e. a shift in the position of the focussed spot) results in a linear phase shift in the space domain (i.e. a tilt of the object beam in the camera plane at an angle that is proportional to the shift in position of the focussed spot).

The ‘off-axis tau-interferometer’ was still limited when using low-temporal-coherence illumination because a refractive beam splitter is used to split the beams. It also could not work with a low-spatial-coherence source, due to the fact that the retro-reflector is positioned only in the object beam path, which introduces flipping of the object beam relative to the reference plane wave. Another disadvantage is that the reference beam passes through the pinhole twice resulting in a loss of power. These disadvantages led to the development of the ‘partial-coherence tau-interferometer’ by the same research group[142]. This system utilised a temporally coherent DPSS source and introduced spatial incoherence by using a rotating diffuser in the illumination path. The size of speckle was controlled by using an aperture in a $4-f$ system in the illumination path and the spatial coherence was controlled by rotating the diffuser. This system used two retroreflectors, one for each path and in this way both the object and reference beams were flipped to have the same orientation. The amount of shift applied by the retroreflectors in both paths is half

that used in the ‘off-axis tau-interferometer’. The pinhole size was increased to allow the spatially coherent illumination to pass through and cancel with its conjugate in the interference term. By keeping the speckle size large and the pinhole relatively small it was possible to achieve quantitative phase imaging.

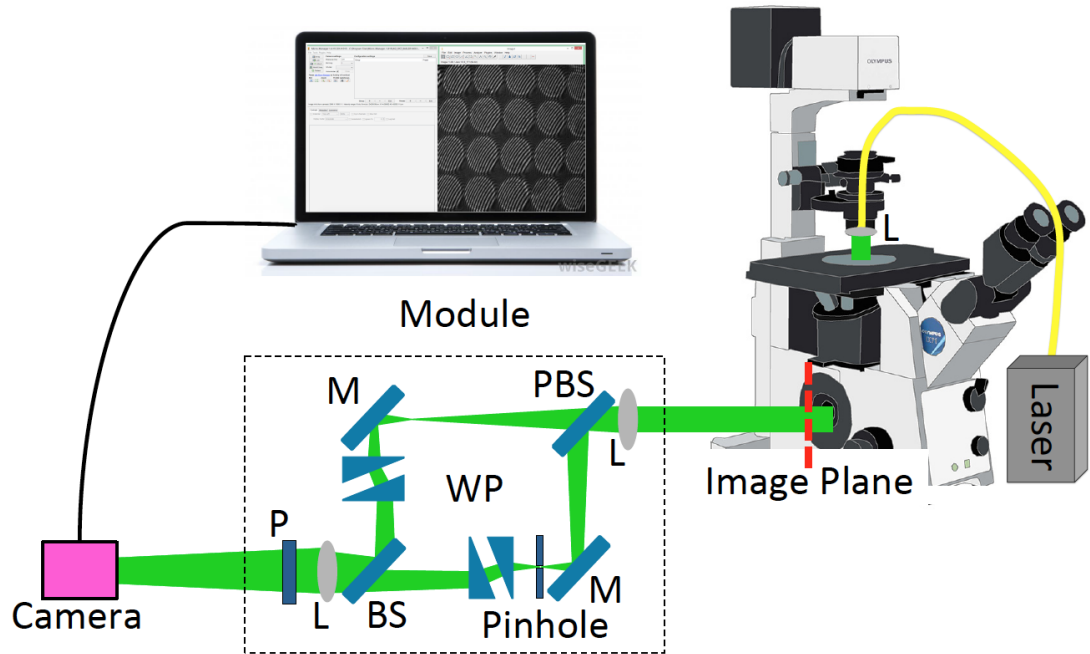


Fig. 3.1 Optical setup of off-axis digital holographic microscopy using the common-path module proposed in this chapter. L: Lens; P: Polarizer; BS: Beam Splitter; M: Mirror; WP: Wedge Prism. The module is placed at the output port of an existing microscope and an inexpensive laser is used to illuminate the sample.

In this chapter, a new common-path interferometer is introduced, which is illustrated in Fig. 3.1. This system has several similarities to the ‘partial-coherence tau-interferometer’ but which provides a number of significant advantages. Like the ‘partial coherence tau-interferometer’ the system is portable and can be easily added to the output port of an existing microscope, it is inexpensive and has a small form factor, it is robust to vibration and to differential noise as well as not requiring realignment of the reference when different samples are imaged. Unlike the ‘partial coherence tau-interferometer’, which uses a Michelson architecture, our proposed system uses a Mach-Zehnder architecture. Instead of using two retroreflectors, our system makes use of two prism-pairs which also have the effect of shifting the Fourier transforms of the object and reference paths. The proposed system allows for simple control of the tilt that is applied in both the reference and object paths such that it can be continuously varied and match to the bandwidth of the camera that is used to record the hologram. We believe it is easier to align the pinhole in our proposed system because the reference path is based on transmission instead of

reflection. The proposed system is described in Section 3.2 and the experimental results are provided in Section 3.2.1.

3.2 Off-axis DHM module

In this section we describe the proposed module in more detail. The first point of note is that an inexpensive laser source is collimated using a plano-convex lens or by using the existing condenser in a brightfield microscope. This light source does not need to be split into two output fibers as for the case described in Section 2.6. In this case the module will split the object wavefield outside the microscope and filter one of the paths in order to obtain the a plane reference wave. The second point of note is that the module is placed at the output camera port of the microscope where a camera would usually be used to record an image. The complex image of the sample appears at the image plane and this is the input to the module as illustrated in Fig. 3.1. A more detailed graphical illustration of the module is provided in Fig. 3.2.

The first element inside the module is a bi-convex lens and the base of the module is positioned such that this lens is located at a focal length distance from the image plane of the microscope. This lens is the first of two in a $4-f$ imaging system that maps the image plane of the microscope to the camera plane. A beam splitter is placed immediately after the lens, which splits the wavefield into two parts, illustrated in red (object wavefield) and green (reference wavefield) in the figure. At the back focal plane in the reference path a pinhole is positioned to spatially filter a plane wave. Immediately after the pinhole a pair of wedge prism pairs are located; the first prism refracts the incoming field at an angle α and the effect of the second prism is to undo this tilt. If the prisms are separated by a distance d , the overall effect of the two prisms combined is to shift the wavefield spatially by a distance δ , which is defined below:

$$\delta = d \tan \alpha \quad (3.1)$$

Since this shifting of the reference field occurs in the back focal plane of the lens, it can be described as a shift in the spatial frequency domain, which in turn is described as a linear phase shift, or tilt, in the space domain at the back focal plane of the second lens[143] in the $4-f$ imaging system. For simplicity, we assume that the shifting occurs only in the x -direction, and the reference wavefield is described as a tilted plane in the camera plane as follows:

$$R(x,y) = \exp\left(\frac{j2\pi x\delta}{f\lambda}\right) \quad (3.2)$$

where λ and f denote the the laser wavelength and the focal length of the lens respectively. The object wavefield propagates through an identical pair of wedge prisms, which are in this case, oriented in the opposite direction to that of the

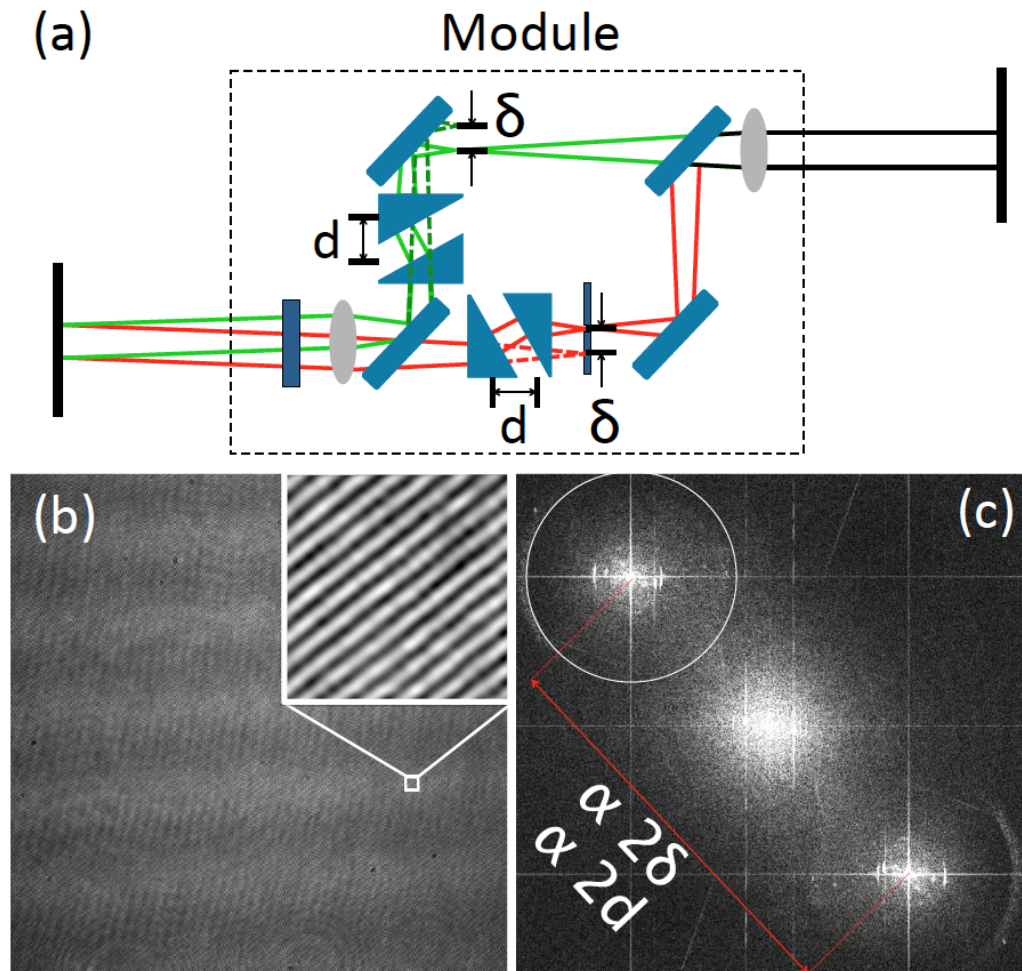


Fig. 3.2 (a) This figure illustrates the components and light paths within the module. Two wedge-prism pairs are used to shift the object and reference beams in opposing directions in the Fourier domain. A pinhole is used to obtain a plane reference wavefield which interferes with the object wavefield on the camera face. (b) Intensity pattern recorded by the camera and (c) the discrete Fourier transform of this intensity pattern showing the separation of the twin image terms. This separation is proportional to the distance between the wedge prism pairs and can be adjusted to match any particular camera pixel size.

reference path. The result is a shifting of $-\delta$ in the spatial frequency domain, which can also be described as a linear phase shift, or tilt, in the space domain at the back focal plane of the second lens. The object wavefield in the camera plane can, therefore, be described as follows:

$$O(x, y) = o(x) \exp\left(-\frac{j2\pi x \delta}{f\lambda}\right) \quad (3.3)$$

where $o(x)$ is the complex image produced at the image plane of the microscope, and which is input to the module. It should be noted that the linear phase term in Eq. 3.3 is equal in slope but opposite in sign to the linear phase term in Eq. 4.1. Here, we have assumed that the $4-f$ imaging system introduces no changes to the field $o(x)$. It should also be noted that generalisation to shifting along any particular direction in the $x-y$ plane. A second beam splitter is used to recombine the two wavefields before the second lens. A polariser is also used in advance of the camera in order to enhance the diffraction efficiency of the recorded hologram. We will also describe in the next section how this polariser can be used in conjunction with a polarising beam splitter in order to control the relative powers in both paths. The interference term that is recorded by the camera is given by:

$$\begin{aligned} I(x) &= |R(x) + O(x)|^2 \\ &= |O(x)|^2 + |R(x)|^2 + O(x)R^*(x) + R(x)O^*(x) \\ &= |o(x)|^2 + 1 + o(x) \exp\left(-\frac{j2\pi x 2\delta}{f\lambda}\right) + o^*(x) \exp\left(\frac{j2\pi x 2\delta}{f\lambda}\right) \end{aligned} \quad (3.4)$$

The camera pixel size will determine the spatial frequency support of the recorded intensity pattern $I(x)$. For a pixel size of p_x the spatial frequency support is given by $1/p_x$. In the discrete Fourier transform domain of $I(x)$, the linear phase terms in Eq. 3.4 will result in a separation of the twin image terms by an amount Δ as follows:

$$\begin{aligned} \Delta &= \frac{4\delta}{f\lambda} \\ &= \frac{4d \tan \alpha}{f\lambda} \end{aligned} \quad (3.5)$$

It is clear from Equation 3.5 that the separation between the twin image terms in the discrete Fourier domain is proportional to the distance d between the prism pairs, which is illustrated in Fig.3.2. The separation can, therefore, be easily controlled by varying the distance between the prisms, which is facilitated using cage optics as shown in Fig. 3.3 below. In this way, the system can be optimised for any camera pixel size. It should be noted that for the case of a laser source with low temporal coherence it may be necessary to carefully match the separation between the prism pairs in both paths in order to ensure a common path length. In the next section the experimental system is described in detail.

3.2.1 Experimental System

An image of the experimental system that implements the proposed module is shown in Fig. 3.3. The module is constructed on a small aluminum breadboard of dimensions $250\text{mm} \times 300\text{mm}$ (Thorlabs; MB2530/M). Both lenses are bi-convex lenses with 150mm focal length (Thorlabs; LB1437-A) and all four prisms are 10° round wedge glass prisms (Thorlabs; PS814-A) mounted on shims (Thorlabs; SM1W189) which were in turn mounted on rotation mounts (Thorlabs; CRM1/M). These rotation mounts containing the wedge prisms were mounted on cage optics in order to facilitate easy adjustment of the separation d , which is discussed in detail in the previous section. Both mirrors used in the system were identical (Thorlabs; BB1-E02). The pinhole (Thorlabs; P20S) has a diameter of $20\mu\text{m}$ and is mounted on a miniature xyz translations stage (Thorlabs; DT12XYZ/M) which allowed for alignment of the pinhole with the focused spot of the collimated plane wave laser illumination.

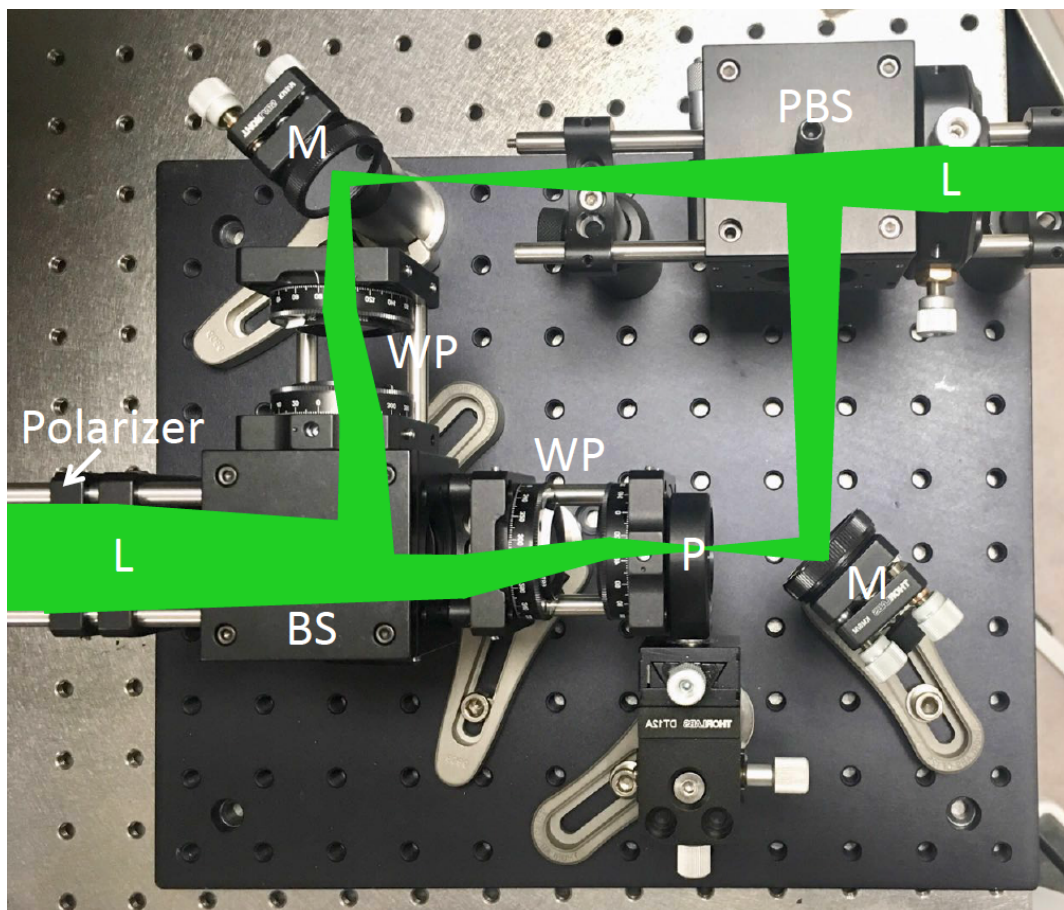


Fig. 3.3 Image of the experimental setup for the off-axis DHM module proposed in this chapter. L: Lens; P: Polarizer; BS: Beam Splitter; M: Mirror; WP: Wedge prism Pair.

The first beam splitter was selected to be a polarising beam splitter cube (Thorlabs; PBS201) mounted in a cage optics cube mount (Thorlabs; C4W). This polarising beam splitter, together with a linear polarizer (Thorlabs; LPVISE100-A) located close to the camera, the ratio of the powers in both paths could be controlled. This linear polariser also ensures a high diffraction efficiency of the recorded hologram. The second beam splitter is a broadband 50:50 cube beamsplitter (Thorlabs; BS013). The camera uses a CMOS sensor (Basler; acA200-340km) which has 2048×1088 pixels of size $5.5 \mu\text{m}$. Not shown in Fig.3.3 is the laser illumination or the microscope. The microscope is an Olympus Ix81 with which three microscope objectives were used to generate the results shown in Section 3.3: Olympus UMplanFl 10x/0.3, UMplanFl 20x/0.46, and UMplanFl 50x/0.8. A low power handheld laser alignment source was used (Thorlabs; HLS635) with power 3mW and centre wavelength 635nm and a full width half maximum of $<1\text{nm}$, which also has an FC/PC fiber connector which was used to couple the laser into a single mode optical fiber (Thorlabs; P1-460B-FC-2), which delivers the laser to the condenser lens of the microscope, which is used for collimation.

3.3 Results

The first set of results are shown in Fig. 3.4 for a microlens array object (Suss MLA 18-00028 quartz, circ. lenses, quad. grid, pitch $110 \mu\text{m}$, ROC $6.188\text{mm} \pm 5\text{percent}$, no AR-Coating, size $10\text{mm} \times 10\text{mm} \pm 0.05\text{mm}$, thickness 0.9mm , rectangular shape). The object was placed on the translation stage of the Ix81 microscope. The microscope objective (UMPlanFl $20 \times /0.46$) was adjusted using the focus knob of the microscope, and the eyepiece was used with a camera (Amscope) in order to determine the correct placement of the sample in the focal plane of the objective. A hologram was recorded by the camera and filtered in the discrete Fourier transform domain. The object wavefield was slightly out of focus and numerical propagation was applied in order to refocus to the correct distance, as described in Section 2.6. The resulting quantitative phase image is shown in Fig. 3.4.

Fig. 3.4 (a) shows the absolute value and (b) shows the phase of the reconstructed image. Some aberration of the phase image can be seen. Aberration compensation is performed as described in Section 2.6.7 whereby the hologram is recorded of no sample and reconstructed under the same conditions of the object wavefield. The resultant phase of this reference is shown in Fig. 3.4 (c). This is used to compensate for aberrations in the phase image of the object as shown in Fig. 3.4 (d). The corresponding unwrapped phase is shown in Fig. 3.4(d) for which unwrapping is performed using the algorithm described in Ref[68]. The unwrapped phase image is used to render a three-dimensional image of the thickness profile of the microlens array in Fig. 3.4(f).

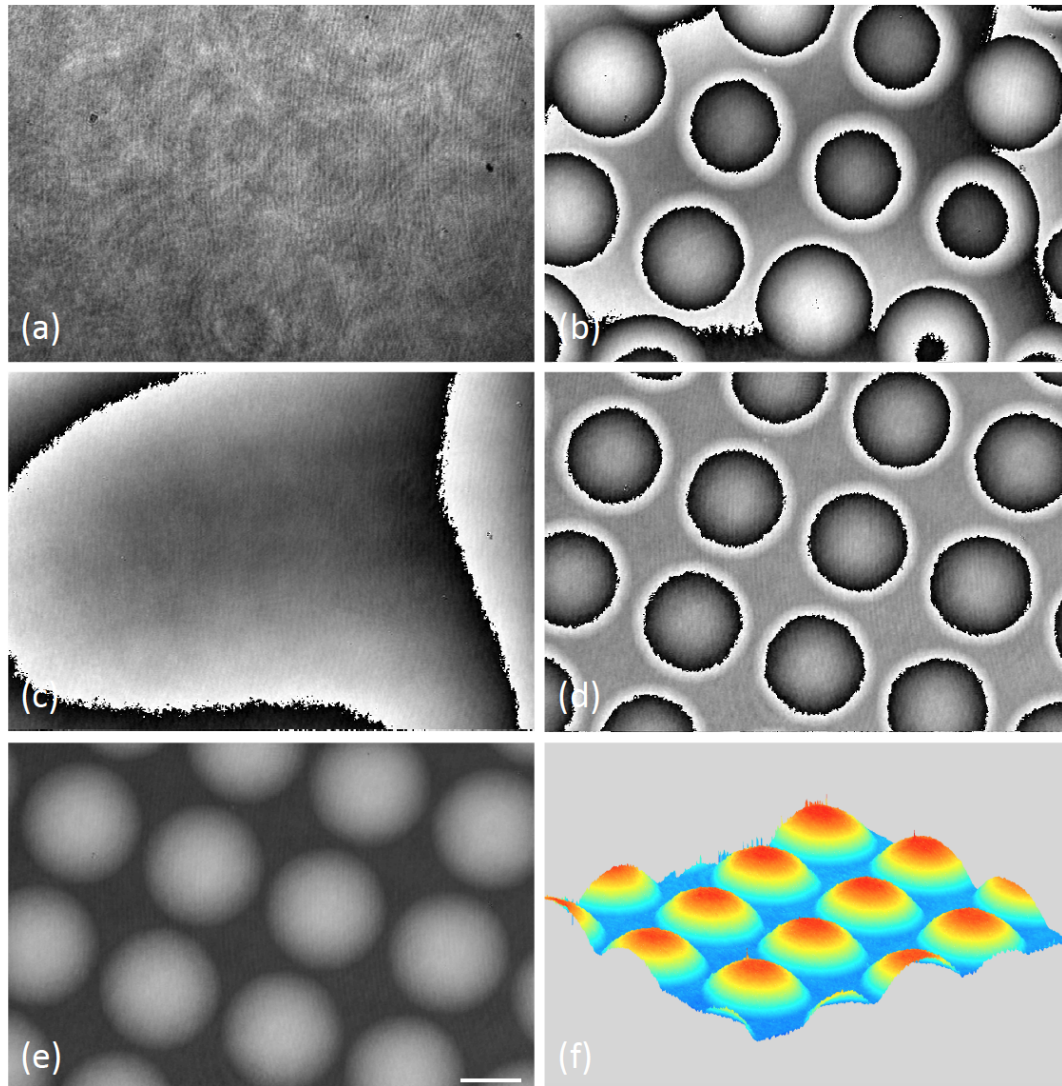


Fig. 3.4 Results for a microlens array using a 20x/0.46 microscope objective. The resolution bar represents $50\mu m$. (a) and (b) are the reconstructed amplitude and phase; (c) shows the phase image recorded from a reference hologram and (d) shows the phase image of the object following aberration compensation using this reference hologram; (e) is the unwrapped phase and (f) is a three-dimensional image of the thickness profile of the object.

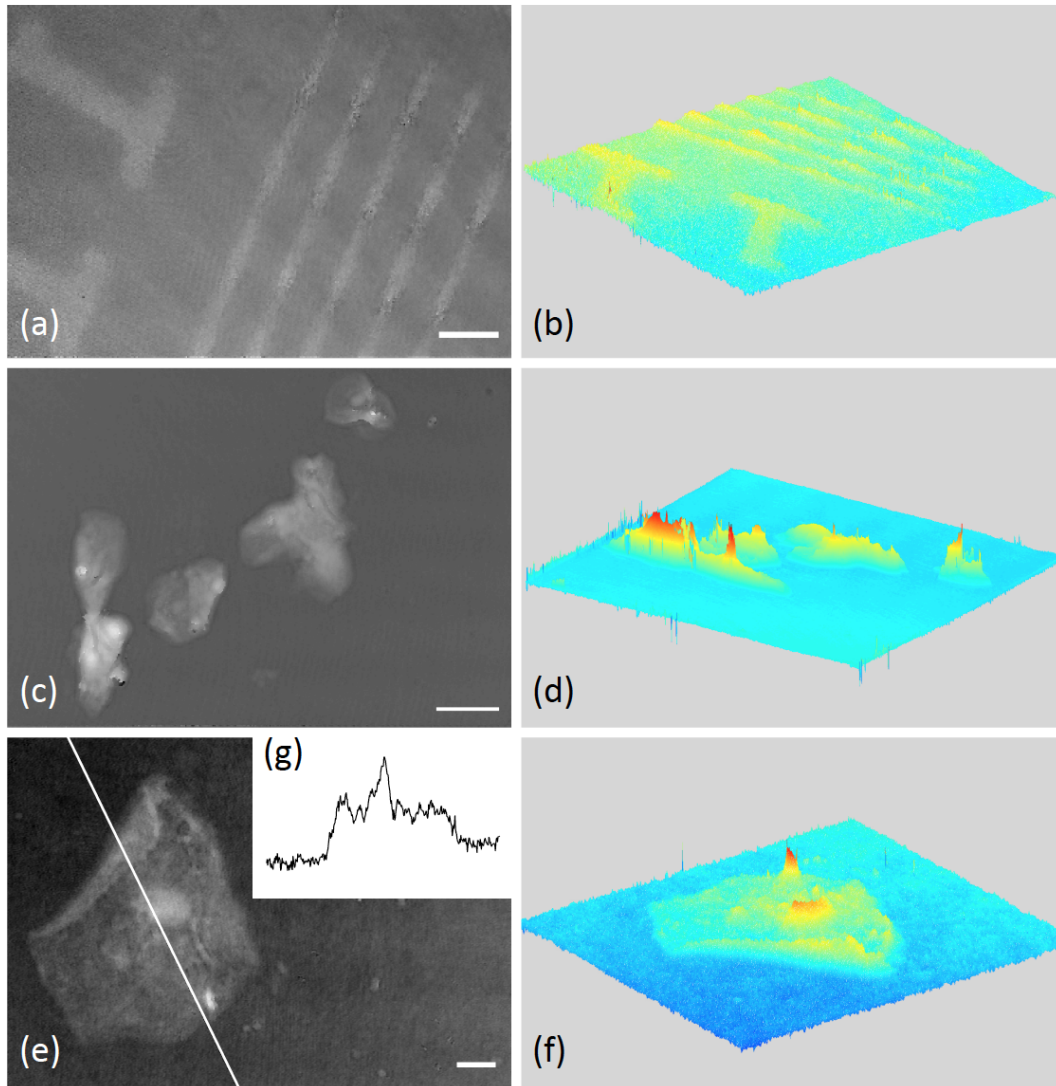


Fig. 3.5 (a) phase image and (b) thickness profile of a birefringent resolution chart recorded using a 10x/0.3 MO; (c) phase image and (d) thickness profile of human cheek cells recorded using a 20x/0.46 MO; (e) phase image and (f) thickness profile of a human cheek cell with 50x/0.8 MO; in all cases the resolution bar represents $10\mu m$.

Results for an additional set of objects are shown in Fig. 3.5. The first object was an NBS 1963A Birefringent Resolution Target (Thorlabs; R2L2S1B) for which a 10x/0.3 microscope objective was used to record the image. The final reconstructed phase image is shown in Fig. 3.5 (a) and the corresponding thickness profile is shown in Fig. 3.5 (b). The second object of interest is a glass slide on which are swabbed fresh human cheek cells from a healthy volunteer. This object was recorded using a 20x/0.46 microscope objective, the results of which are shown in Fig. 3.5 (b) and (c), and using a 50x/0.8 microscope objective, the results of which are shown in Fig. 3.5 (e) and (f). The thickness profile associated with a line that cuts through the cheek cell is also shown in Fig. 3.5(e). In all cases presented here aberration compensation, autofocusing, and phase unwrapping have been applied.

3.4 Conclusion

In this chapter, a new common-path interferometer has been described. Although this system has several similarities to the ‘partial-coherence tau-interferometer’ proposed by Shaked *et. al.*[142] it also has several differences. Like the ‘partial coherence tau-interferometer’ the system is portable and can be easily added to the output port of an existing microscope, it is inexpensive and has a small form factor, it is robust to vibration and to differential noise as well as not requiring realignment of the reference when different samples are imaged. Unlike the ‘partial coherence tau-interferometer’, which uses a Michelson architecture, our proposed system uses a Mach-Zender architecture. Instead of using two retroreflectors, our system makes use of two prism-pairs which also have the effect of shifting the Fourier transforms of the object and reference paths. The proposed system allows for simple control of the tilt that is applied in both the reference and object paths such that it can be continuously varied and match to the bandwidth of the camera that is used to record the hologram. We believe it is easier to align the pinhole in our proposed system because the reference path is based on transmission instead of reflection.

In Section 3.2 the module was described in detail and in Section 3.2.1 specific details are given on the optical elements that were used to construct the module. All of these elements, including a handheld laser source, were purchased from Thorlabs for less than €2000. During the course of the experiments the module was found to be surprisingly robust to vibration and was relatively noise free when compared with the off-axis architecture that was used for much of the early work in this thesis, which likely results from the common path architecture.

We note, however, that the module employs wedge prism pairs and will therefore not be useful for low-temporal coherence due to reliance of refraction angle on wavelength. Nevertheless, the system may work well for source with bandwidth of 7 nm such in the work of Shaked *et al.* One possible avenue for future work is to introduce low spatial coherence using a diffuser and to open the pinhole in a manner

similar to that described in [142], which may provide cleaner images with less noise due to parasitic interferences in the system.

In this chapter, we proposed a novel DHM interferometer with a compact structure for full-field quantitative phase imaging with low spatial coherence illumination. In the following chapter, we introduce a second off-axis DHM system, with a key advantage of continuous variable magnification, field of view and numerical aperture by simply moving the sample. It will be shown the proposed architectures borrows from the principles of DIHM, which is described in Chapter 2.

Chapter 4

Off-axis DHM with continuous variable magnification, field of view and numerical aperture

4.1 Introduction

This chapter is on the preparation to be published as part of the following paper:

- Xin Fan, Bryan Hennelly, *Method for off-axis digital holographic microscopy with continuously variable magnification, field of view, and numerical aperture.* In preparation for submission to Journal of advanced photonics.

The goal of this thesis is to explore the cellular morphology of quantitative phase images of unstained biological samples, which are essentially invisible in ordinary bright-field microscopy, by digital holographic microscopy. In Chapters 1 and 2, we reviewed the theory behind digital holography and in Chapter 3 we proposed a novel DHM interferometer with a compact structure for full-field quantitative phase imaging with low spatial coherence illumination. In this chapter, we introduce a second off-axis DHM system, with a key advantage of continuous variable magnification, field of view and numerical aperture by simply moving the sample. It will be shown the proposed architectures borrows from the principles of DIHM, which is described in Chapter 2.

As described in Section 2.7, DIHM has the wonderful advantage of variable magnification/field of view but the critical disadvantages of not being able to produce quantitative phase information as well as requiring the weak transfer function approximation with a single capture. The focus of this chapter is to develop an optical system that retains the advantage of variable magnification/field of view but also provides the quantitative phase information about the sample and furthermore requires no assumption regarding the transmittance of the sample. It will be shown that this can be achieved using an optical system that utilizes the off-axis interference

principle and is broadly similar to the experimental off-axis DHM system that was described in Section 2.6 in Chapter 2; the proposed system also incorporates the idea of diverging illumination, which is borrowed from the DIHM modality. Indeed, it will be demonstrated that any existing DHM system may be altered slightly (a single Fourier transforming lens is inserted into the object path) such that variable magnification is achievable by simply moving the sample.

In Section 4.2 we review the optical set up for in-line Gabor holography, which is the basis for DIHM. Following this, we introduce the basic idea of the off-axis system that is proposed in this chapter, which borrows from the ideas that are inherent to Gabor holography. In Section 4.3 the proposed experimental system is described in detail and in Section 4.4 the ABCD ray transfer matrix for the system is used to design a reconstruction algorithm. Ray tracing is used in Section 4.5 in order to estimate the numerical aperture and field of view of the system for each object position in the continuous space that exists between the point source and the microscope objective that is used in the set-up. An initial set of experimental results are presented in Section 4.6 followed by a brief conclusion in Section 4.7.

4.2 The principle of off-axis DHM with variable magnification

In Section 2.7 in Chapter 2 the theory of DIHM was presented and it was shown that this approach could be used to record images of microscopic samples with a continuously variable magnification by moving the sample position in the set-up. The goal in this section is to outline a basic approach for incorporating this functionality into the traditional off-axis DHM architecture. The principle of the approach is illustrated in Fig. 4.1(b) beside which we reproduce the image that appeared earlier in the thesis for the DIHM set-up for ease of comparison, see Fig.4.1(a).

For both set-ups, a spherical beam emerges from a pinhole with a wavelength λ . Following propagation of a distance d this diverging spherical field is incident upon a transmissive object, which introduces a phase delay that we denote as $o(x)$, which is identical to the DIHM case shown in Fig. 4.1(a). In the case of DIHM, an intensity pattern is recorded by a camera a further distance z away from the object plane, and this intensity pattern is assumed to contain an interference pattern between the wavefield scattered by the weak object and the unscattered field. For the system proposed here, a microscope objective (MO) replaces the camera in the same plane. In this way, we will demonstrate that it is possible to overcome the limitations of DIHM. We recall from Section 2.7 that under a set of assumptions, DIHM provides for $O(x)r_f^*(x)$ to be approximately recovered, from which $o(x/M)$ can be approximately reconstructed; in this way it was possible to reconstruct an approximate image intensity $|o(x/M)|^2$ of the magnified object. However, the

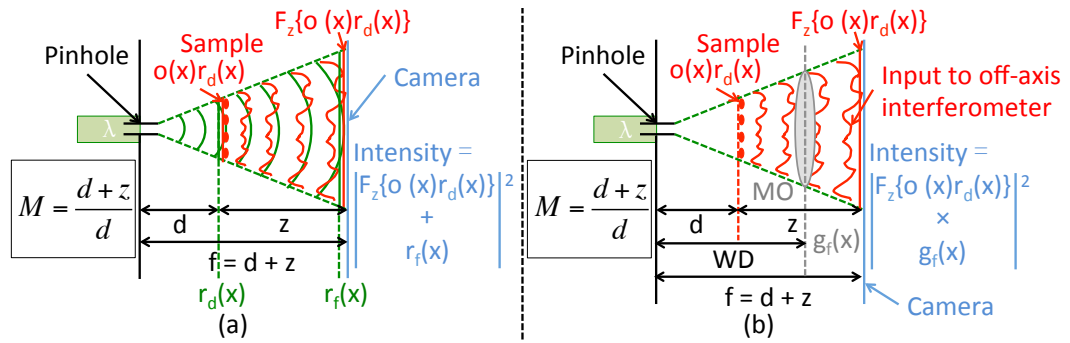


Fig. 4.1 The physical set-up shown in (a) is a Gabor set-up with a spherical diverging beam, $r(x)$, emerging from a pinhole, illuminating an object, $f(x)$, a distance d_1 away. Immediately behind this plane there is an object wave $o(x)r(x)$. The interference pattern, $H(x')$, between the propagated reference wave, $R(x')$, and the propagated object wave, $O(x')$, is captured on a CCD a further d_2 away. This capture is the input to the numerical reconstruction part of the imaging system which is described in detail later.

presence of the other three terms in the intensity pattern results in corruption of the phase image. Furthermore, the DIHM modality is very much dependent on the weak object transmission function assumption.

For the proposed system illustrated in Fig. 4.1(b) we do not need to make any assumption about the weakly scattering object, since we do not need to rely upon the unscattered wavefront $r_f(x)$ to generate an interference pattern. By selecting an MO with focal length, $f = d + z$, the effect of the lens can be described as a chirp function that is similar to the unscattered wavefront in the interference pattern in DIHM, i.e. the field in the output plane of the MO can be described as $O(x)r_f^*(x)$, which is identical to the real image term in the DIHM hologram. In our case, however, this term is not corrupted by the presence of the other three terms and an off-axis DHM architecture can be used to record it in isolation, which can provide for a reconstruction of the quantitative phase image of $o(x/M)$. The exact optical system that is used to do this is described in Section 4.3. It will be shown in the following sections, that the proposed system has magnification M that is identical to the magnification term in DIHM, and that the magnification, field of view, and numerical aperture can be continuously varied by moving the sample.

4.3 Experimental System

For practical reasons it is more efficient to replace the pinhole in Fig. 4.1(b) with a focused spot from a condenser lens, which in this case is a microscope objective with numerical aperture matching that of the imaging MO. A laser is collimated and expanded to fill the back aperture of the condenser lens, thereby producing a diffraction limited spot in lieu of the pinhole used in the previous description.

This simplifies the positioning of samples close to the point source. In Fig. 4.2 the optical set up that is custom built in our laboratory is illustrated; the same partially coherent laser diode source (CNI Laser MGL-III-532) is used as for the previously described set-up in Section 2.6. The laser operates at a power of $< 10 \text{ mW}$ and with a wavelength of 532 nm and is coupled to a single mode optical fiber (Thorlabs; FC532-50B-FC) which splits into two output fibers with a 50/50 power ratio. The first fiber output is collimated by a plano-convex lens with focal length 5 cm and passes through a linear polariser (Thorlabs; LPVISE100-A) and a condenser lens (Olympus; UMplanFl 50x/0.8) to illuminate the sample. The condenser focuses

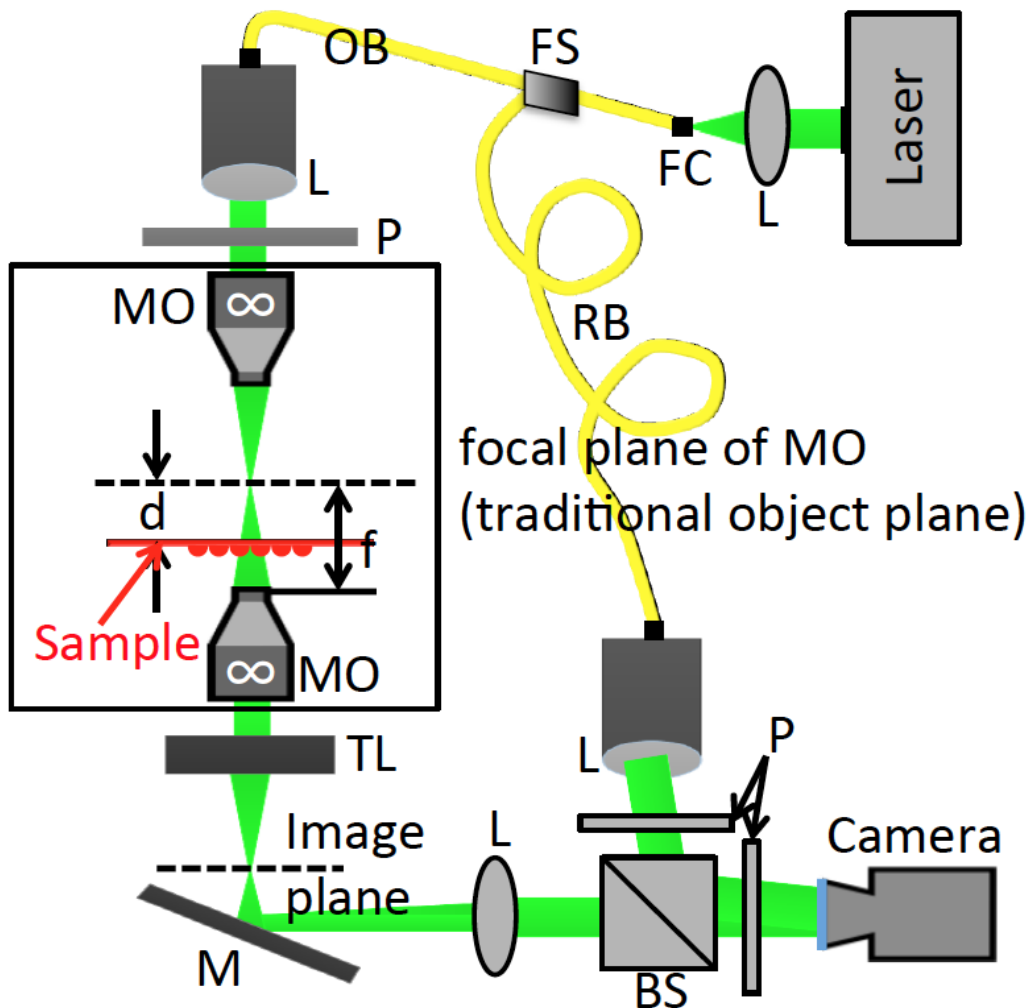


Fig. 4.2 Optical setup of off-axis digital holographic microscopy with variable magnification. L: Lens; FC: Fiber Coupler; FS: Fiber Splitter; P: Polarizer; MO: Microscope Object; TL: Tube Lens; PBS: Beam Splitter; OB: Object beam; RB: Reference beam.

the collimated beam to a diffraction limited spot at the traditional object plane of a second microscope objective, (Leitz; $32 \times L/0.6$) which has a numerical aperture of 0.6 and a long working distance of approximately $WD \approx 3.5 \text{ mm}$. Both of the

MOs used in the set-up are infinity corrected, and therefore they are separated by the sum of their working distances, and the focused spot is located a focal length away from both. The sample is located at some plane a distance d from that focused spot immediately before the $32\times$ MO. The sample is mounted on an electronic translation stage (ASI; MS-2000, LS-50, LX-4000) capable of moving the sample in all three spatial dimensions with less than $1\mu m$ accuracy. The wavefield that is scattered by the object then passes through the $32\times$ MO, and an infinity corrected tube lens with focal length 200mm (Thorlabs; TTL200) and a convex lens also with 200mm focal length (Thorlabs; LB1945-A) which is positioned 200mm from the traditional image plane at the back of the tube lens. The object wavefield propagates through polarising cube beam splitter (Thorlabs; PBS252), a second linear polariser (Thorlabs; LPVISE100-A) to a CMOS sensor (Basler; acA200-340km) which has 2048×1088 pixels of size $5.5\mu m$.

The second fiber is used to generate the reference; the output of the fiber is collimated and polarised as for the case of the object wavefield. Both wavefields are combined using the polarising beam splitter (PBS), The final linear polariser that is used immediately before the camera ensures high hologram diffraction efficiency. All optical elements were obtained from Thorlabs with anti-reflection coating for the visible region. The coherence length of the laser is approximately 0.1 mm , which ensures that noise from back reflections is reduced; this requires that the path lengths are suitably matched, which is achieved by using different fiber lengths for both paths. The experimental setup of off-axis digital holographic microscopy with variable magnification in our lab is shown in Fig. 4.3.

By ensuring that the reference wave is a plane wave that is propagating at a small angle with respect to the camera normal, as described by the equation below:

$$R(x,y) = \exp(j2\pi[x\sin(\theta_x) + y\sin(\theta_y)]/\lambda), \quad (4.1)$$

where θ_x and θ_y denote the angles with respect to the camera normal in both the x and y directions respectively, and λ denotes the laser wavelength, it can be shown that the latter two terms in Eq. 2.22 become separated from the other terms in the spatial frequency domain[1] and can be isolated by filtering using the discrete Fourier transform (DFT)[18]. This is possible if the support of the object wavefield in the spatial frequency domain is sufficiently limited and the frequency shift imparted by the angle of the reference is sufficiently large; for more details see Chapters 6 and 9 of Goodman[1]. In the following section, this system is further investigated and it is shown that the mapping between the sample plane and the camera plane can be defined using a simple Fresnel transform and a variable magnification that is equivalent to that provided by DIHM.

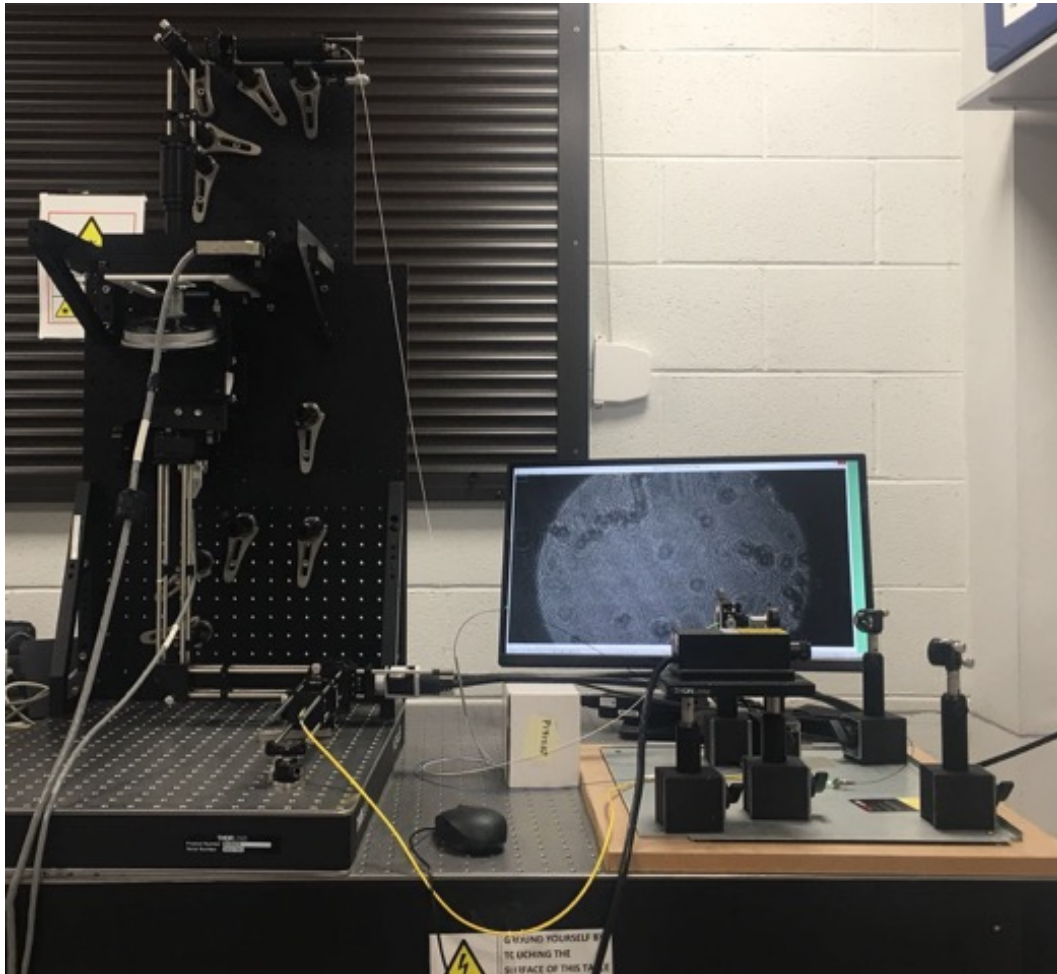


Fig. 4.3 Experimental setup of off-axis digital holographic microscopy with variable magnification in our lab.

4.4 Numerical reconstruction

The overall system that maps in the object plane to the camera plane is illustrated in Fig. 4.5. Contrary to convention, light propagates from the input (sample) plane, which is located on the right of the figure, towards the output (camera) plane on the left of the figure. The reason for this is to facilitate the correct ordering of the matrices that are associated with each of the different optical elements that make up the system, in the matrix product that describes the system. The overall matrix product is shown immediately beneath the diagram of the system and arrows are used to relate each element to its corresponding matrix. The values of d , z , and

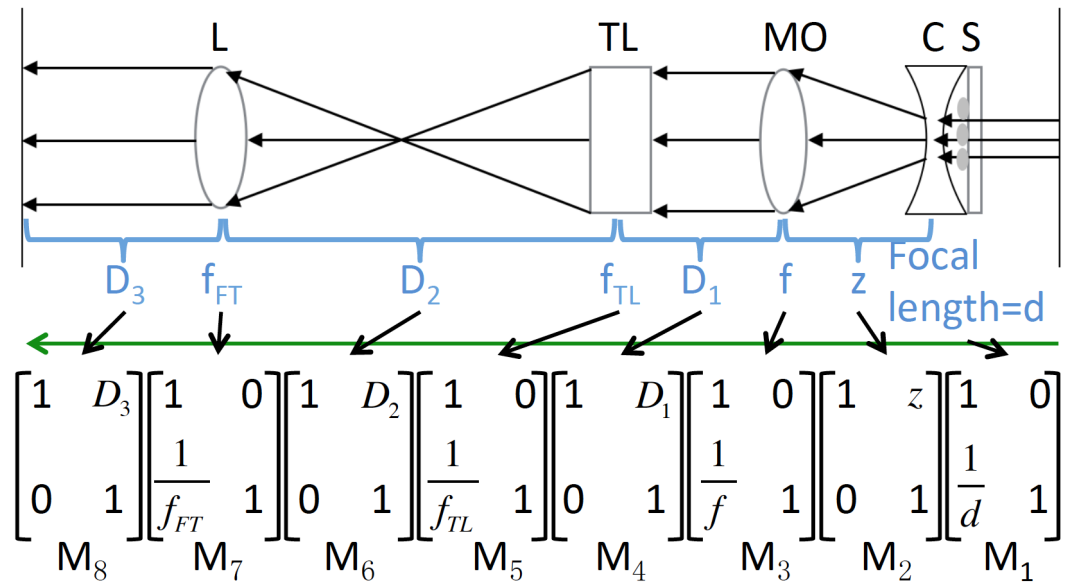


Fig. 4.4 Illustration of the optical system that maps the input sample plane to the output camera plane; S, Sample; C, Complex lens; MO, Microscope objective; TL, Tube lens; L, Fourier transforming convex lens. Here, the divergent spherical illumination is represented as a convex lens of focal length d in the plane immediately after the sample plane and coherent plane wave illumination is assumed.

f_{MO} that appear in Fig. 4.4 are equivalent to the parameters described in Fig. 4.1. In Fig. 4.4, plane wave illumination is assumed and, in this way, it is possible to describe the effect of the diverging illumination as being equivalent to the effect of a convex lens of positive focal length d . The focal length of the MO and the tube lens are represented by f_{MO} and f_{TL} , respectively, and the focal length of the third lens (performing an optical transform of the traditional image plane) is denoted f_{FT} . D_1 , D_2 , and D_3 denote sections of free space between the MO and tube lens, between the tube lens and Fourier transforming lens, and between this latter lens and the camera plane, respectively. Matrices for each of the optical elements are shown directly below and are denoted as M_1 to M_8 from right to left as indicated in the figure and these matrices are used in the next section, which deals with estimating the numerical aperture of the microscope for any given sample position by applying geometrical

ray tracing using these eight matrices. We define the following relationships between the various parameters:

$$f_{MO} = z + d \quad (4.2a)$$

$$D_2 = f_{TL} + f_{FT} \quad (4.2b)$$

$$D_3 = f_{FT} \quad (4.2c)$$

The first of these relationships, defined in Eq. 4.2a was previously discussed in Section 4.2 and ensures that the first part of the optical system relates closely to the DIHM system (including the multiplication with the unscattered reference wavefront). The second relationship defined in Eq. 4.2b ensures that the lens f_{FT} is located a focal length away from the traditional image plane of the microscope, i.e. the plane in which the illuminating point source in Fig. 4.2 will converge to a point. The third relationship given in Eq. 4.2c implies that the camera is located at the back focal plane of f_{FT} . Therefore, the lens f_{FT} performs an optical Fourier transform between the traditional image plane and the camera plane and it becomes clear that the point source illumination will be transformed into a plane wave in the camera plane. If these three relationships are satisfied, it is straightforward to show that the matrix product defined in Fig.4.4, which represents the optical transformation between the sample plane and the camera plane, reduces to a simplified form as follows:

$$\begin{aligned} M_8 M_7 M_6 M_5 M_4 M_3 M_2 M_1 &= \begin{bmatrix} M & \frac{q}{M} \\ 0 & \frac{1}{M} \end{bmatrix} \\ &= \begin{bmatrix} 1 & q \\ 0 & 1 \end{bmatrix} \begin{bmatrix} M & 0 \\ 0 & \frac{1}{M} \end{bmatrix} \end{aligned} \quad (4.3)$$

where,

$$q = f_{FT} \left[1 - \frac{1}{f_{TL}} (zM + D_1) \right] \quad (4.4a)$$

$$\text{and } M = \frac{d+z}{d} = \frac{f}{d} \quad (4.4b)$$

The definition for the magnification, M , in Eq. 4.4b is identical to the definition of magnification for the case of DIHM. It is also interesting to note that this simplification is entirely independent of the value of D_1 , which is the distance between the microscope objective and the tube lens. This freedom is also found with any imaging system that uses infinity corrected microscope objectives like the one used in this study. These objectives are designed to image at a plane at infinity and are standard in all life-science microscopes that employ fluorescence cubes to be inserted behind the objective, which will inevitably delay the wavefront passing through. Based on Eq. 4.3 and following from the discussion in Section 4.4 we may conclude that the relationship between the sample plane and the camera plane is

simply a magnification of the object wavefield $o(x)$ followed by a Fresnel transform with distance parameter q .

It is possible to define a simple reconstruction algorithm by inverting the right hand side of Eq. 4.3 as follows:

$$\begin{bmatrix} \frac{1}{M} & 0 \\ 0 & M \end{bmatrix} \begin{bmatrix} 1 & -q \\ 0 & 1 \end{bmatrix} \quad (4.5)$$

Following the capture of a raw hologram and the spatial filtering step in the DFT domain[18], reconstruction, therefore, consists of simulating the Fresnel transform using the method previously described in Section 2.3.3 which consists of two DFT operations, which can be implemented in real-time using the fast Fourier transform algorithm[42, 144, 145]. If the value of q is not known exactly, perhaps because the value of d or D_1 is not known precisely, then an autofocus algorithm can be applied, similar to that described in Chapter 5 and elsewhere[86, 104].

4.5 Numerical aperture, field of view, magnification

The magnification that is provided by the overall imaging system proposed in Section 4.3 and Section 4.4, by which we mean the combination of optoelectronic recording of the hologram, followed by algorithmic numerical reconstruction of the image of the sample, is given in Eq. 4.4b. A simple inspection of this equation reveals that the largest magnification that is achievable is infinity, $M_{max} = \infty$, which occurs when the sample is placed in the same plane as the point source, i.e. when $d = 0$. The smallest magnification that is achievable occurs when the sample is placed as close as possible to the MO, i.e. at the largest possible value of d . As discussed in Section 4.2, the working distance, WD , of the MO will in general be shorter than the focal length of the MO, f . Therefore, the smallest magnification is given by:

$$M_{min} = \frac{f}{f - WD} \quad (4.6)$$

The smallest magnification, therefore, will always be greater than one. The ratio of the working distance to focal length varies significantly across microscope objectives but can be assumed to be < 2 for long working distance objectives, such as the one used in this study. In such cases, it can be assumed that $M_{max} < 2$. Using the magnification, it is also possible to calculate the field of view, FoV , of the resultant image by simply dividing the sensor area, w , by the magnification to provide:

$$FoV = w/M \quad (4.7)$$

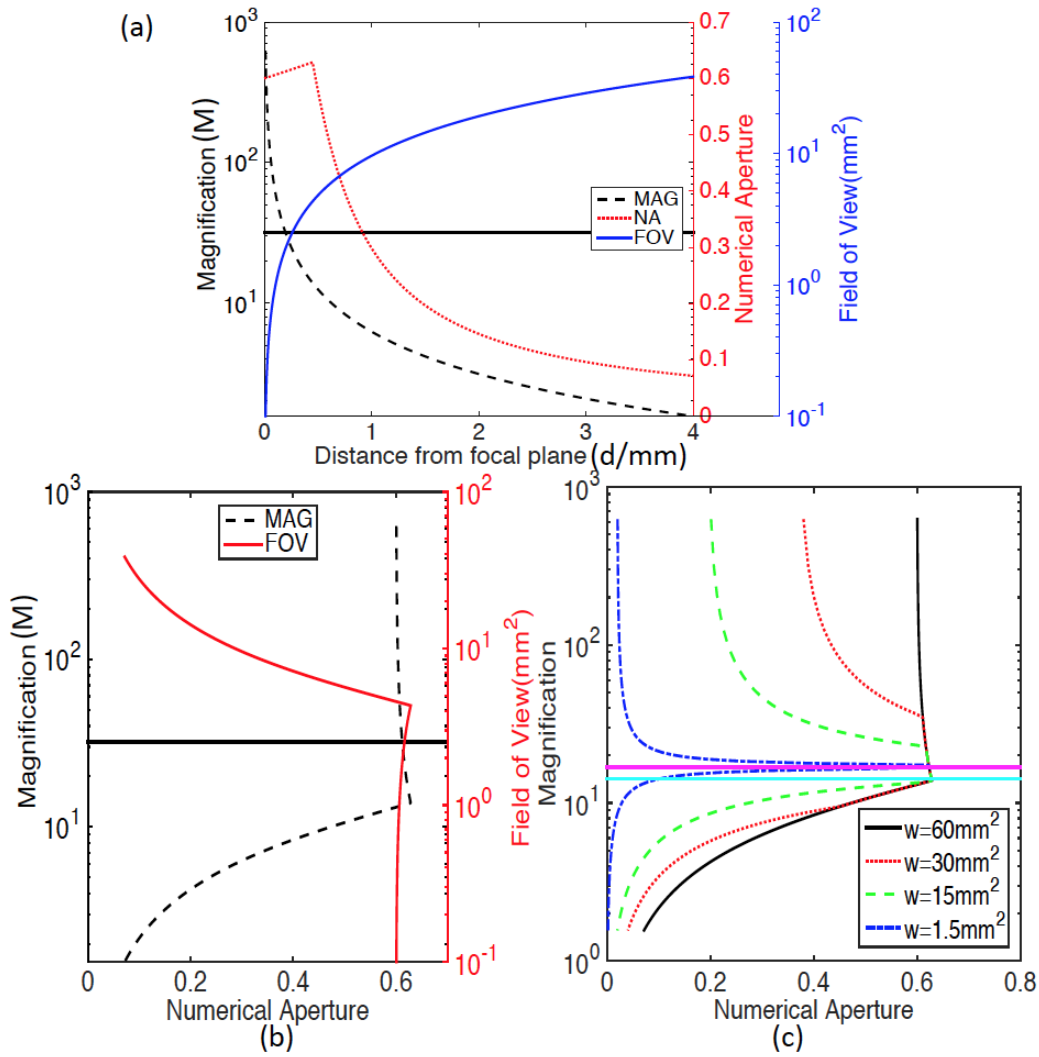


Fig. 4.5 The relationships between magnification M , field of view FoV and numerical aperture NA for the setup shown in Fig. 4.2; (a) shows the variation in M , FoV , and NA as a function of sample position d in the set-up; (b) M and FoV both plotted as a function of NA ; and (c) the relationship between M and NA for a range of different sensor sizes, w .

The value for FoV will vary from 0, for the case of M_{max} to $> w/2$ for the case of M_{min} , i.e. it should be possible to record a field of view at least half the area of the recording sensor. In Fig. 4.5(a) the magnification and field of view are both shown as a function of the sample position d . The microscope objective used in the study is a Leitz $32\times$ L microscope objective infinity corrected long working distance with a NA of 0.6, which has a focal length of $f = 6.25mm$ and a working distance of approximately $WD \approx 3.5mm$. The range of values of d , therefore, over which the M and FoV are calculated is from $0mm$ up to $4mm$. It can be seen that M decreases rapidly from an infinitely high value at $d = 0$ to a value of $M = 7$ over the first $1mm$ from the point source. In contrast, the FoV decreases inversely over this range.

However, despite the ease with which magnification and field of view can be defined, it is not immediately obvious what the numerical aperture (NA) of the overall imaging system will be. It can be expected that the numerical aperture will vary depending on the position of the sample plane relative to the MO, since this will change the angle that relates the centre of the object on the optical axis, to the edge of the MO. However, these rays that propagate at the most extreme angles into the MO, might not be captured through the apertures of one or more of the remaining optical elements. Therefore, in order to determine the NA for a given sample position d is necessary to perform ray tracing using the matrices for each of the optical elements in the system. This can be done systematically, such that for the centre point on the sample, the maximum ray angle can be determined that will pass through each individual element. As an example, consider the tube lens. The position, x' and angle θ' of a ray that originates at the centre of the sample (position $x = 0$) propagating at an angle θ can be calculated as follows [1]:

$$\begin{bmatrix} x' \\ \cos^{-1} \theta' \end{bmatrix} = M_2 M_1 \begin{bmatrix} 0 \\ \cos^{-1} \theta \end{bmatrix} \quad (4.8)$$

Therefore, the position of the ray in the plane of the tube lens is given by:

$$x' = B \cos^{-1} \theta \quad (4.9)$$

where B is the parameter from the $ABCD$ ray transfer matrix that is given by $M_2 M_1$. The maximum value of x' is given by the radius of the tube lens and in this way, the maximum ray angle from the sample centre that can pass through the tube lens can be calculated. The same procedure can be applied for the third lens in the system f_{FT} and for the camera. The position of the ray in these two planes is also given by Eq. 4.8 where the B parameters is taken from the two matrix products, $M_6 M_5 M_4 M_3 M_2 M_1$ and $M_8 M_7 M_6 M_5 M_4 M_3 M_2 M_1$ respectively. In practice, for the components used in this study, it was found that, in addition to the aperture of the MO, the limiting aperture was in general defined by the camera aperture. The numerical aperture is also plotted as a function of sample position d in Fig. 4.5(a), in which it

can be seen that the intended NA of the MO (0.6) can be approximately achieved for a range of different magnifications and $FoVs$. At a distance of $d = 0.3mm$ the magnification of the system $M = 32$, which is marked by a horizontal line in the figure; interestingly, this is the intended magnification of the MO, and at this position the NA is slightly greater than the design value of 0.6. From a position of $d = 0.5mm$ corresponding to a magnification of $M = 10$ the NA begins to drop rapidly as the d increases. At a value of $d = f$, which corresponds to a magnification of $M = 1$, it can be seen that the NA has dropped to a value of 0.07.

In Fig. 4.5(b) M and FoV are both plotted as a function of the numerical aperture. It can be seen that for a range of different magnifications, from $10 < M < \infty$ the maximum NA of approximately 0.6 can be obtained. Below a value of $M = 10$ the NA drops in an approximately linear manner as a function of NA . Conversely, the FoV decreases linearly for values of $0.07 < NA < 0.6$. It was found that the camera aperture played an important role in defining the relationship between NA and M . In Fig. 4.5(c) this is explored by relating M and NA for a range of different square sensor area wmm^2 , where all other parameters are the same as those defined in Section 4.3. For the smallest sensor area investigated, $w = 1.5mm^2$ it can be seen that the maximum NA of 0.6 can only be achieved for a particular sample position corresponding to a magnification of $M = 10.8$ denoted by the pink line in the figure. Deviation from this position to provide any other magnification results in a sharp decrease in NA . This constraint relaxes as we increase the sensor area in the sense that the range of values of M that can provide the maximum NA widens as a function of w .

4.6 Results

In this section, the results are shown for a microlens array sample (Suss MLA 18-00028 quartz, circ. lenses, quad. grid, pitch $110 \mu m$, ROC $6.188mm \pm 5\%$, no AR-Coating, size $10mm \times 10mm \pm 0.05 mm$, thickness 0.9 mm, rectangular shape). The sample was placed in a range of different positions and the results are shown in Fig.4.6 and Fig.4.7 for three different values of d corresponding to magnifications of $M = 32$, which is the design magnification of the MO, $M = 12$, and $M = 5$. The reconstructed intensity and phase images are shown for the three cases in Fig. 4.6(a)-(f) following spatial filtering with the DFT to isolate the real image, followed by simulation of Fresnel propagation of distance q using the spectral method as discussed in previous sections. In this case no attempt is made to perform aberration compensation. The sample position d is shown in the top right corner of each intensity image, and the values of NA and FoV are also shown in each intensity image, which have been calculated using the formula defined in Section 4.5 and Section 4.4. The same set of results are shown in Fig. 4.7(a)-(f) where in this case aberration compensation is applied using the method described in Ref. [104], which

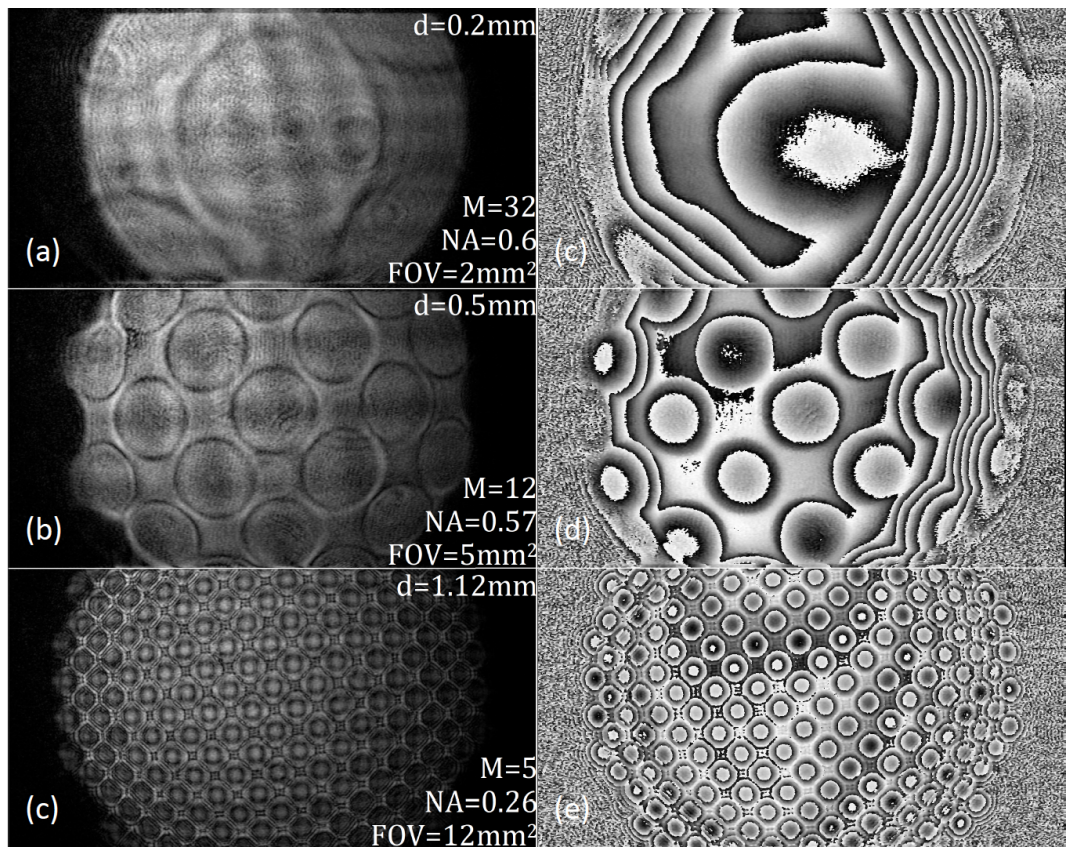


Fig. 4.6 Raw amplitude and wrapped phase images of microlens array for different magnifications.

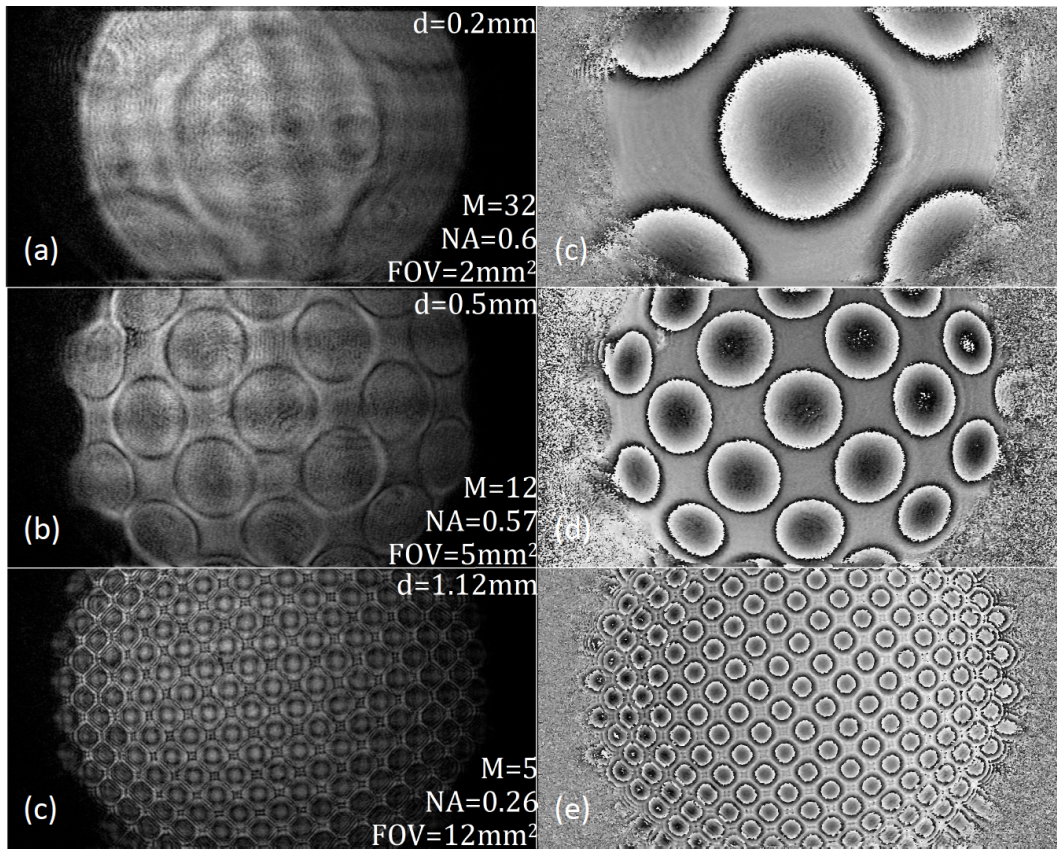


Fig. 4.7 Amplitude and wrapped phase image of microlens array after compensation with same magnifications shown in Fig. 4.6.

makes use of a reference conjugated hologram. This form of aberration compensation is minimalist, whereby a reference hologram is recorded with no sample, and the resulting complex hologram is divided into the hologram of the object prior to reconstruction, and several more detailed forms of aberration compensation have been developed[104, 20, 105, 103].

Although this attempt to compensate for aberrations clearly improves the phase image, it only partially corrects for aberration. The reason for this, is that this method of aberration compensation relies on the assumption that there exists only phase aberration in the hologram plane, which may be true for other systems that use a camera position close to the back aperture of the MO, and use the MO at the correct working distance from the sample; it is only at this distance the MO has been designed to have little or no value for the Zernike polynomial coefficients. Clearly, in our case this assumption that no image distortion will occur in the CCD plane is not satisfied; indeed, a curvature is visible in the hologram itself, (not shown here), which is also visible in the reconstruction plane. Further work is required in order to fully solve the problem of aberration compensation for the variable magnification system proposed here; this is discussed in more detail in Section 4.7.

4.7 Conclusion

In this chapter, a novel system for off-axis digital holographic microscopy is proposed that has the capability to provide for continuously variable magnification over a range of values from approximately two times up to infinity, by simply moving the position of the sample in the set-up. In Section 4.2 the basic principle of the proposed method was discussed and it was shown that the way in which the magnification is defined is identical to the case of digital inline holographic microscopy, which is based on Gabor's original system. Unlike DIHM, however, the proposed system provides full quantitative phase images in a single capture and requires no preconditions on a weakly scattering object. In Section 4.3 the experimental system was described in detail and in Section 4.4 the ray transfer matrix for the system was used to derive the relationship between the sample plane and the camera plane, which was demonstrated to be defined by a single magnification step and a Fresnel transform. In Section 4.5, the ray transfer matrix of each component in the set-up was used to calculate the largest angle of light from the centre of the sample that could be recorded by the camera and in this way the numerical aperture of the system for each sample position and magnification could be calculated.

The experimental results presented in Section 4.6 clearly demonstrate the usefulness of the method by imaging a microlens array sample over a range of magnifications and field of views. One shortcoming of the method is the manifestation of aberrations in the final reconstructed image. This was briefly discussed in Section 4.6 and we expand on that discussion here. In Section 4.6 the method used for aberration

compensation was the simplest possible method whereby we simply divide by a reference conjugate hologram in the hologram plane. This method works well for the case where the hologram plane is close to the back of the MO and the MO is imaging at the correct image plane for which it was designed. In such a case it can be expected that only phase aberrations will manifest in the hologram plane, which is clearly not the case for the system proposed here. Of particular concern is the fact that the MO is being used to image a sample that is placed very far from the expected image plane for which the MO was designed to image with little aberration. Also of concern is that fact that the aberrations from two different microscope objectives are contributing to image distortion. The condenser MO effectively produced the concave lens in the sample plane, which will contain the aberrations from that lens. Nevertheless, a complete distortion compensation is likely possible by applying aberration compensation in two different planes as described elsewhere[104, 20, 105], and also possibly by measuring the aberrations to both of the MOs separately. It is also possible that the process of aberration compensation could be simplified by using the set-ups that record the hologram immediately behind the microscope objective such as that used in other studies[104, 8].

A final point of note is the microscope objective. The proposed method will provide a large range of magnification only if there is a large working distance, i.e. a large range of travel in front of the MO. This feature is provided by long working distance objectives such as the one used in this chapter. MOs with even longer working distances are available from other sources like Mitutoyo and it will be interesting to see if other researchers investigate their potential in future work.

In this section, we have proposed a novel method for recording and reconstructing in digital holographic microscopy with the new features of variable magnification, field of view and numerical aperture, which is achievable by simply moving the sample. The remaining three chapters in this thesis focus on processing the quantitative phase images that have been obtained following recording.

Chapter 5

An investigation of sparsity metrics for autofocusing in DHM

5.1 Introduction

This chapter has been published as part of the following papers:

- Xin Fan, John J. Healy, and Bryan M. Hennelly. *Sparsity metrics for autofocus in digital holographic microscopy*. in SPIE Photonics Europe, 989619–989619, International Society for Optics and Photonics (2016).
- Xin Fan, John J. Healy, and Bryan M. Hennelly. *Investigation of sparsity metrics for autofocusing in digital holographic microscopy*. *Optical Engineering* 56.5 (2017): 053112. (2006): 3177-3190.

The goal of this thesis is to explore the cellular morphology of quantitative phase images of unstained biological samples, which are essentially invisible in ordinary bright-field microscopy, by digital holographic microscopy. In the previous chapters, we reviewed the theory behind holography and quantitative phase imaging, and proposed two novel recording and reconstructing methods for DHM. In this chapter, we quantitatively evaluate, compare and classify the performance of sparsity based autofocusing metrics in terms of accuracy and reliability, by applying DHM to the sequence of intensity or amplitude images in step of distances recovered by the numerical reconstruction algorithm as described in Section 2.6.

As discussed in Section 2.6.6, a key advantage of DHM over conventional microscopy is that both the phase and intensity information of the object can be recovered at any distance, using only one capture, and this facilitates the recording of scenes that may change dynamically and which may otherwise go in and out of focus. Autofocusing using traditional microscopy requires mechanical movement of the translation stage or the microscope objective, and multiple image captures that are then compared using some metric. Autofocusing in DHM is similar, except

that the sequence of intensity images, to which the metric is applied, is generated numerically from a single capture.

The motivation of this chapter is to advance the current understanding of autofocus metrics in DHM in a number of ways: (i) We propose several new sparsity metrics for DHM; (ii) We qualitatively and quantitatively evaluate the performance of 32 sparsity metrics across a range of different holograms recorded with different numerical apertures; a number of different diatom cells are used to generate the holograms and the various sparsity metrics are compared to previously proposed DHM autofocus metrics including the variance of the intensity; (iii) Although all of the autofocus metrics proposed in DHM to date are designed to achieve the same outcome, their behavior differs significantly both in term of the autofocus distance that is returned, and the variation of each metric as a function of propagation distance. To date, there has been no effort to understand or relate the behavior of these various metrics, and this is one of the core objectives of this chapter. We demonstrate that the majority of the sparsity metrics that are investigated here exhibit matching behavior following high pass filtering. Furthermore, we demonstrate that this methodology can be extended to other well-know metrics including variance, thereby providing a possible framework for a unified understanding of autofocus metrics in DHM.

In Section 5.2, sparsity metrics that are used in this chapter are discussed and the concept of applying the Savitzky-Golay filter in order to improve the performance of these metrics is also introduced. In Section 5.3 the results are presented for three example holograms over two magnifications in both graphical and tabulated format. Finally, a discussion and conclusion are offered in Section 5.4 and 5.5.

5.2 Sparsity metrics

Sparsity metrics are often applied in signal processing for compression [33, 34] and source separation[35, 36] and they have recently been proposed as potential autofocus metrics in digital holography.[93, 97, 94, 95] The concept of sparseness is based on representing the majority of a signal energy using a reduced number of elements from a chosen basis set[146, 2]. *P. Memmolo et al.*[93, 97] recently investigated the Gini index, a well known sparsity metric, for autofocusing in DHM.

The behavior of autofocus metrics varies for amplitude objects (by which we mean objects or samples that have scattering and/or absorption properties) and phase objects, examples of which are stained and unstained epithelial cells, respectively; the metric is maximum for the case of an in-focus amplitude image, while returning a minimum for an in-focus phase only image. Since all of the objects that are analyzed in this chapter are unstained diatom cells, we expect the various sparsity metrics under investigation will return a minima value at the image plane.

In this section, 32 sparsity metrics are investigated for their suitability for autofocusing in DHM based; Table 5.1 lists the definitions of the sixteen core sparsity

metrics, which are based on the two dimensional real valued signal, $I(n_x, n_y)$. The first 16 metrics that are investigated are based on setting I equal to the reconstructed 2D image intensity of the digital hologram, i.e. $I(n_x, n_y) = |o(n_x \delta_x, n_y \delta_y)|^2$, and the second set of 16 metrics are based on setting $I(n_x, n_y) = |o(n_x \delta_x, n_y \delta_y)|$.

The first sparsity metric, ℓ_0 , is based on the definition of sparseness as the number of non-zero elements. However, in practical applications, the majority of non-zero components are small enough to contribute very little to the information content of the signal. A direct replacement for this metric is the ℓ_0^ϵ norm; however, it may be difficult to determine the most suitable value of ϵ . We have already described the second to sixth metrics, ℓ_p and ℓ_0^ϵ norm-like metrics and some extensions[94], which are often employed instead of the ℓ_0 norm. For the case of ℓ_0^ϵ , the value of ϵ is set to $0.1 \times \overline{I(n_x, n_y)}$ where $\overline{I(n_x, n_y)}$ denotes the mean value of I . The seventh metric $-\tanh_{a,b}$ is an approximation of the ℓ_0^ϵ norm, the main difference being that the output of $-\tanh_{a,b}$ saturates to 1 when the input values become very large[147]. The values of parameters a and b in the $-\tanh_{a,b}$ metric should be positive real values and b must be greater than 1. In our study, we chose 1 divided by the maximum value of I and a and b are both set equal to 4 in order to obtain the best performance. The highest-density interval, u_θ , is a nonparametric sparsity metric that implicitly adopts a similar concept to that of the ℓ_0^ϵ norm, whereby θ is not a parameter. Sorting the input elements is necessary and then finding the smallest range that contains a specific percentage, θ , of the total range of values. The -log measure is concave outside some range, but convex near the origin, which in effect spreads the small components. The Kurtosis metric has been used as a measure of sparseness and as an approximation of the entropy[147].

The final metric in the list in the Tab. 5.1, the Gini index was originally introduced in 1921 as a measure of inequality of income[148] and also has been used to study the sparseness of the wealth distribution[149, 150]. The application of the Gini index to a two dimensional real valued image, involves reshaping the values of the image pixels into a vector, $I = \{I(1, 1), I(1, 2), \dots, I(N_x, N_y)\}$; this vector is then sorted according to the values from minimum to maximum, $|I_1| \leq |I_2| \leq \dots \leq |I_N|$, where after the operation of sorting, $1, 2, 3, \dots, N$ are the new indices of the elements of the vector and $N = N_x \times N_y$. The Gini index is derived from the Lorenz curve, originally defined in the work of Lorenz *et al*[151], as follows

$$\text{Gini}(I) = 1 - 2A(I) \quad (5.1)$$

where $A(I) = \frac{1}{2N} \sum_{n=1}^N [L(\frac{n-1}{N}) + L(\frac{n}{N})]$ can be described as the area between the 45 degree line[152]. The Lorenz curve is given by

$$L\left(\frac{i}{N}\right) = \sum_{j=1}^i \frac{|x_{(j)}|}{\sum_{k=1}^N |x_k|} \quad (5.2)$$

Therefore, the Gini index can be derived from Eq. 5.1 as follows,

Table 5.1 Full list of sparsity metrics applied in this chapter for autofocusing in digital holographic microscopy. Note these metrics are based on those found in the work of Hurley *et al*[2], and have been adapted for two dimensional real valued images.

Name	Definition
ℓ^0	$\# \{I(n_x, n_y) = 0\}$
$-\ell^p$	$-\left[\sum_{n_x=0}^{N_x-1} \sum_{n_y=0}^{N_y-1} I^p(n_x, n_y) \right]^{\frac{1}{p}}, 0 < p < 1$
$-\ell^p_-$	$-\sum_{n_x=0}^{N_x-1} \sum_{n_y=0}^{N_y-1} I^p(n_x, n_y), p < 0$
$-\ell^1$	$-\left[\sum_{n_x=0}^{N_x-1} \sum_{n_y=0}^{N_y-1} I(n_x, n_y) \right]$
ℓ_ε^0	$\# \{I(n_x, n_y) \leq \varepsilon\}$
$\frac{\ell_2}{\ell_1}$	$\frac{\sqrt{\sum_{n_x=0}^{N_x-1} \sum_{n_y=0}^{N_y-1} I^2(n_x, n_y)}}{\sum_{n_x=0}^{N_x-1} \sum_{n_y=0}^{N_y-1} I(n_x, n_y)}$
$-\tanh_{a,b}$	$-\sum_{n_x=0}^{N_x-1} \sum_{n_y=0}^{N_y-1} \tanh\left((aI(n_x, n_y))^b\right)$
$-\log$	$-\sum_{n_x=0}^{N_x-1} \sum_{n_y=0}^{N_y-1} \log(1 + I^2(n_x, n_y))$
Kurtosis	$\frac{\sum_{n_x=0}^{N_x-1} \sum_{n_y=0}^{N_y-1} I^4(n_x, n_y)}{\left(\sum_{n_x=0}^{N_x-1} \sum_{n_y=0}^{N_y-1} I^2(n_x, n_y)\right)^2}$
u_Θ	$1 - \min_{i=1,2,\dots,N-\lceil\theta N\rceil+1} \frac{I_{(i+\lceil\theta N\rceil-1)} - I_i}{I_{(N)} - I_{(1)}}$ s.t. $\lceil\theta N\rceil \neq N$ for ordered data, $I_{(1)} \leq I_{(2)} \leq \dots \leq I_{(N)}$
Gaussian Entropy	$-\sum_{n_x=0}^{N_x-1} \sum_{n_y=0}^{N_y-1} \log(I^2(n_x, n_y))$
Shannon Entropy	$-\sum_{n_x=0}^{N_x-1} \sum_{n_y=0}^{N_y-1} \tilde{I}(n_x, n_y) \log(\tilde{I}^2(n_x, n_y))$ where $\tilde{I}(n_x, n_y) = \frac{I(n_x, n_y)}{\ \vec{I}(n_x, n_y)\ _2^2}$
MSE	$-\sum_{n_x=0}^{N_x-1} \sum_{n_y=0}^{N_y-1} I(n_x, n_y) \log(I^2(n_x, n_y))$
Hoyer	$\left(\sqrt{N} - \frac{\sum_{n_x=0}^{N_x-1} \sum_{n_y=0}^{N_y-1} I(n_x, n_y)}{\sqrt{\sum_{n_x=0}^{N_x-1} \sum_{n_y=0}^{N_y-1} I^2(n_x, n_y)}} \right) (\sqrt{N} - 1)^{-1}$ where $N = (N_x - 1)(N_y - 1)$
pq-mean	$-\left[\frac{1}{N} \sum_{n_x=0}^{N_x-1} \sum_{n_y=0}^{N_y-1} I^p(n_x, n_y) \right]^{\frac{1}{p}} \left[\frac{1}{N} \sum_{n_x=0}^{N_x-1} \sum_{n_y=0}^{N_y-1} I^q(n_x, n_y) \right]^{\frac{1}{q}}$ $p < q$
Gini index	$1 - 2 \sum_{k=1}^N \frac{I_{(k)}}{\ \vec{I}\ _1} \left(\frac{N-k+\frac{1}{2}}{N} \right)$ for ordered data, $I_{(1)} \leq I_{(2)} \leq \dots \leq I_{(N)}$

$$Gini(I) = 1 - 2 \sum_{k=1}^N \frac{I^{(k)}}{\|I\|_1} \left(\frac{N - k + 1/2}{N} \right) \quad (5.3)$$

The Gini index can be described as a weighted sum of the intensity values of the image that has a desirable property whereby the smaller valued pixels are given larger weight[153]. Using this metric, any changes in a pixel in the image, even in a smaller one, is reflected by a relatively strong variation in the weight of the value of the pixel in Eq. 5.3. Unlike the other metrics, another important advantage of the Gini index is that it is independent of the size of the input image, which makes it useful for comparing the sparsity value of images of different size. In addition to being normalized between the value of 0 and 1, the Gini index has a number of attributes that make it one of the most useful sparsity metrics[2].

The reconstructed intensity is the most common input used for metrics to detect the focal plane in DHM[83, 81, 87]. Another possible input is the reconstructed magnitude, equal to the square root of the reconstructed intensity, which has been previously used as the input in sparseness measurements[2] and autofocus algorithms in DHM[10]. Relative to the intensity, it reduces the dynamic range of the image data, resulting in smaller numbers playing a greater role. Therefore, it can be expected that the larger variation within the smaller range of values will have a greater influence on the sparsity metrics than for the case of the intensity. It must be noted that in some cases, for example, the ℓ_p norm and pq -mean, the choice of parameters will influence whether the absolute value or the intensity is actually used, regardless of whether they are applied as input to the metric, e.g. $p = 2$ or $p = 1/2$. The phase of a reconstructed digital hologram was also considered as an input, but all of the sparsity metrics return insignificant results. In this chapter, in addition to the reconstructed intensity and absolute value, we consider another input to the various metrics listed in Tab. 5.2, effectively doubling the number of sparsity metrics that are investigated as shown in Tab. 5.2.

Table 5.2 Two inputs for the metrics that are listed in Tab. 5.1.

Name	Definition
Intensity	$I(n_x, n_y) = o(n_x \delta_x, n_y \delta_y) ^2$
Magnitude	$I(n_x, n_y) = o(n_x \delta_x, n_y \delta_y) $

5.3 Results

In this section we present the results of sparsity based autofocusing on digital holograms of a number of diatom cells recorded using two different MOs. The

optical system described in Section 2.6 is used to record all holograms, and all numerical reconstruction are implemented using the spectral method also described earlier. Specifically, we present results of two diatom cells using a $20\times$ MO with $NA = 0.5$ and an oil immersion $63\times$ MO with $NA = 1.3$.

In all cases, the distance values that are given below are related to the image plane; these values are equal to the value of the distance parameter input to the spectral method divided by M^2 where M is the magnification, as discussed in Section 2.6.4 and elsewhere.[154]

5.3.1 Application of sparsity metrics to DHM of a diatom cell with $20\times$ magnification

In this section, we present the results of applying the metrics discussed in Section 5.2 to a sequence of reconstructed images of the digital hologram of a diatom cell recorded with a $20\times/0.5NA$ MO. The hologram was reconstructed at a sequence of distances from the CCD plane, with a range of values of $d = -75\mu\text{m} \rightarrow 75\mu\text{m}$ and with a step size of $\delta_d = 0.25\mu\text{m}$. In Fig. 5.1 (a)-(f) the intensity and phase images of the reconstruction are shown before, at, and after the correct focal plane, with the distance $d = -12.5\mu\text{m}$, $-6.75\mu\text{m}$ and $0\mu\text{m}$ respectively. The intensity images shown in Fig. 5.1 (a) and (c) appear blurred and diffraction effects are visible, indicating that they are both out-of-focus; on the other hand, Fig. 5.1 (b) contains more detailed information about the internal structure of the cell, which suggests that this plane is close to the correct image plane. Video 5.2 shows both the intensity and phase of the reconstructed image for a progression of increasing propagation distance values; the distance propagation is shown in the top left in the video.

The intensity of each reconstruction is evaluated by the 32 sparsity metrics discussed in Section 5.2, and the values of these metrics as a function of reconstruction distances are compared. In the case of the pure phase objects, such as unstained biological cells, previous studies have shown that the correct in-focus image produces the minimum value of traditional autofocus metrics; this plane contains the minimum image contrast and diffraction effects are observed at planes that are not in focus, resulting in higher contrast and lower sparsity values. The results are shown in Fig. 5.3, only for $I = |o|^2$, where it can be seen that most of the metrics provide reasonable performance for identifying the correct image plane with the exception of the ℓ_0 metric. The ℓ_0 metric fails because the reconstructed intensity contains no zero value pixels at any distance.

In Fig. 5.3 the raw results are shown in blue and it is clear that the metrics: $-\ell^p$ _norms, ℓ_ϵ^0 , $\frac{\ell_2}{\ell_1}$, $-\tanh_{a,b}$, $-\log$, Kurtosis, Modified Shannon Entropy, Hoyer and Gini index, all provide reliable performance in that they all have a global minimum and a local minimum at what we qualitatively perceive to be the correct image plane at $d = -6.75\mu\text{m}$. Although Shannon Entropy and pq -mean metrics fail to produce

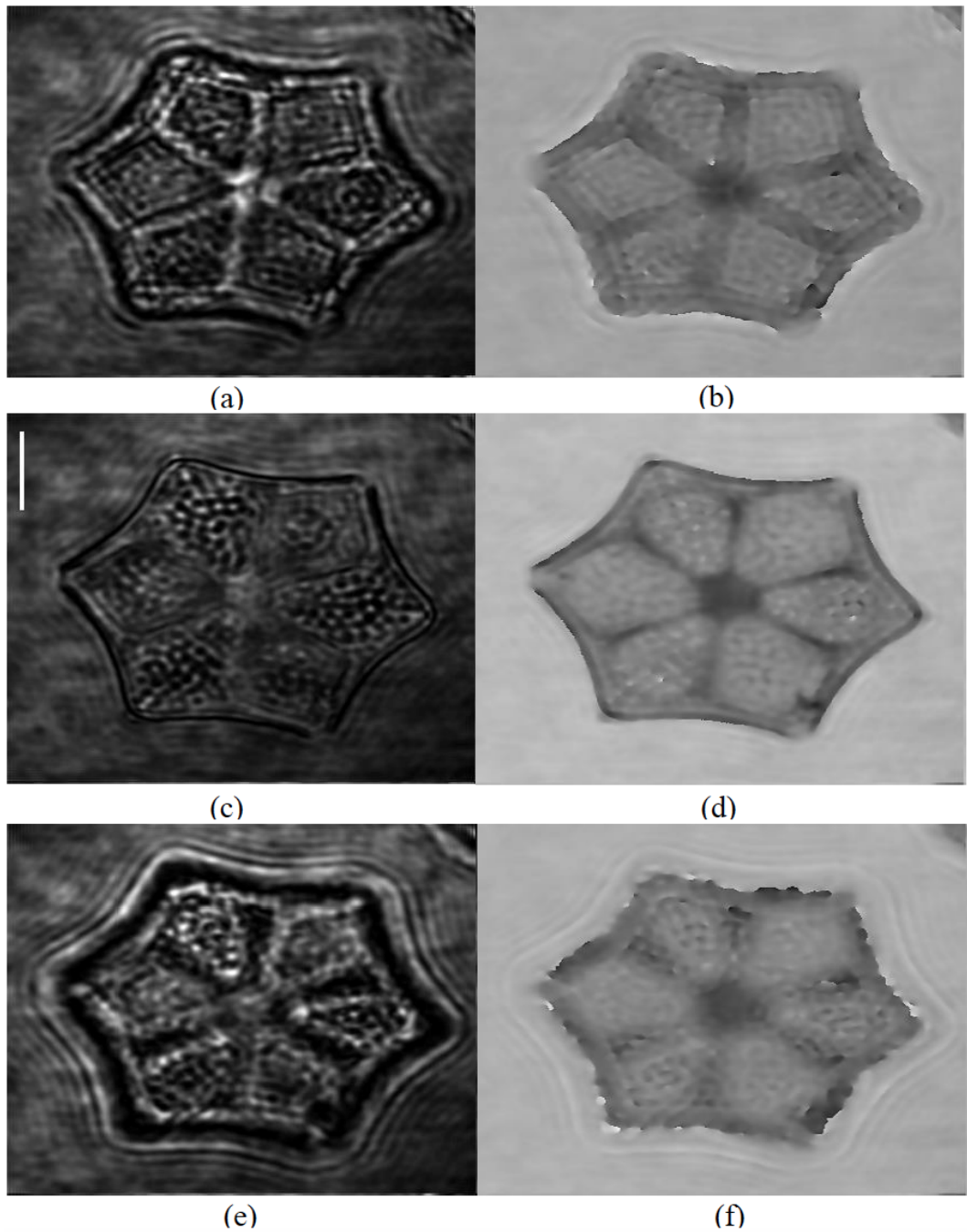


Fig. 5.1 Hologram 1($20\times/0.5$): the reconstructed intensity and unwrapped phase of Hologram 1 on the plane before, at, and after, the focus plane; the distances are $-12.5\mu\text{m}$, $-6.75\mu\text{m}$, and $0\mu\text{m}$ respectively. A scale bar is shown that is equal to $10\mu\text{m}$.

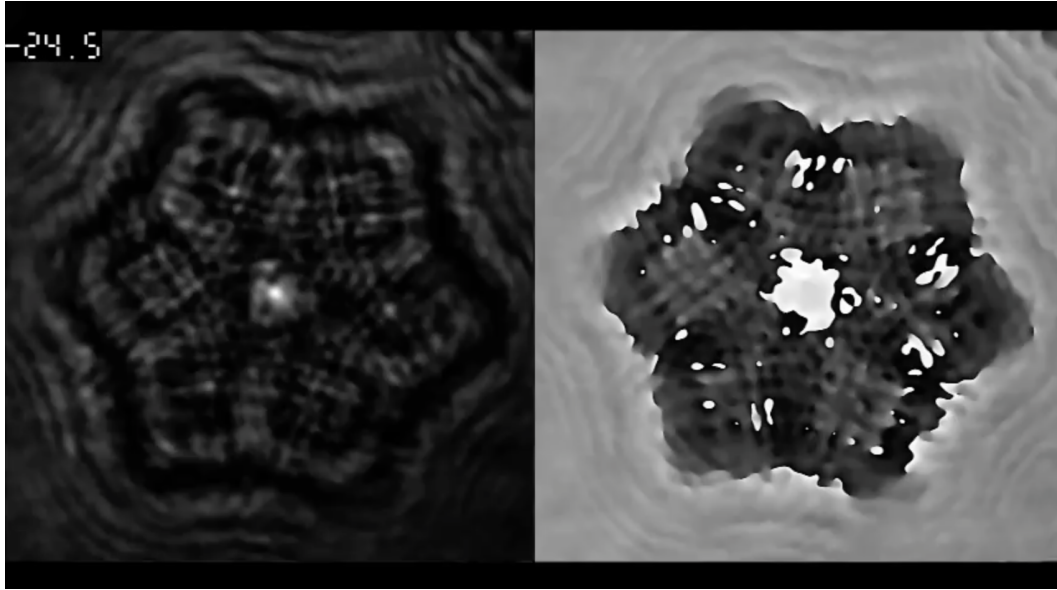


Fig. 5.2 Hologram 1 ($20 \times /0.5$): the intensity and phase reconstructed images of the diatom cell hologram over a range of propagation distances; the propagation distance is shown in the top left with units of μm .

a global minimum, these metrics succeed in producing a clearly identifiable local minimum in the proximity of the correct distance. It is notable that although the metric u_{Θ} produces several local minima that could potentially result in an incorrect convergence for an arbitrary search range, it produces a global minimum at the correct distance over the full range chosen here.

In an effort to produce more reliable and reproducible results, we perform a type of high-pass filtering of each metric as a function of propagation distance by employing the well-known Savitzky-Golay filter. The Savitzky-Golay filter is a least squares polynomial filter proposed by Savitzky and Golay in 1964[155], which is among the most popular digital smoothing filters in signal processing. It is a finite impulse response filter that is essentially a low-pass filter that is well adapted for data smoothing. Least squares fitting of an n order polynomial is applied across different regions of pixels in order to obtain a smoothed low frequency estimate of the signal. The polynomial degree and the filter length can be adapted to suit a given application. In this work, we choose a polynomial degree of 3 and a polynomial length of 143; these values were found to provide good estimates of the broad signal variation for the majority of cases. Following subtraction of this smoothed signal, thereby revealing the high frequency content, all metrics except for the ℓ_0 norm and the ℓ_1 norm provide more reliable and reproducible performance, and interestingly exhibit matching behavior, which is the subject of the following subsection. These results are also shown in Fig. 5.3 in black. Following high pass filtering, the locations of the global minima are presented in Tab. 5.3.

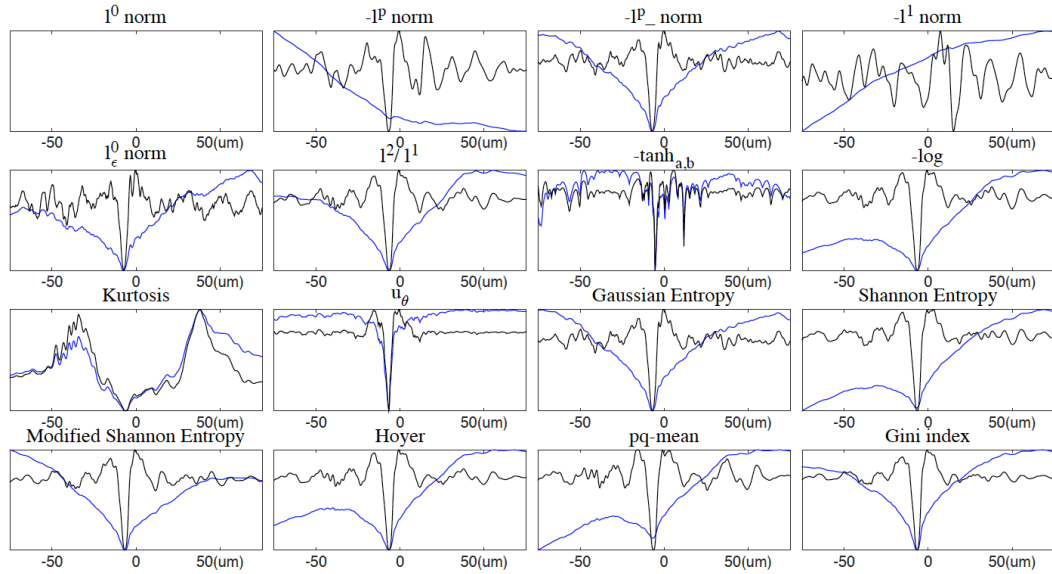


Fig. 5.3 Hologram 1($20 \times /0.5$): results of 16 sparsity metrics in Table 5.1 applied to the reconstructed intensity images of the Diatom cell before and after subtraction of the smoothed signal. The blue lines are the raw autofocusing curves and the black lines are the autofocusing curves after subtraction of the smoothed signal.

5.3.2 Grouping

Following the removal of smooth features, the behaviors of several of the sparsity metrics show a clear resemblance. For example, metrics $\frac{\ell_2}{\ell_1}$, $-\log$, Shannon Entropy, Modified Shannon Entropy, Hoyer, pq -mean, Gini index, $-\ell^p$ norm, Gaussian Entropy and ℓ_ϵ^0 , share similar characteristics. Based on these results (which, thus far correspond only to the first input $I = |o|^2$), we propose classifying the 15 sparsity metrics (excluding the ℓ_0 metric), into three different groups respectively, which reflects the common features that are present in the performance of these metrics as a function of propagation distance; this grouping is illustrated in Fig. 5.4. It should be noted that the behaviors of the first six metrics show a significant resemblance, even for the small features that are visible across the total range, and the position of the global minimum is found to closely match. The last three metrics in Group A bear a close similarity to each other, while differing slightly with the first six metrics, whereby the location of the minimum value is observed to shift slightly. Overall the ten metrics in Group A are approximately conformable, although a mismatch exists in some small features, particularly with respect to the first six and latter three metrics. Similarly for Group B, $-\tanh_{a,b}$ and u_θ have similar characteristics, which is confirmed following testing on a large number of different holograms that are not presented here. Following this classification, there are three metrics that remain, all of which exhibit erratic performance, and therefore, we group these misfit metrics together as Group C. All metrics in this group, except for the ℓ_1 norm (and the previously dropped ℓ_0), successfully contain both a local and global minimum in

Table 5.3 The focus positions detected by the metrics that are listed in Tab. 5.1 and Tab. 5.2. Here, * denotes to the estimated focus position for each hologram based on the mean value of the results.

	Metrics	Hologram1(20×) (−6.75μm*)		Hologram2(20×) (−6.50μm*)		Hologram3(63×) (−0.81μm*)	
		$ o ^2$	$ o $	$ o ^2$	$ o $	$ o ^2$	$ o $
(1)	ℓ^0	-	-	-	-	-	-
(2)	$-\ell^p$	−6.75	−7.00	−6.50	−6.75	−0.40	−0.38
(3)	$-\ell^p_-$	−7.00	−7.00	−7.25	−7.25	−0.35	−0.35
(4)	$-\ell^1$	15.00	−7.00	−7.50	−6.75	−5.87	−0.38
(5)	ℓ_ε^0	−7.50	−7.75	−8.00	−10.00	−0.60	−0.45
(6)	$\frac{\ell_2}{\ell_1}$	−6.75	−7.00	−6.50	−6.75	−0.81	−0.38
(7)	$-\tanh_{a,b}$	−5.50	−5.50	−6.25	−6.25	5.59	3.25
(8)	−log	−6.50	−6.75	−6.50	−6.50	−0.38	−0.81
(9)	Kurtosis	−5.75	−6.75	−6.50	−6.50	−0.86	−0.81
(10)	u_Θ	−6.75	−6.75	−6.25	−6.25	−0.43	−0.43
(11)	Gaussian Entropy	−7.00	−7.00	−7.00	−7.00	−0.35	−0.35
(12)	Shannon Entropy	−6.75	−6.75	−6.50	−6.50	−0.38	−0.40
(13)	MSE	−6.75	−7.00	−6.50	−7.25	−0.40	−0.35
(14)	Hoyer	−6.75	15.00	−6.50	−69.00	−0.81	5.97
(15)	pq-mean	−6.50	−7.00	−6.25	−7.00	−0.81	−0.38
(16)	Gini index	−6.75	−6.75	−6.50	−6.75	−0.38	−0.38

the correct focal plane. A second diatom cell was recorded using the same MO and the same investigation was applied to test the performance of the various sparsity metrics for autofocusing, once again $I = |o|^2$. The results are shown in Tab. 5.3 under ‘Hologram 2’ and in Fig. 5.6; similar grouping was observed and it is evident that Group A produces a strong global minimum at approximately the correct image plane. Interestingly, the slight disagreement between the first six metrics and the latter three metrics appears again, whereby the global minimum is observed to shift slightly; however, this can be ignored because it has little influence on the reconstructed image. Similar results to those shown in Fig. 5.4 were also found for Group B but these results are not shown here. Video 5.5 shows the intensity and phase of the reconstructed images of this diatom cell over the full range of distances that are investigated, as for the previous cell. In this case, we used a same range of d , step size and the Savitzky-Golay filter proceeds as mentioned before. Once again the reconstruction distance is shown in the top left in the video.

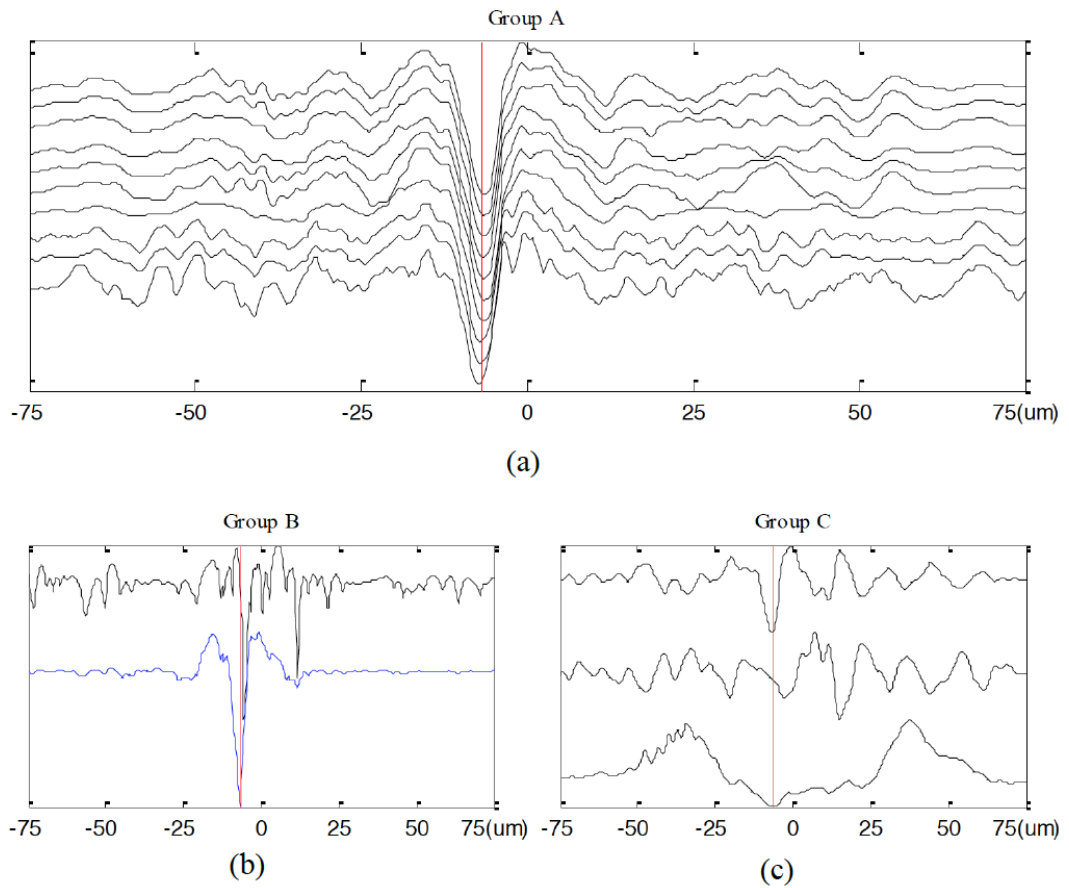


Fig. 5.4 Results for Hologram 1($20 \times /0.5$) using $I = |o|^2$. Grouping of the 15 sparsity metrics in Fig. 5.3 is possible after high pass filtering. (a) Group A produces the most similar results; from top to bottom: $\frac{\ell_2}{\ell_1}$, $-\log$, Shannon Entropy, Modified Shannon Entropy, Hoyer, pq -mean, Gini index, $-\ell^p$ norm, Gaussian Entropy and ℓ_ϵ^0 ; (b) Group B contains $-\tanh_{a,b}$ and u_Θ ; (c) Group C contains those metrics that are not similar to any other metrics; from top to bottom, they are $-\ell^p$ norm, $-\ell^1$ and Kurtosis.

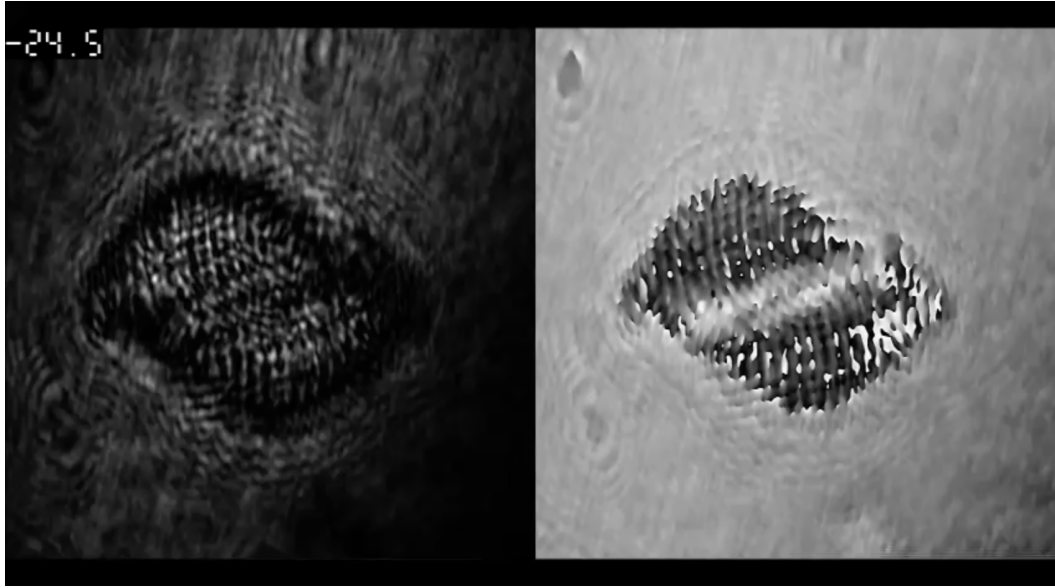


Fig. 5.5 Hologram 1 ($20\times/0.5$): the intensity and phase reconstructed images of a second diatom cell hologram over a range of propagation distances; the propagation distance is shown in the top left with units of μm .

5.3.3 Application of sparsity metrics to DHM of a diatom cell with $63\times$ magnification

The first of the two diatom cells investigated in Section 5.2 was recorded again, this time using a $63\times$ oil immersion MO with a significantly higher numerical aperture of 1.3. It is well known that the depth of field is considerably narrower for higher numerical apertures, and therefore, narrower features are expected in the behavior of the autofocus metrics as a function of distance. Video 5.7 shows the intensity and phase reconstructed images over a range of different distances. In this case the range of distances is given by $d = -7.5\mu\text{m} \rightarrow 7.5\mu\text{m}$ and a step size of $\delta_d = 0.025\mu\text{m}$ is used. The locations of the global minimum (following high pass filtering) are given in Tab. 5.3. Once again similar behavior is found for Group A and Group B; where only the former is shown in Fig. 5.8. Notably, two strong local minima are observed to be adjacent to each other, in the location of the image plane indicating that the diatom cell has two different focal depths of interest; the global minimum varies slightly across Group A: $\frac{\ell_2}{\ell_1}$, Hoyer and pq -mean metrics indicate that the left minimum corresponds to the image plane, while $-\log$, Shannon Entropy, Modified Shannon Entropy and Gini index metrics identify the right minimum as corresponding to the correct image plane. The $-\ell^p$ norm and Gaussian Entropy both indicate that there is only one focal plane, which is the right of the two minima that are marked on the figure, and finally the ℓ_ϵ^0 metric identifies both minima as focal planes. An investigation of the reconstruction at both of these distances reveals that the object contains features primarily at both of these distances; the object is

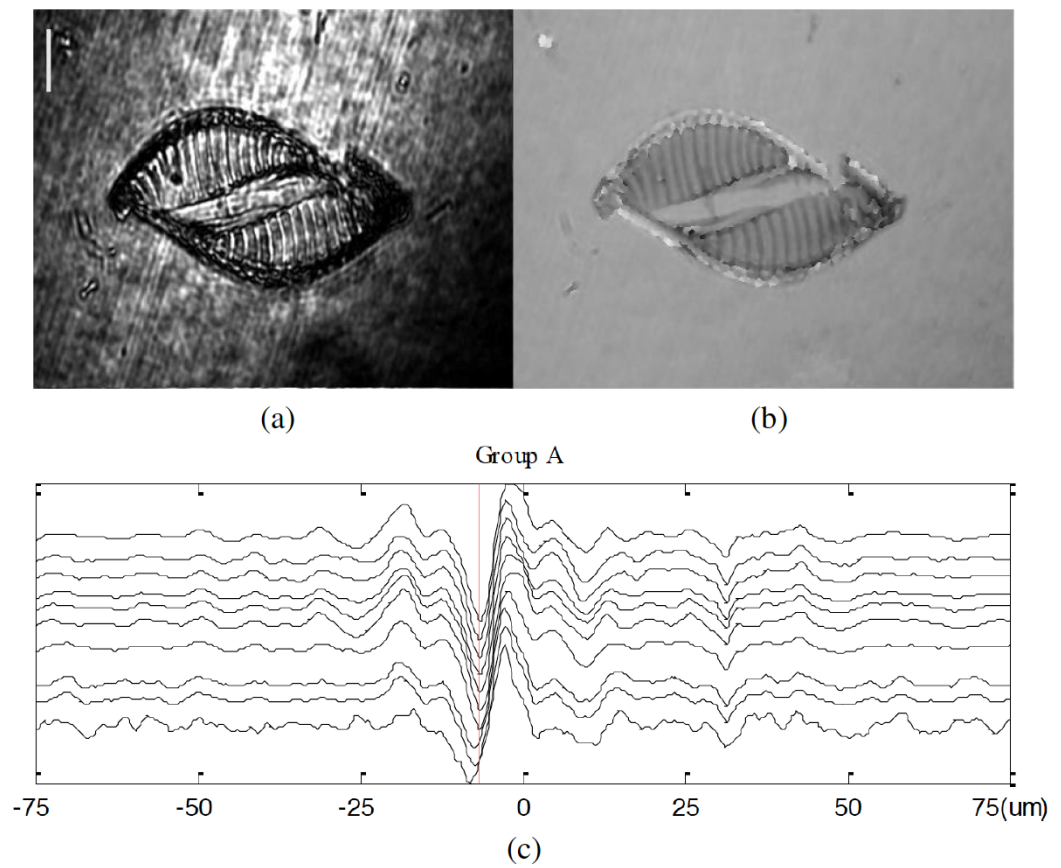


Fig. 5.6 Hologram 2 ($20\times/0.5$): (a) and (b) are the reconstructed intensity and unwrapped phase of a second Diatom cell. The scale bar represents $10\mu\text{m}$. (c) The result for Group A are shown for this hologram.

hexagonal as shape, and interestingly every second region is in focus at alternate values of distance.

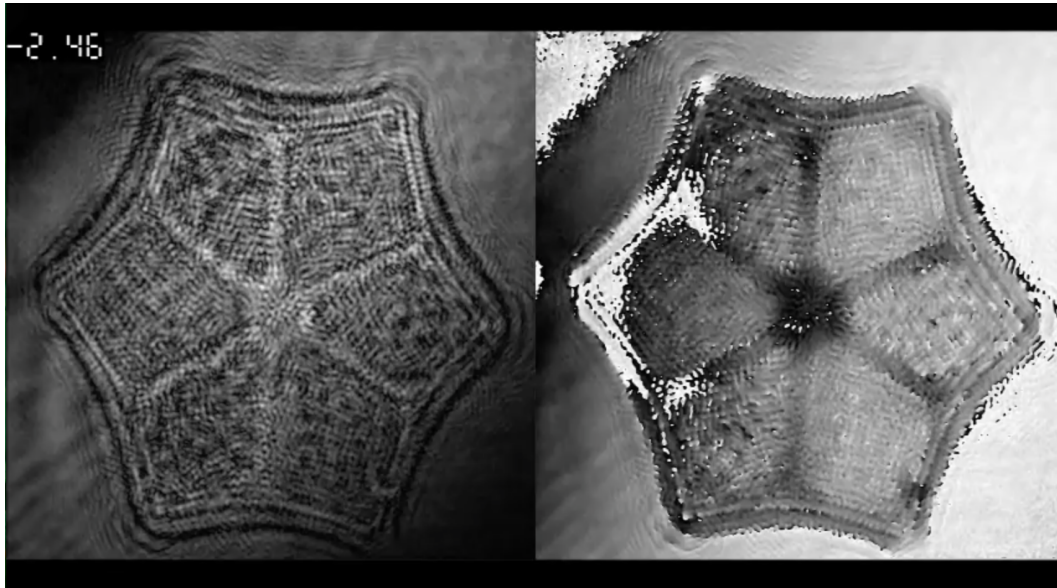


Fig. 5.7 Hologram 3 ($63 \times /1.3$): the intensity and phase reconstructed images of the diatom cell hologram over a range of propagation distances; the propagation distance is shown in the top left with units of μm .

Before proceeding to the next section, we mention that the procedure discussed above was repeated for all three holograms with $I = |o|$; in each case, similar results were found as shown in Tab. 5.3, and once again, it was possible to classify the matching behavior of many of the metrics; this extended grouping is discussed in more detail in Section 5.4.

5.4 Discussion

In Section 5.3, results were presented from digital holograms of two diatom cells using two different MOs. For the purpose of clarity, the performance of the 16 sparsity metrics listed in Tab. 5.1 were evaluated only for the input $I = |o|^2$, and on this basis we proposed classifying the 16 metrics based on matching behavior of each metric as a function of propagation distance; this was possible only after high pass filtering. The results of the 16 metrics for $I = |o|$ are provided in Tab. 5.3; however, no further discussion was given. In this section we extend the discussion to include these results in terms of classification. Furthermore, the discussion that follows on the subject of grouping the metrics according to matching behavior, is based on testing all 32 sparsity metrics on a range of different holograms of 10 different diatom cells in addition to the holograms shown in the chapter, all using the two different MOs. In addition, we quantitatively compare these results to a number

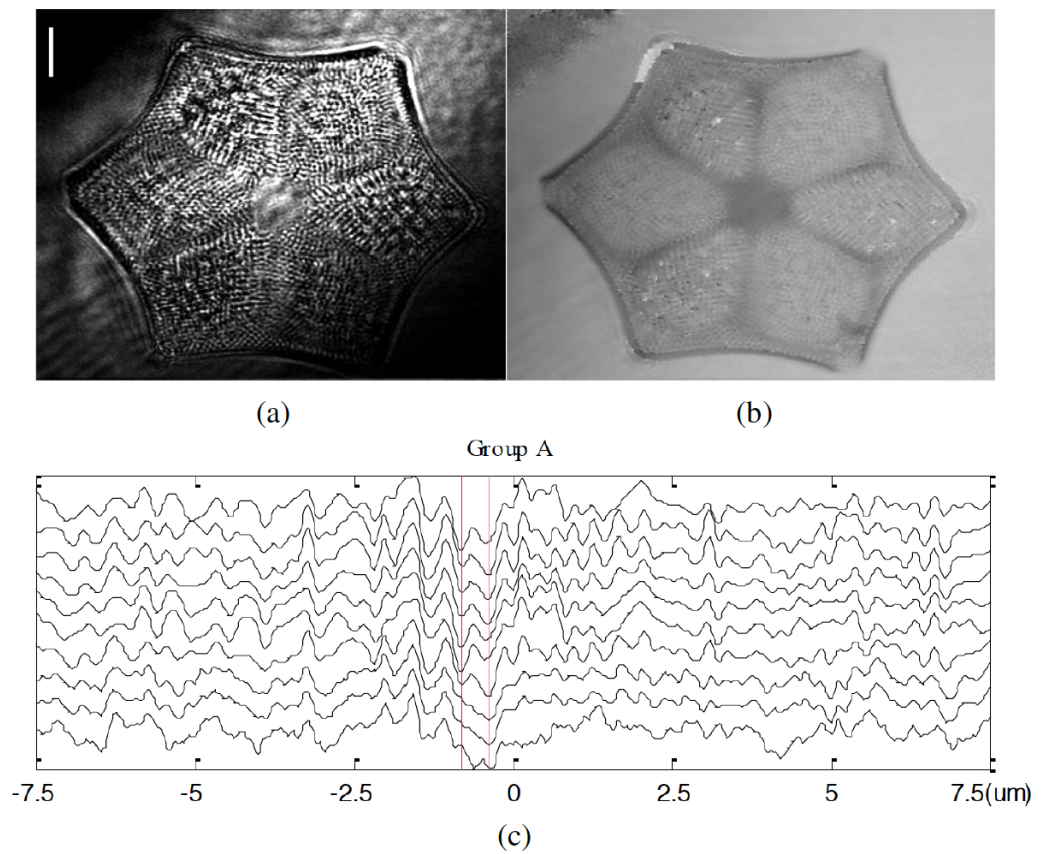


Fig. 5.8 Hologram 3 ($63 \times / 1.3$): (a) and (b) are the reconstructed intensity and unwrapped phase of a diatom cell hologram. The scale bar represents $5 \mu\text{m}$. (c) The results for Group A are shown, indicating two global minima as discussed in the text.

of well known autofocus metrics in DHM and we interpret the performance in terms of the depth of field of the microscope.

5.4.1 Classification of sparsity metrics for autofocusing

Based on the results of all of the holograms tested in this study, including results from more than 10 diatom cells, recorded using both the $20\times$ and $63\times$ MOs, we apply grouping for all 32 sparsity metrics, which are made up of the 16 original sparsity metrics with the two inputs that are presented in Tab. 5.2. Most of the metrics succeed in detecting the image plane. The groupings are presented in Tab. 5.4.

Table 5.4 The grouping for the 32 sparsity metrics based on 10 different diatom cells recorded using the $20\times$ and $63\times$ MOs. * denotes a slight difference shown in this metric compared to others in the same group; - denotes these metrics that failed to return the focus curve and X denotes the metrics that return a global minimum at an incorrect location.

Number	Name	$ o ^2$	$ o $
(1)	ℓ^0	-	-
(2)	$-\ell^p$	C	A
(3)	$-\ell^p_-$	A	A*
(4)	$-\ell^1$	X	A*
(5)	ℓ_ϵ^0	A	C
(6)	$\frac{\ell_2}{\ell_1}$	A	A
(7)	$-\tanh_{a,b}$	B	B
(8)	$-\log$	A	C
(9)	Kurtosis	C	C
(10)	u_Θ	B	B
(11)	Gaussian Entropy	A	A*
(12)	Shannon Entropy	A	A
(13)	Modified Shannon Entropy	A	A
(14)	Hoyer	A	X
(15)	pq-mean	A	A
(16)	Gini index	A	A

In general, the behavior of a given sparsity metric in Tab. 5.4 is consistent for each of the two inputs listed in Tab. 5.2. The symbol ‘-’ denotes these metrics that failed to return any information whatsoever and ‘X’ denotes those metrics that return data that fails to detect the correct focal plane with the global minimum. Most of metrics provide reliable performance. The ℓ_0 metric fails to return any meaningful information, since the reconstructed intensity and magnitude are composed of non-zero values in general; however, many of elements are small numbers that are

close to zero and therefore, the ℓ_ε^0 metric is preferable and is shown to provide good performance using both the reconstructed intensity and the absolute value. Noticeably, the $-\ell^1$ metric succeeds in detecting the image plane for $I = |o|$ but fails to do so for $I = |o|^2$, for which the returned global minimum is not located in the correct focal plane. Interestingly, the $-\ell^p$ metric with the input $|o|^2$ has a behavior that differs from that $I = |o|$, which can be classified into Group A, but it exhibits similar behavior to the $-\log$ metric and is therefore classified in Group C. Conversely, for the case of the Hoyer metric using the reconstructed magnitude fails to produce a reliable result while the input $I = |o|^2$ closely matches the behavior of Group A. This is due to the reconstructed magnitude lowering the range between the maximum and the minimum values. The $-\tanh_{a,b}$ and u_Θ metric were found to have similar behavior regardless of the two inputs, and these metrics make up Group B.

In general, we conclude that Group A contains the most reliable metrics, most often returning the correct distance; the following five in Group A, ($\frac{\ell_2}{\ell_1}$, Shannon Entropy, Modified Shannon Entropy, pq -mean and Gini index) were determined to provide the most reliable and reproducible results for both inputs $I = |o|^2$ and $I = |o|$. Group B also provides reliable results. Although some variation is observed on a case by case basis, in general, these groups show similar behavior.

5.4.2 Quantitative evaluations in terms of depth of field

In this subsection the performance of the 16 sparsity metrics, for both $I = |o|^2$ and $I = |o|$ are evaluated in terms of the mean value, the median, the standard deviation, and the depth of field of the microscope.

The depth of field (DoF) in the object plane refers to the thickness of the optical section along the z -axis within which, objects in the specimen are collectively in-focus[154]; for a diffraction limited microscope the definition of depth of field is given as $DoF = n\lambda/NA^2$, [154] where n is the refractive index of the medium between the lens and the object. Thus, the larger the aperture angle (the higher the NA), the narrower the depth of field[46]. This definition is based on wave-optics and can be extended to include features of geometrical optics; however, for the optical system described in Section 2.6, the wave optical definition is sufficiently accurate.

In Fig. 5.9 the distribution of the global minima of all 32 sparsity metrics are illustrated for each of the three holograms discussed in this chapter. Those metrics that failed to detect the approximate image plane are omitted (see Tab. 5.4). The mean values are illustrated with red lines, around which the box plot illustrates double the standard deviation of the results. The median values are also shown in green. The DoF is shown alongside the distribution of values and is centered on the mean value. The following results are obtained for the standard deviation of the sparsity metrics and the DoF for each hologram respectively: Hologram 1 ($20\times$) $0.63\mu\text{m}$ and $2.6\mu\text{m}$, Hologram 2 ($20\times$) $0.58\mu\text{m}$ and $2.6\mu\text{m}$ and Hologram 3 ($63\times$)

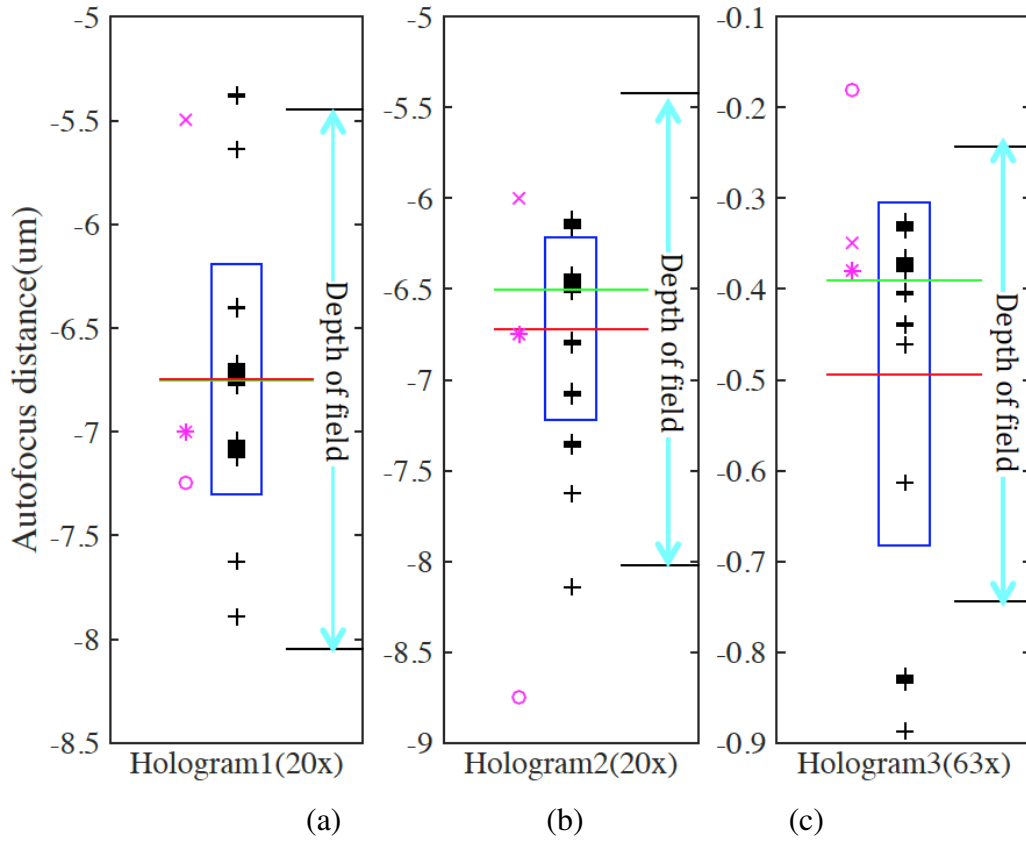


Fig. 5.9 + donates to the focal position detected by 32 sparsity metrics, listed in Tab. 5.3; the positions of the red line, the green line, the blue box are the mean value, median value, and the standard deviation of the focus distances detected by 32 sparsity metrics respectively; the cyan line represents the depth of field of each hologram; the magenta spots represent the focal positions detected by three commonly used autofocusing metrics: the asterisk, cross, and circle, denote the variance of the intensity, cumulated edge detection by gradient calculation, and weighted spectral analysis respectively.

$0.20\mu\text{m}$ and $0.50\mu\text{m}$. The standard deviation of the autofocus value are significantly smaller than the DoF of the microscope for all three holograms, and all of the values returned by Group A are comfortably within the DoF.

5.4.3 Comparisons with the commonly used autofocusing metrics

Three commonly used autofocusing metrics, the variance of the intensity, cumulated edge detection by gradient calculation, and weighted spectral analysis[10], are applied to the three holograms in order to compare the performance of our sparsity metrics. The distance range and step size is the same as for the previously described experiments. Figure 5.10 shows the results of these three focus metrics as a function of propagation distance for the three holograms. The raw results, shown in blue, are broadly in agreement with the focus position detected by our 32 sparsity metrics. Of

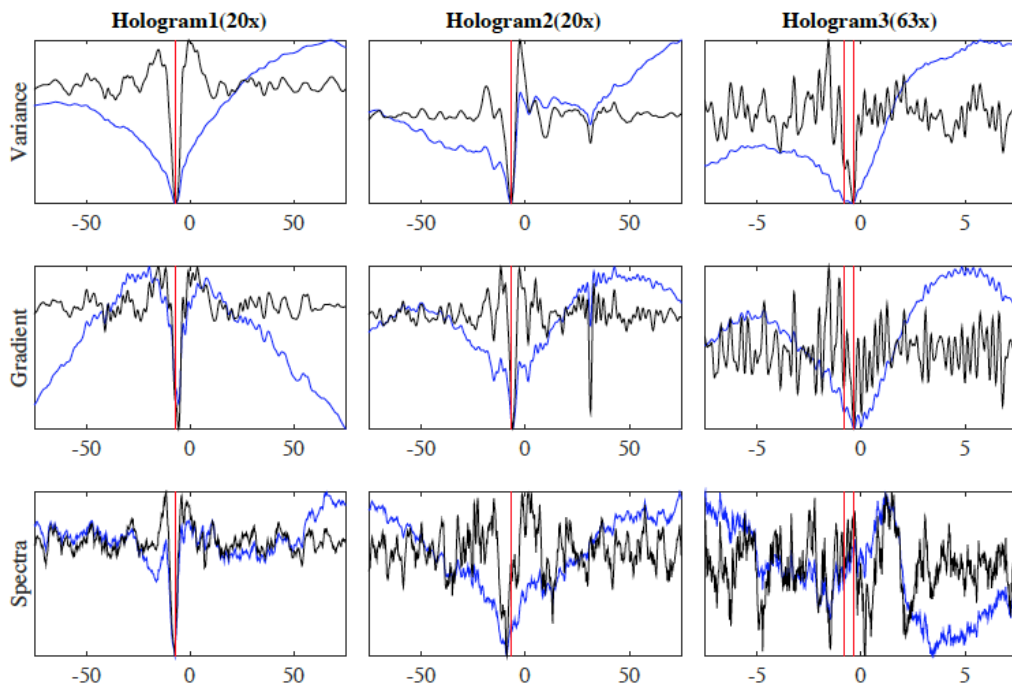


Fig. 5.10 Results of 3 commonly used metrics applied to the reconstructed intensity images of the three holograms investigated in this chapter before and after subtraction of the smoothed signal. The blue lines are the raw results, and the black lines are the same results after subtraction of the smoothed signal.

the three metrics, the variance is found to be the most consistent and provides the most similar results to Group A.

Interestingly, when these three metrics, as a function of propagation distance, are high pass filtered in the same way as described in Section 5.3, a similar behavior can be observed as for the sparsity metrics; these results are shown by the black lines in Fig. 5.10. Most noticeably the variance is now found clearly to resemble Group A. The gradient also has similarities to Group A, although appearing to be more symmetrical about the global minimum. The weighted spectral analysis metric also exhibits similar behavior but fails to identify the image plane for the $63\times$ magnification hologram.

5.5 Conclusion

In this chapter, 32 sparsity metrics are investigated for application to autofocusing in DHM. These metrics, the majority of which have not previously been investigated in image processing to the best of our knowledge, are applied to a range of holograms, recorded from a number of different diatom cells and using different microscope objectives, in terms of magnification and numerical aperture.

An important result is the discovery that the 32 sparsity metrics investigated here can be grouped according to similar behavior following high pass filtering. After

evaluating and comparing the performance of the metrics, it is notable that six of metrics provide unambiguous, reliable, and repeatable minima for different diatom cells with different MOs over a large search range and both provide similar results for $I = |o|^2$ and $I = |o|$. This conclusion is based on evaluating the metrics across a broad range of holograms of diatom cells, as well as comparing them to commonly used metrics and interpreting their performance in terms of the depth of field of the microscope.

We believe that the methodology proposed here for the evaluation and grouping of different focus metrics according to similar behavior as a function of propagation distance, following high pass filtering, may be applicable to all autofocus metrics and should be the subject of future research. This approach may offer a common framework for understanding and comparing the many autofocus metrics that have been proposed to date in the literature in a meaningful way, both for DHM as well as for other forms of microscopy.

Another important conclusion from this work is that following high pass filtering as described in Section 5.2, the variance of the intensity, perhaps the most commonly used autofocus metric in the literature, produces almost identical results to the best performing sparsity metrics that were investigated here, in terms of accuracy and reliable. Taking into account the simplicity of the variance metric in terms of computation, we conclude that this may be the metric of choice for DHM.

At this point, an in-focus hologram of an unstained biological sample containing both amplitude and phase information is achieved by recording by the off-axis DHM interferometer proposed in the previous two chapters, followed by the numerical reconstruction algorithm and a reliable and reproducible autofocusing metric as discussed in this chapter. In the following chapters, the in-focus reconstructed quantitative phase image is input to two novel image processing algorithms for the purpose of label-free color staining of subcellular features.

Chapter 6

Label-free color staining of quantitative phase images of biological cells by simulated Rheinberg illumination

This chapter relates to the following paper:

- Xin Fan, John J. Healy, and Bryan M. Hennelly. *Label-free color staining of quantitative phase images of biological cells by simulated Rheinberg illumination*. Submitted to *Advanced Photonics* Sept 2018.

6.1 Introduction

The goal of this thesis is to explore the cellular morphology of quantitative phase images of unstained biological samples, which are essentially invisible in ordinary bright-field microscopy, by digital holographic microscopy. In the previous chapters, we proposed two new optical systems for recording in digital holographic microscopy as well as a comprehensive examination of methods to achieve autofocusing of the recorded holograms. In this chapter, we propose the first of two label-free color coding algorithm that can be applied to the in-focus reconstructed quantitative phase image. The first algorithm, presented in this chapter is based on simulating the optical microscopy method, Rheinberg illumination, which has previously been demonstrated to have application in the visualization of sub cellular features in biological samples.

As described in Section 2.5, modern microscopes are designed with functionalities that are tailored to enhance image contrast. Dark-field imaging, phase contrast, differential interference contrast, and other optical techniques enable biological cells and other phase-only objects to be visualised. Quantitative phase imaging refers to an emerging set of techniques that allow for the complex transmission function of the

sample to be measured. A brief review of these methods is provided in Section 2.5, Section 2.8 and Section 2.9. With this quantitative phase image available, any optical technique can then be simulated; it is trivial to generate a phase contrast image or a DIC image. Rheinberg illumination, proposed almost a century ago, is an optical technique that applies color contrast to images of phase only objects by introducing a type of optical staining via an amplitude filter placed in the illumination path that consists of two or more colors.

The breakdown of this chapter is as follows. In Section 6.2 the theory of optical Rheinberg illumination is derived from which, a numerical algorithm is proposed in Section 6.3 that can color stain sub cellular features in complex transmittance images recorded using QPI techniques. In Section 6.4 the results are shown of applying the algorithm to a number of images of diatom cells recorded using DHM and finally in Section 6.5 a brief discussion is offered.

6.2 Theory of optical Rheinberg illumination

In this section, a theoretical framework for understanding optical staining by Rheinberg illumination is proposed. Despite the longevity of Rheinberg illumination, a search of the literature did not provide any theoretical analysis of the detail provided here. We believe that this work may represent the first detailed theoretical analysis of this type of imaging. In the next section, an algorithm is developed that is based on this analysis. In Fig. 6.1 (a) the optical set-up for Rheinberg illumination is illustrated. This set-up is based on the traditional architecture of a brightfield optical microscope employing Kohler illumination¹, [156]. In this configuration, a multimodal filter containing at least two color filters (most commonly in the form of a circle of one colour filter around which is a ring containing a second color filter) is placed in the focal plane of the condenser lens. The source illumination and the lens preceding the filter are not shown in the image.

Image formation in microscopy can be described using Fourier theory [1, 156–158]; a brief review can be found in Section 2.3.3. For the case of spatially coherent illumination, the image is given by the convolution of the input complex transmittance, $t(x)$, and the coherent point spread function of the optical system $h(x)$, where x denotes the two dimensional spatial coordinate system. This convolution can be described as a multiplication in the spatial frequency domain; i.e. the Fourier transform of the image is given by the Fourier transform of $t(x)$, which is denoted as $F(k)$, and the pupil function of the microscope, $P(k)$, where k denotes the 2D coordinates of the spatial frequency domain. In this case, the imaging system is linear in complex amplitude. For the case of incoherent illumination, the image formed by the microscope is given by the convolution of the intensity $|t(x)|^2$ and the incoherent point spread function of the optical system $|h(x)|^2$. Once again this

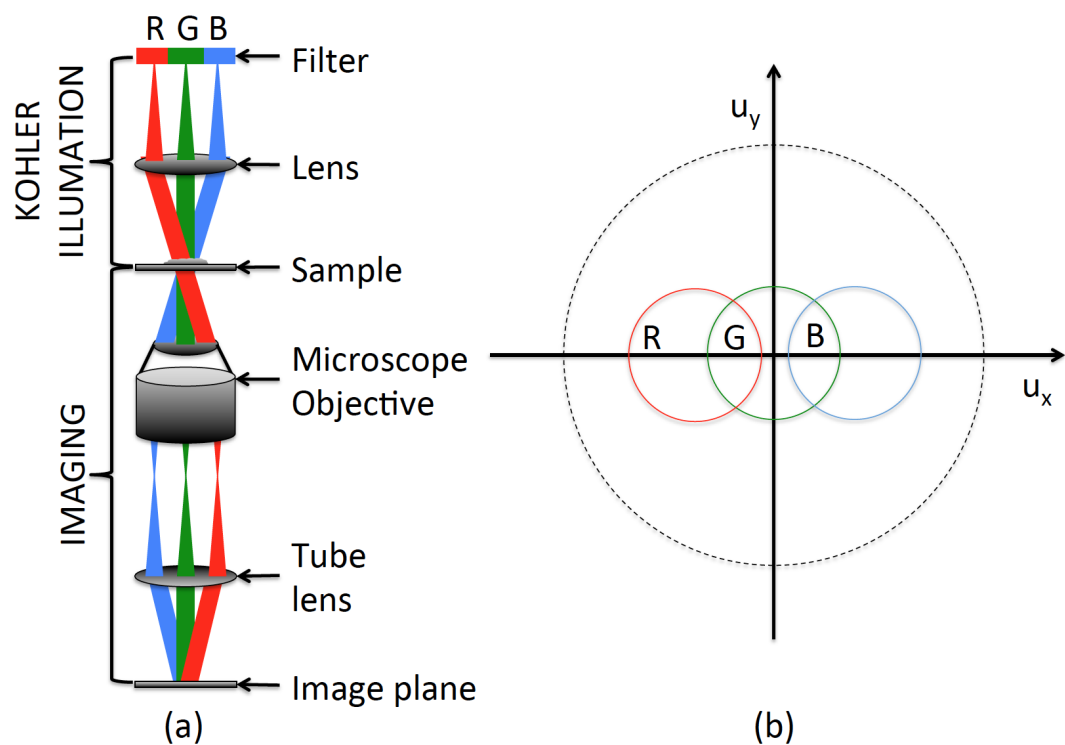


Fig. 6.1 (a) Illustration of optical Rheinberg illumination. Three color filters are placed at the back focal plane of the condenser lens. (b) Each of the three point sources illustrated in Fig. 6.1 (a) independently contribute to image formation. In each of these three cases image formation results from bilinear contributions from within the supports shown in the spatial frequency domain. The radius of the circular supports shown in the figure is related to the pupil function of the microscope[1]. The dashed line represents the fundamental limit of resolution.

can be described in terms of the Fourier transforms of these two functions; this time, however, image formation is linear in intensity.

For the case of a partially coherent imaging, such as that provided by Kohler illumination, image formation becomes more complex, and is no longer linear in either complex transmittance or intensity. For such a system, it can be assumed that the object is illuminated by an ‘incoherent’ delta correlated light source propagating from the condenser pupil[130]. In the following derivation, it is assumed that the illumination is quasi-monochromatic; more specifically, it is assumed that for each of the different color filters in the illumination set-up, the light that is transmitted is quasi-monochromatic around that filter’s line (band) pass wavelength. An extension of this analysis to polychromatic illumination is trivial. Unit magnification is assumed throughout the analysis. Initially, only a single filter is considered; the illumination emerging from the filter plane has an intensity distribution $S(k)$. The image at the output of the microscope is given by:

$$I(x) = \int S(k) \left| \int t(x')h(x-x')e^{j2\pi kx'} dx' \right|^2 dk, \quad (6.1)$$

A simple interpretation of microscopic image formation using Kohler illumination now emerges; the image may be described as an incoherent superposition of the intensities produced by coherent plane wave illumination. In other words, each point (source), or delta functional in the filter plane can be viewed as a spatially coherent source that produces a coherent image as described above; the intensity of each of these coherent images is then superimposed to produce the final image. Eq. 6.1 can also be rewritten in terms of their respective Fourier transforms:

$$I(x) = \iiint S(k)F(k_1)F^*(k_2)P(k+k_1)P^*(k+k_2)e^{j2\pi x(k_1-k_2)} dk_1 dk_2 dk, \quad (6.2)$$

where $P(k) = |P(k)|e^{jkW(k)}$ is the coherent transfer function with the pupil function $P(k)$. For the majority of cases, $P(k)$ is given by a circ-function with radius r , and the wavefront aberration $W(k)$ as mentioned in Section 2.6.7. It is clear from Eq. 6.1 that the observed image intensity is not linear in the complex (specimen) transmittance. Furthermore, it can be seen from Eq. 6.2 that the intensity spectrum consists of the mixing of pairs of spatial frequencies in the amplitude spectrum of the specimen; each pair (k_1, k_2) produces a cosine term with a frequency given by $(k_1 - k_2)$, a complex amplitude given by $F(k_1)F^*(k_2)$, which determines the weight of this cosine in the final image as well as the phase shift of the cosine angle. For this reason, this type of image formation is said to be bilinear[130]. Separating the contribution of the specimen and the system to image formation leads to the concept of the transmission cross-coefficient (TCC)[130, 157, 158]

$$TCC(k_1, k_2) = \iint S(k)P(k+k_1)P^*(k+k_2)dk, \quad (6.3)$$

which leads to a description of the transfer function for partially coherent image formation as follows:

$$I(x) = \iint F(k_1)F^*(k_2)TCC(k_1, k_2)e^{j2\pi x(k_1-k_2)}dk_1dk_2, \quad (6.4)$$

The case is now considered where $S(k)$ is given by three different color filters, $S_R(k)$, $S_G(k)$, and $S_B(k)$, where R , G , and B denote red, green, and blue. If it is assumed that the sensor recording the image is independently sensitive to red, green, and blue light, Eq. 6.3 and Eq. 6.4 can then be rewritten in terms of three independent transmission cross-coefficient terms as follows:

$$\begin{aligned} TCC_i(k_1, k_2) &= \iint S_i(k)P(k+k_1)P^*(k+k_2)dk \\ I_i(x) &= \iint F(k_1)F^*(k_2)TCC_i(k_1, k_2)e^{j2\pi x(k_1-k_2)}dk_1dk_2, \end{aligned} \quad (6.5)$$

where the index i in the above equations takes on three values R , G , and B . Here, it is assumed that the camera is capable of recording three independent images for red, green and blue light by using a Bayer mask or a temporal filter. In terms of image formation, each of these three images can be considered independently by taking into account only the illumination emerging from the red, green, or blue filter.

The most common filter for Rheinberg illumination uses only two colors; a central circ function containing one color (e.g. red) while a surrounding ring contains a second color filter, (e.g. green). In this case, the image is made up of two independent color images, $I_R(x)$ and $I_G(x)$ as described in Eq. 6.5 where

$$\begin{aligned} TCC_R(k_1, k_2) &= \iint circ_{r_1}(k)P(k+k_1)P^*(k+k_2)dk \\ TCC_G(k_1, k_2) &= \iint [circ_{r_2}(k) - circ_{r_1}(k)]P(k+k_1)P^*(k+k_2)dk, \end{aligned} \quad (6.6)$$

where r_1 and r_2 denote the radius of the inner and outer filters and $circ(k)$ represents a circ function in the Fourier domain[1]. In this case, the red image will be formed by contributions of $F(k)$ from only lower spatial frequencies while the green image will be formed by contributions of $F(k)$ from only higher spatial frequencies. The resulting image shows a sharp contrast in color content for regions containing low frequency background and higher frequency cellular features.

In order to better understand the role of the filter distribution on image formation, a simple case is now considered where each of the three filters is represented by a single point source, as illustrated in Fig. 6.1(a), which are modeled by Dirac delta functional as follows:

$$\begin{aligned} S_G(k) &= \delta(k) \\ S_R(k) &= \delta(k - \alpha) \\ S_B(k) &= \delta(k + \alpha), \end{aligned} \quad (6.7)$$

where α denotes a shift in the k_x and k_y dimensions. The transmission cross-coefficient terms for the three different images are given by:

$$\begin{aligned} TCC_G(k_1, k_2) &= P(k_1)P^*(k_2) \\ TCC_R(k_1, k_2) &= P(\alpha + k_1)P^*(\alpha + k_2) \\ TCC_B(k_1, k_2) &= P(-\alpha + k_1)P^*(-\alpha + k_2), \end{aligned} \quad (6.8)$$

Although image formation is bilinear and is given by the sum of interference terms within the bounds of overlapping pupil functions, it is possible to make some interesting conclusions based on Eq. 6.5 and Eq. 6.6. It is clear that image formation will result from contributions of the complex transfer function of the specimen $F(k)$ within the bounds of a pupil function $P(k)$ for the green image, $P(k + \alpha)$ for the red image, and $P(k - \alpha)$ for the blue image. In this discussion, the bilinear nature of image formation is not ignored; however, by dropping the variables k_1 and k_2 and considering only a single variable it is possible to focus only on the band of spatial frequencies within $F(k)$ that contribute to image formation (albeit in a non-linear manner based on interference terms).

In this way, it can be considered that optical staining will be based on the spatial frequency distribution of the specimen, as illustrated in Fig. 6.1(b); in this simplified example, the red image will be constructed from a finite band of spatial frequencies of $F(k)$ that are mostly negative in k_x , while the blue image is formed by contributions from a finite band of spatial frequencies of $F(k)$ that are mostly positive in k_x ; finally the green image is formed by contributions from a finite support of $F(k)$ around the origin.

It must be noted that the maximum spatial frequencies that can contribute to image formation, denoted by the dashed line in Fig. 6.1(b) will be bounded by

$$\sqrt{k_x^2 + k_y^2} < \frac{1}{\lambda}, \quad (6.9)$$

where λ is the wavelength of the quasi monochromatic light. Any spatial frequency components outside of this area contribute only to rapidly attenuating evanescent waves[1, 156]. The details of the derivation are provided in Section 2.3.4.

In the following section, the theoretical analysis presented here is used as the basis for the development of a numerical algorithm that is capable of simulating the process of image formation in an optical microscope utilizing Rheinberg illumination.

6.3 Digital simulation of Rheinberg illumination

Quantitative phase imaging techniques based on a partially coherent illumination, and digital holographic microscopy based on coherent illumination[101, 24, 8], both

produce an image of the specimen's complex transmittance, $t'(x)$, which it is assumed will be available as input to the algorithm under development in this section.

6.3.1 The general case

In the general case, the objective is to simulate optical Rheinberg illumination for a sample transmittance given by $t'(x)$; in terms of the original sample, *this is equivalent to first recording the quantitative phase image $t'(x)$ using material holography[1] and then using this material hologram as the sample in an optical microscope utilizing Rheinberg illumination.* The special case of simulating optical Rheinberg illumination of the actual original sample, with transmittance $t(x)$, is discussed in the next subsection. In order to simplify the analysis that follows the discussion is based only on continuous variables; their discrete counterparts are briefly discussed later. For the general case, the red image can be generated as follows:

1. Select a number of parameters. These include (i) deciding on the number of pinholes in the filter, and for each one deciding their color and position. Thus, the user selects a set of N red pinhole positions: $[\alpha_{R1}, \alpha_{R2}, \dots, \alpha_{RN}]$; (ii) deciding on the numerical aperture of the optical microscope that is being simulated. In simple terms this equates to selecting the radius, r_s , of the pupil function, $P_s(k)$, of the optical system to be simulated. Obviously $r_s \leq r$, since it will be impossible to improve on the resolution of the original image.
2. Simulate the illumination of $t'(x)$ with a plane wave of angle θ with respect to the optical axis, emerging from point source α_{R1} . The relationship between θ and α_{R1} is given by $\tan\theta = \alpha_{R1}/f$ where f is the focal length of the condenser lens. In the frequency domain, Step 2 is equivalent to shifting $F'(k)$ by an amount α_{R1} .
3. Simulate image formation in the microscope by convolving the image obtained in Step 2 with the point spread function of the microscope being simulated. In the frequency domain, Step 3 is equivalent to multiplying by $P_s(k)$.
4. Calculate the intensity of the resultant image.
5. Repeat Steps 2-4 for each of the $[\alpha_{R1}, \alpha_{R2}, \dots, \alpha_{RN}]$ pinhole positions to obtain the final red image.

The blue and green images can be obtained in the same manner using different sets of pinhole positions. It must be noted that it is possible for the shift in the frequency domain introduced in Step 2 to be large enough to result in $P_s(k)$ in Step 3 overlapping with no signal energy. Thus, it is important to judiciously select the pinhole positions, taking into account both the frequency support of the original

image as defined by P as well as the support of P_s . A simple algorithm can now be defined that makes use of the DFT[1, 38] which can be efficiently calculated using the fast Fourier transform algorithm. The algorithm is illustrated in Fig. 6.2. The previously described steps can be rewritten in terms of a computational algorithm as follows. For the red image only:

1. Select the set of pixel coordinates $[\alpha_{R1}, \alpha_{R2}, \dots, \alpha_{RN}]$ and pixel radius r_s , which is the radius of P_s .
2. Calculate the DFT of the input digital complex image t' .
3. Multiply the result of Step 2 with a binary mask given by a circular aperture of radius r_s and center coordinate α_{R1} . Then, calculate the inverse DFT.
4. Multiply each pixel value by its complex conjugate to obtain the intensity.
5. Repeat Steps 3-4 for each pinhole position given in Step 1 and add all of the resultant intensity images together to obtain the final red image.

In total, $N + 1$ DFTs must be calculated to generate the red image. The overall process is repeated for the blue and green images as illustrated in Fig. 6.2 and the final RGB image is obtained by combining these three independent images. It should be noted that the resolution of the final image will depend on the value of r_s .

6.3.2 The special case: simulation of optical Rheinberg illumination of the original transmittance $t(x)$

The general case described the situation where the original sample's transmittance $t(x)$ function is first recorded by a quantitative phase microscope with a complex point spread function $h(x)$, which provides a complex image $t'(x)$. The relationship between these three functions can be described in terms of their Fourier transforms as follows:

$$F'(k) = F(k)P(k), \quad (6.10)$$

Here, $P(k) = |P(k)|e^{jkW(k)}$ denotes the pupil function associated with the recording optical system, which is commonly assumed to be given by a circ-function and the wave-front aberration $W(k)$ as mentioned in Section 2.6.7, and $F(k)$ is the complex transfer function of the specimen. Going forward, this aberration is neglected (the effect of aberration can be reduced significantly using various compensation algorithms for quantitative phase imaging[20, 104, 105], and the pupil function is considered to be given only by a circ function with a radius $r \leq 1/\lambda$; i.e. it is assumed that the optical system introduces a spatially frequency cutoff less than or equal to the maximum permissible bandpass as described by Eq. 6.9. In this

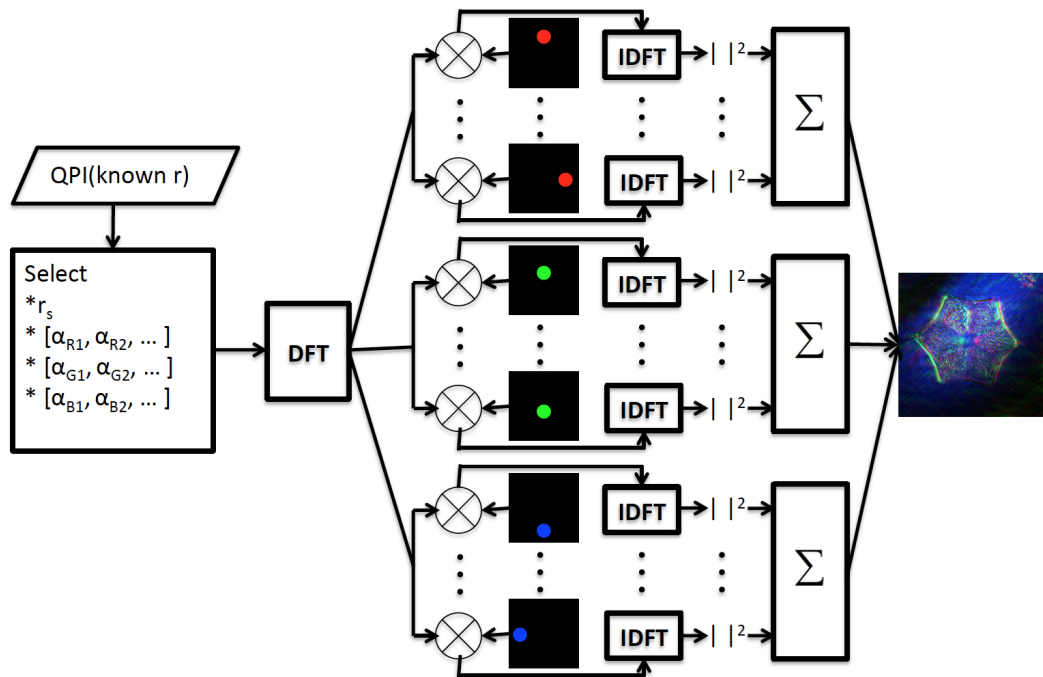


Fig. 6.2 Description of the algorithm that simulates optical Rheinberg illumination. Input to the algorithm is the quantitative phase image. The user selects the pinhole locations and the pupil radius for the optical microscope under simulation. A single DFT is calculated and stored for use as input to all of the remaining steps in the algorithm. For the red image this DFT is multiplied by a sequence of different binary masks, each one associated with a different point source (pinhole) in the filter plane. In each case an inverse DFT is calculated and the resultant intensity is stored. All of these intensities are superimposed to generate the final red image. The same procedure is applied for the red and green cases, each with their own set of unique pinhole positions.

case, it is clear that complex transfer function of the original specimen, $F(k)$, is available up to some bound, and therefore, it is possible to simulate the process of optical Rheinberg illumination on that original specimen so long as the algorithm parameters are chosen judiciously; this will be true so long as $|\alpha| + r_s < r$ for all pinhole positions α , where r and r_s denote the radius of the pupil function associated with the recording microscope and the simulated microscope respectively. It is clear that in order for the conditions of the special case to be met it is necessary that $r > r_s$ and therefore, the special case requires that the processed (color stained) image must be of lower resolution than the recorded image. In the next section results are shown for a number of diatom cells for both the general case and the special case.

6.4 Results

6.4.1 Recording of quantitative phase images

All of the quantitative phase images that were used to generate the results in this chapter were recorded using an off-axis digital holographic microscope with the same architecture as that described in detail in Section 2.6. This system uses a coherent laser with wavelength 633nm . The CCD camera has pixel pitch equal to $3.45\mu\text{m}$ in both spatial dimensions and a total pixel count given by 1024×1024 . The complex transmittance is obtained by spatial filtering the real image in the DFT domain as outlined in Ref.[101]. The images were in general not recorded at the exact image plane; the images were refocused using numerical propagation, specifically, using the spectral method outlined in Ref.[118, 65] and making use of autofocusing as described in Ref.[159] in order to determine the precise propagation distance. Aberration compensation was performed using the method described in Ref.[104], which involves capturing the complex transmittance of the illuminating beam (subject to the same processing as described for the sample) and dividing this into the complex transmittance recorded from the sample. This produces the final transmittance, which is input to the algorithm described in Section 6.3. A brief review of aberration compensation is provided in Section 2.6.7. Quantitative phase images are recorded of two diatom cells using two different microscope objectives (MO): a $20\times$ MO with $NA = 0.4$ and an oil immersion $63\times$ with $NA = 1.3$. In the subsections that follow the results are presented for seven different Rheinberg illuminations applied to these quantitative phase images.

6.4.2 The general case: simulation of Rheinberg illumination to complex transmittance recorded from a diatom cell with $20\times/0.4$ magnification

Here, the results are presented for simulated Rheinberg illumination of the complex transmittance recorded from a diatom cell using a $20\times/0.4$ MO. The raw hologram contains 1024×1024 pixels of size $3.45\mu m$ and, therefore, the DFT of this image contains 1024×1024 pixels of size $0.283mm^{-1}$. Taking into account the $20\times$ magnification, the sampling interval of the image is given by $0.173\mu m$ and the DFT has a sampling interval of $5.661mm^{-1}$. The real image comprises a circular section in the DFT plane with a radius of 95 samples. Therefore, $r = 95\times 5.661mm^{-1}$ and the full spatial frequency bandwidth of the real image is given by $2r$, which is approximately 1076 lines/mm. This is approximately in agreement with the Rayleigh criterion[1, 156], which predicts an optical resolution (the smallest distance between two observable points) to be equal to $0.61\times \lambda/NA = 0.965\mu m$. Spatial filtering involves isolating the area of approximately 190×190 samples within the DFT that contains the real image and performing an inverse DFT. This complex image is then subject to numerical propagation and aberration compensation as described in the previous section; these two processes have no effect on the bandwidth of complex image, i.e. the DFT of the final complex transmittance image still comprises a circular support of radius r . The intensity and phase components of this complex transmittance image are shown in Fig. 6.3 (a) and (b) respectively, following interpolation up to a size 2000×2000 by zero padding the DFT. A point of note is that this complex DFT must be zero padded up to a width that is at least double the bandwidth of the complex transmittance (i.e. at least 380 samples in this case) in order to guarantee that the intensity image shown in Fig. 6.3(a) is well sampled in the Nyquist sense[38].

Fig. 6.3(d) shows the result of simulated Rheinberg illumination for the color filter illustrated in Fig. 6.3(c). As discussed in the previous section this filter is simulated to exist in the back focal plane of the microscope condenser lens positioned for Kohler illumination; each point source in the back focal plane of the condenser is transformed to a plane wave illumination in the sample plane. In order to reduce computational complexity the simulation involves only nine point sources in total, comprising eight red point sources at positions $[\alpha_{R1}, \alpha_{R2}, \dots, \alpha_{R8}]$ located around a center green point source at position $\alpha_{G1} = (0, 0)$. Based on the discussion in Sections 6.2 and 6.3 we can expect this to result in the superposition of nine independent image intensities. Each of these nine images is obtained by spatial filtering different regions of the DFT of the complex transmittance function, as illustrated in Fig. 6.3(e), before returning to the spatial domain via an inverse DFT and taking the intensity of the resulting complex image. The overall algorithm describing this process is discussed in Section

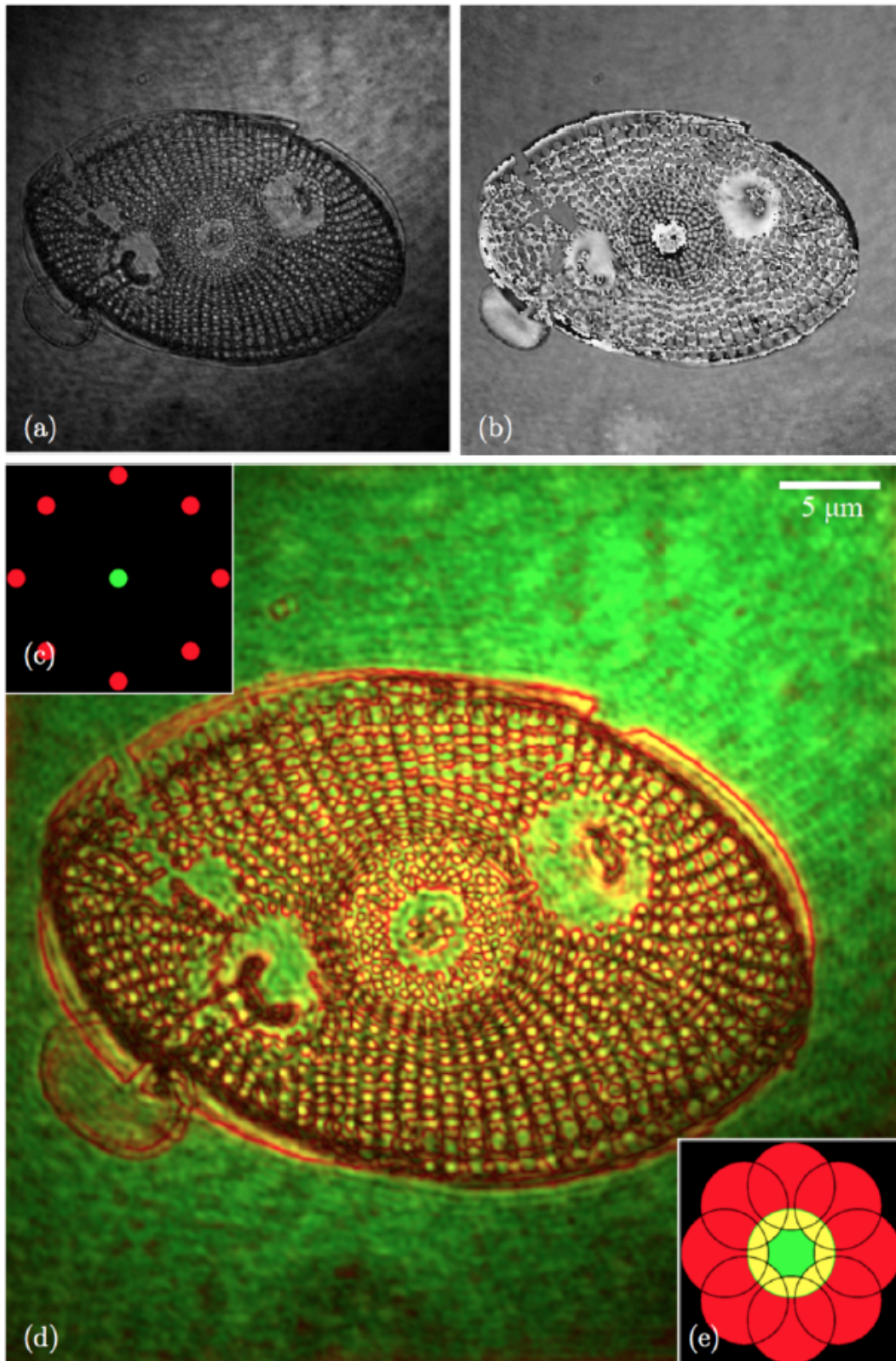


Fig. 6.3 Results for quantitative phase image of a diatom cell recorded with $20\times/0.4$ MO; (a) and (b) are the intensity and phase images of the recorded complex transmittance. (c) is an illustration of the Rheinberg filter that is simulated to be in the back focal plane of a microscope condenser lens, which is made up of eight red point sources located around a centre green point source; (d) The resulting image from simulated Rheinberg illumination; (e) illustrates the filtering process that takes place in the DFT domain, for each of the independent point sources in the filter. This filtering process is illustrated in more detail in Fig. 6.4(a).

6.3.1 and illustrated in Fig. 6.2. More detail on the color filtering process that takes place, more detail is provided in Fig. 6.4.

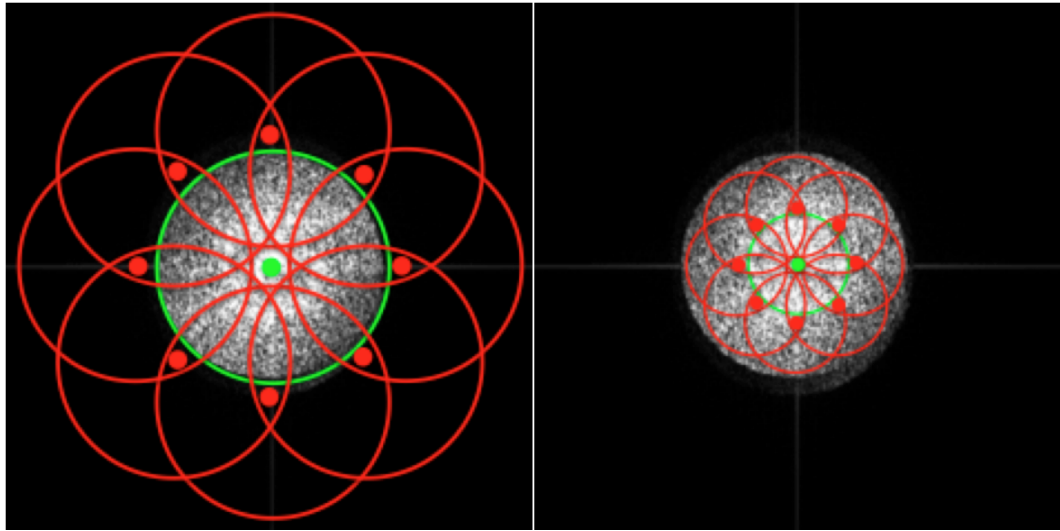


Fig. 6.4 Illustration of the color filtering that takes place in simulating Rheinberg illumination. (a) The general case: this image relates to the results shown in Fig. 6.3. The DFT of the complex transmittance that is input to the color staining algorithm is shown in the figure; the signal energy is contained in the center. The simulated color filter is shown as large red and green spots in the image, which represent point sources in the spatial frequency domain that are selected by the user. The user selects the radius of the circular filters, r_s , to be applied in the DFT domain. In this simulation, $r_s = r$. For each of the red masks, only a part of the spatial frequency support of the complex transmittance will contribute to the resulting intensity. The centre positions of the red filters are chosen such that none of the red masks will overlap with the center of the DFT, which guarantees that regions with only low frequency content, such as the background will appear as green. (b) Illustrates the special case where each of the masks lies entirely within the spatial frequency support of the complex transmittance; the resulting image is shown later in Fig. 6.9 and discussed in Section 6.4.3.

Fig. 6.4(a) illustrates the spatial frequency filtering that takes place in the simulation that produces the color stained image shown above in Fig. 6.3(d). The DFT of the complex transmittance (with amplitude and phase shown in Fig. 6.3(a) and (b)) is shown in the figure; in total 450×450 samples are shown. The signal energy is contained in a circular area with radius $r = 95$ samples. The simulated color filter is shown as large red and green spots in the image, which represent point sources in the spatial frequency domain. The number, color, and position of these point sources are decided by the user. Also decided by the user, is the numerical aperture of the microscope being simulated, which in simple terms means that the user selects the radius of the circular filters, r_s , to be applied in the DFT domain. In this case it was chosen that $r_s = r$ and, therefore, each circular mask used in the algorithm has the same radius as $P(k)$. Since, for the single green filter, all of the signal energy is

encompassed, it can be expected that the green image will be exactly equivalent to the grayscale intensity image shown in Fig. 6.3(a), with no loss in resolution. For each of the red masks, only a part of the signal energy will contribute to the resulting intensity. It can be expected, therefore, that each of the red images will contain reduced resolution when compared to the green image. However, each of these eight red images will contain information that relates to different higher spatial frequency bands, none of which overlap with the low frequency content at the center of the DFT; this is guaranteed if each red filter position obeys the following relationship: $|\alpha_{Ri}| > r$. In this case $|\alpha_{Ri}|$ is selected to be 100 samples for each of the red filters. Thus, it can be expected that the color stained image will contain no red component in areas of the image that contain only low frequencies, such as background areas.

In this example the DFT was zero padded up to a size of 450×450 samples, which guarantees that the intensity image shown in Fig. 6.3(a) is well sampled in the Nyquist sense. In terms of the algorithm illustrated in Fig. 6.2, it is more efficient to maintain a small image size. Not shown in Fig. 6.2 is the interpolation of the color image as a final step, which can be applied arbitrarily by the user. Interpolation up to a larger size, such as the 2000×2000 image shown in Fig. 6.3(d) can be applied to each of the final red, green, and blue images that are output by the algorithm. Four more color stained images of the same QPI are shown in Fig. 6.5, where in each case different color filters are applied, shown in the top left of each figure. In all cases it was chosen that $r_s = r$ and $|\alpha|$ was chosen to be 100 samples for all of the various filters, except for the green filter placed at the origin. The resulting filtering that takes place in the DFT domain are illustrated in the bottom right of each figure. In all four cases the color filters contain three different colors, blue, green and red and in all cases a single green spot in the center is used to create the low spatial frequency background, similar to the previous case shown in Fig. 6.3. For the four cases, the surrounding multiple blue and red spots emphasize different image features related to different subcellular structure. In Fig. 6.5(a), the filter contains a single red point source and a single blue point source in the left and right of the horizontal spatial frequency axis, respectively. Regions of the image that contain local frequency components that are captured in the corresponding circular filters will be stained with red and blue accordingly. Local spatial frequency can be related to the rate of change of the phase[1]; in this context, it can be inferred that image pixels with negative and positive phase gradients in the horizontal direction will be stained with blue and red color respectively. There is clear evidence of predominantly red and green regions in the image, and these areas can be compared with the quantitative phase image in Fig. 6.3(b) in terms of phase gradient; Fig. 6.6(a) provides an upsampled image of a cropped area of the image and there is clear evidence of color staining of subcellular features. In Fig. 6.5 (b) the result is shown for which the filter contains a single red point source and a single blue point source in the upper and lower parts of the vertical spatial frequency axis, respectively. The resulting color stained image

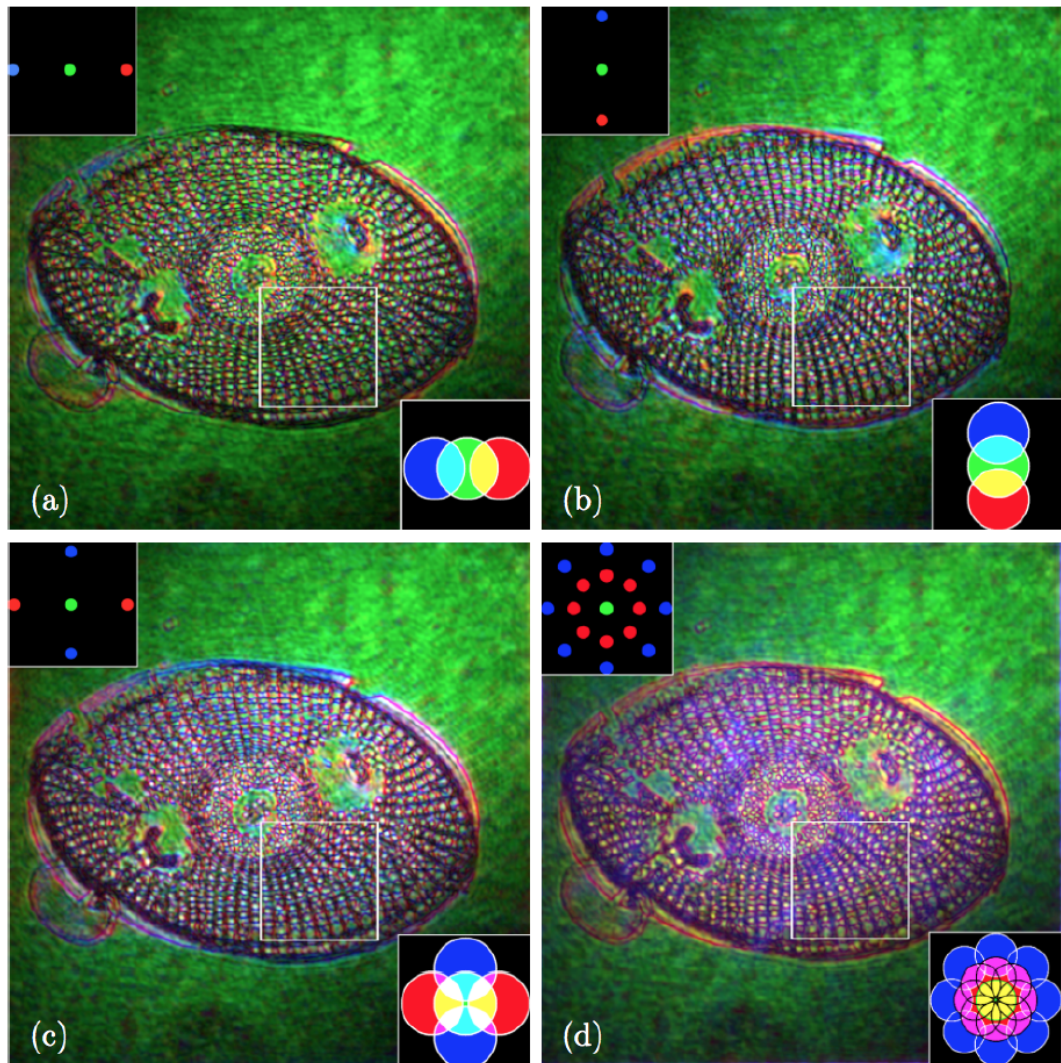


Fig. 6.5 Results of different simulated Rheinberg illumination applied to the same QPI shown in the previous example. The color filter used in each simulation is shown in the top left of each image, and the corresponding filters that are applied in the DFT domain are illustrated in the bottom right corner of each image. The individual parts, (a), (b), (c), and (d) are discussed in the text. The subsections from each of these images are shown in Fig. 6.6.

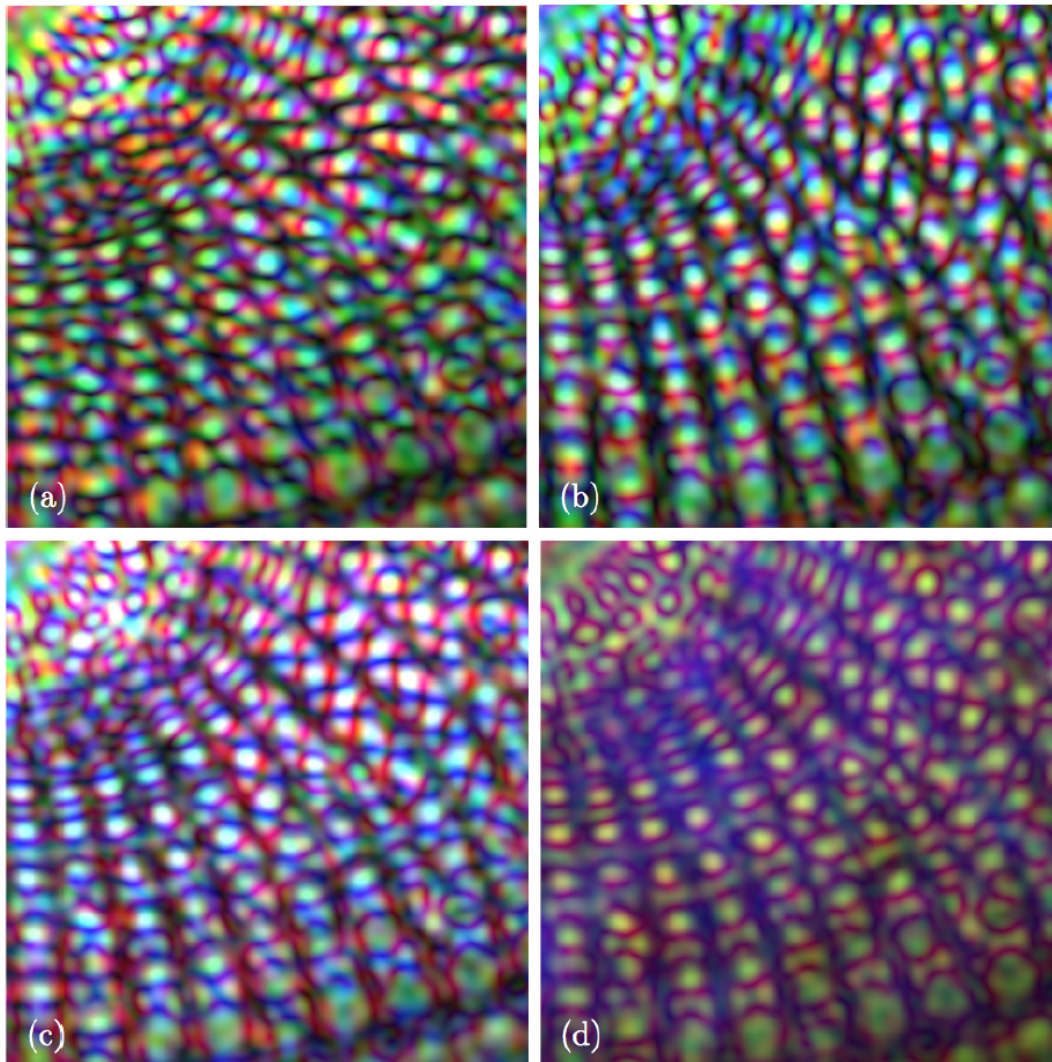


Fig. 6.6 Sections of images taken from Fig. 6.5 allowing for clearer inspection of the color staining of subcellular features, for each of the four color filters.

clearly shows red and blue color variation associated with subcellular features that are oriented in the vertical direction; features with phase gradient that are positive and negative are coded with red and blue color respectively, and these features are clearly visible in Fig. 6.6 (b). In Fig. 6.5 (c) (and Fig. 6.6 (c)) the color filter is made up of two red point sources placed in the horizontal dimension and two blue in the vertical. In this case image regions containing either positive or negative horizontal spatial frequencies will contain red staining, while blue staining will be applied to areas containing spatial frequency content in the vertical direction. Finally in Fig. 6.5 (d) and Fig. 6.6 (d) the result is shown for a filter containing a circular distribution of red point sources, around which is another circular distribution of blue point sources. In this case, it can be expected that the blue stain will appear in image regions containing only higher frequencies in the image, while the red stain will appear in a lower band of spatial frequencies, but not so low as to extend to the origin.

6.4.3 The general case: simulation of Rheinberg illumination to complex transmittance recorded from a diatom cell with $63\times/1.3$ magnification

Here, the results are presented for simulated Rheinberg illumination of the complex transmittance recorded from a diatom cell using a $63\times/1.3$ MO. As before, the raw hologram contains 1024×1024 pixels of size $3.45\mu m$ and, therefore, the DFT of this image contains 1024×1024 pixels of size $0.283mm^{-1}$. Taking into account the $63\times$ magnification, the sampling interval of the image is given by $54.76nm$ and the DFT has a sampling interval of $17.833mm^{-1}$. The real image comprises a circular area in the DFT plane with a radius of 95 samples. Therefore, the full spatial frequency bandwidth of the real image is given by $2\times 95\times 17.833mm^{-1}$, which is approximately 3388.27 lines/mm. This is in agreement with the Rayleigh criterion, which predicts an optical resolution (the smallest distance between two observable points) to be equal to $0.61\times \lambda/NA = 0.297\mu m$. Once again the area of approximately 190×190 samples so cropped from the DFT, which contains the real image an inverse DFT is performed. The resulting complex image is then subject to numerical propagation and aberration compensation.

In all of the following simulations, the same values for r_s and α are selected as for the corresponding cases in the previous example. The intensity and phase components of this complex transmittance image are shown in Fig. 6.7 (a) and (b) respectively, following interpolation up to a size 2000 by zero padding the DFT. Fig. 6.7 (d) shows the result of simulated Rheinberg illumination for the color filter illustrated in Fig. 6.7 (c). The corresponding filtering that takes place in the DFT domain is illustrated in Fig. 6.7 (e). Four more color stained images of the same QPI

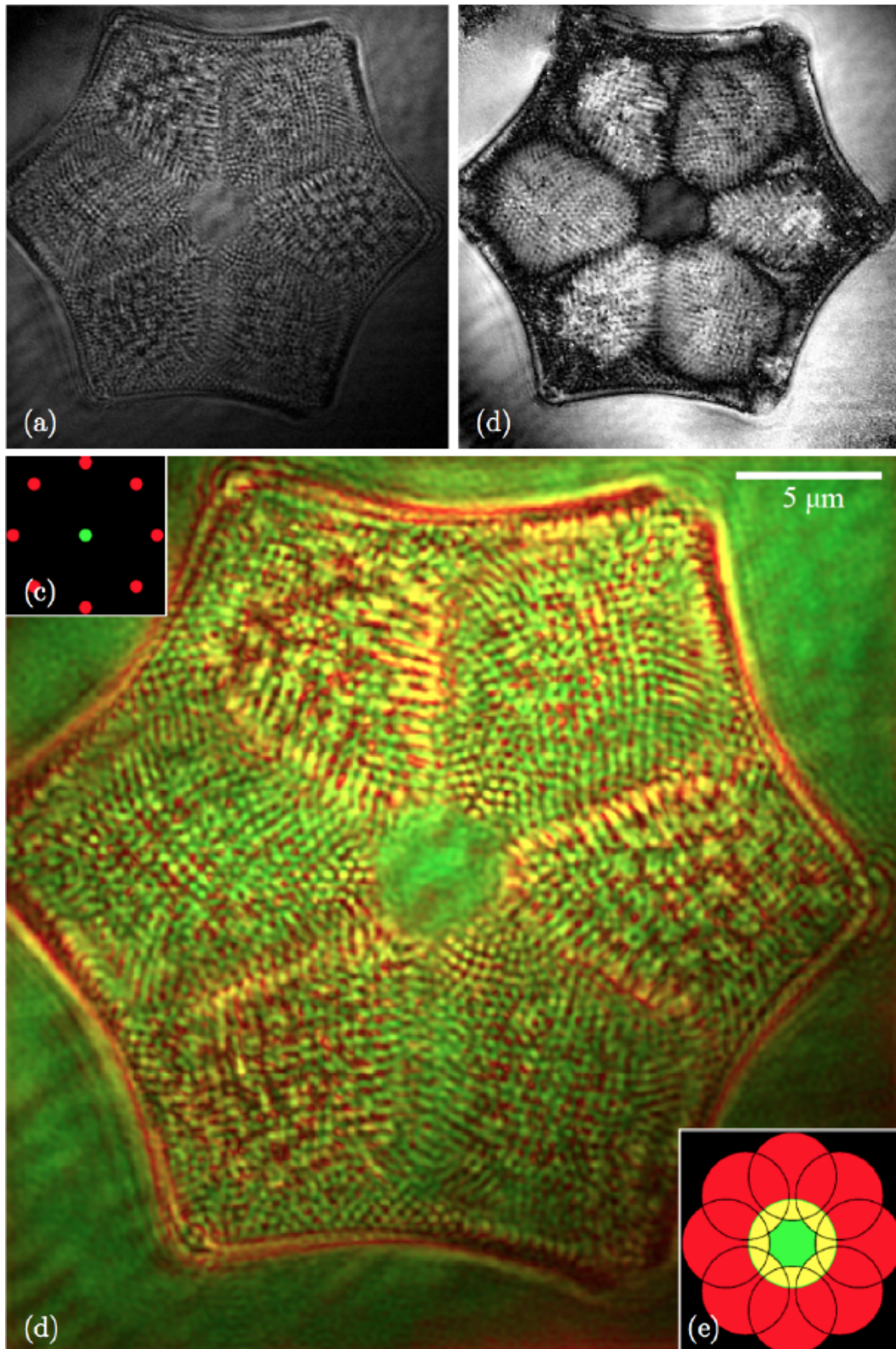


Fig. 6.7 Results for quantitative phase image of a diatom cell recorded with $63 \times /1.3 \text{ MO}$; (a) and (b) are the intensity and phase images of the recorded complex transmittance. (c) is an illustration of the Rheinberg filter used in the simulation; (d) The color stained image; (e) Illustration of the filtering process that takes place in the DFT domain, for each of the independent point sources in the filter.

are shown in Fig. 6.7, where in each case different color filters are applied, shown in the top left of each figure.

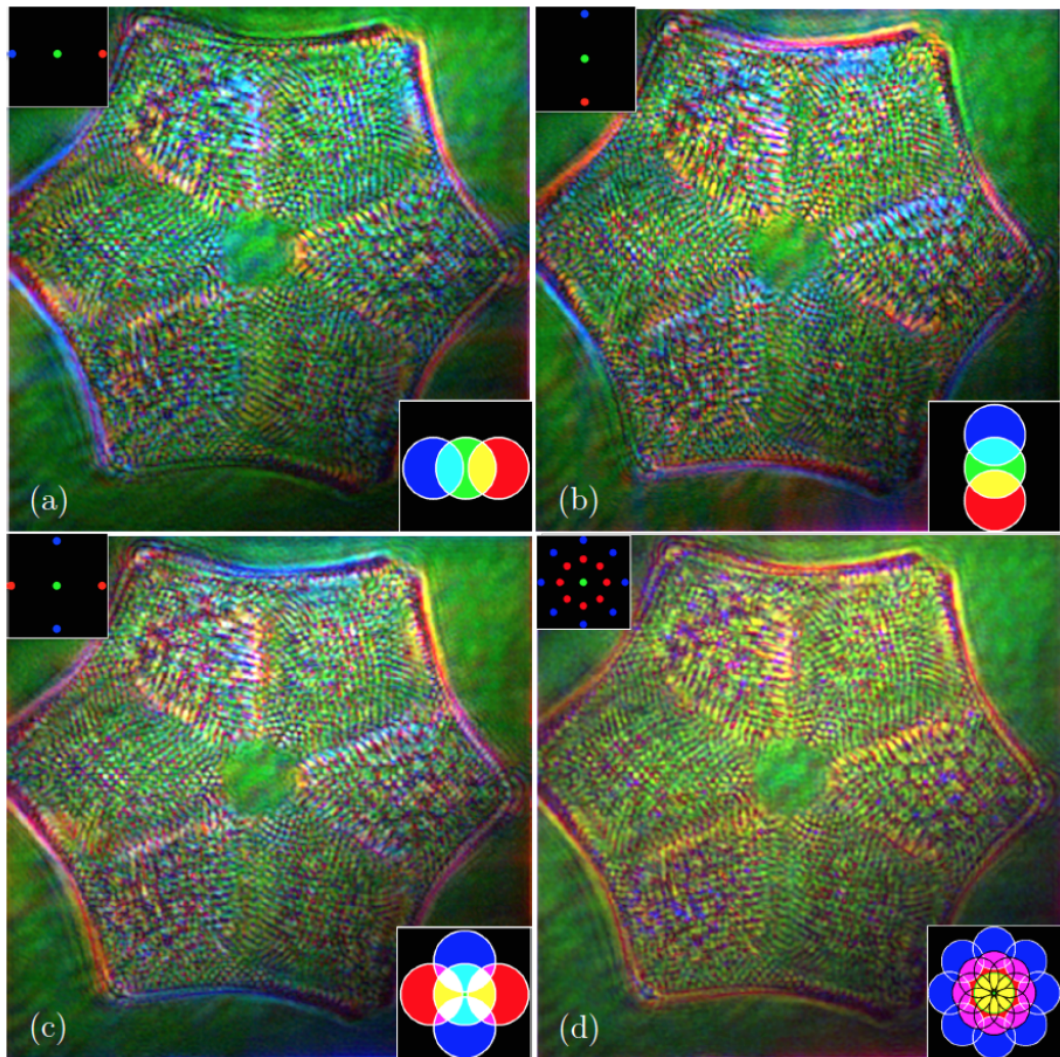


Fig. 6.8 Results of different simulated Rheinberg illumination applied to the same QPI shown in the previous example. The color filter used in each simulation is shown in the top left of each image, and the corresponding filters that are applied in the DFT domain are illustrated in the bottom right corner of each image.

The same color filters are used as in the previous example. The resulting filtering that takes place in the DFT domain is illustrated in the bottom right of each figure.

6.4.4 The special case: simulation of optical Rheinberg illumination of the original sample

All of the results presented so far have resulted from simulation using $r_s = r$, i.e., there is no loss in resolution for the (background) image. The other color images that are superimposed will all contain only part of the spatial frequency support, and will therefore have a reduced resolution; however it must be noted that these color

images will contain information from different spatial frequency bands. In Section 6.3.1 this was introduced as the general case, which was equivalent to recording a material hologram of the complex transmittance and placing this in an optical microscope with a given Rheinberg filter and a specified NA. In Section 6.3.2 it was proposed that it is possible to simulate optical Rheinberg simulation of the actual original sample under certain conditions. In light of the discussion thus far, these conditions can now be summarised as follows: all of the circular filters that are applied in the DFT domain must lie entirely within the spatial frequency support of the recorded complex transmittance, which is ensured with appropriate choice of r_s and the various pinhole positions. The result of color staining of the first QPI under the conditions of the special case is shown in Fig. 6.9 (a). The color filter is shown in the top left corner of the image and the corresponding filtering masks applied to the DFT are illustrated in the bottom right corner. These masks are more accurately illustrated in Fig. 6.4 (b). In this case r_s is chosen to be 45 samples and $|\alpha_{Ri}|$ is chosen to be 50 samples for all of the red pinholes. The resolution of the resulting image is, therefore, increased to $1.93\mu m$. This resolution is the same for each of the eight red images that are superimposed as well as the green background image, although each of these independent images will contain information from different bands within the spatial frequency support of the image. Fig. 6.9(b) shows a similar result except that in this case an additional six green pinholes are added to the Rheinberg filter. The value of r_s is chosen to be the same as that for the previous example and the red pinholes have the same positions as before. The additional six green filters have positions $|\alpha_{Ri}|$ at a radius of 20 samples. Due to the partial independence of the seven green masks in the DFT domain, a reduction in spatial coherence is expected, although no improvement in resolution can be expected. A similar set of results for the second QPI is shown in Fig. 6.9(c) and (d); the resolution of these images is equal to $0.594\mu m$ due to the different sampling interval for this case (see Section 6.4.3).

In order to highlight the reduction in spatial coherence brought about the inclusion of the six additional green filters sections from Fig. 6.9 are magnified and shown in Fig. 6.10. In both bases there is clear evidence of a reduction in the noise due to spatial coherence. It should be noted that this has not resulted from a reduction in resolution; the comparable images have identical resolution for the green component. The reduction in coherence is due to the superposition of different (partially) independent filters applied in the spatial frequency domain, each containing (partially) different background images, which are then averaged together. This process could be repeated indefinitely in order to further reduce the noise resulting from spatial coherence in the background image; however, in order to increase the number of green images and to ensure the independence of each of these, the value of r_s would have to be reduced, which in turn would reduce the final image resolution.

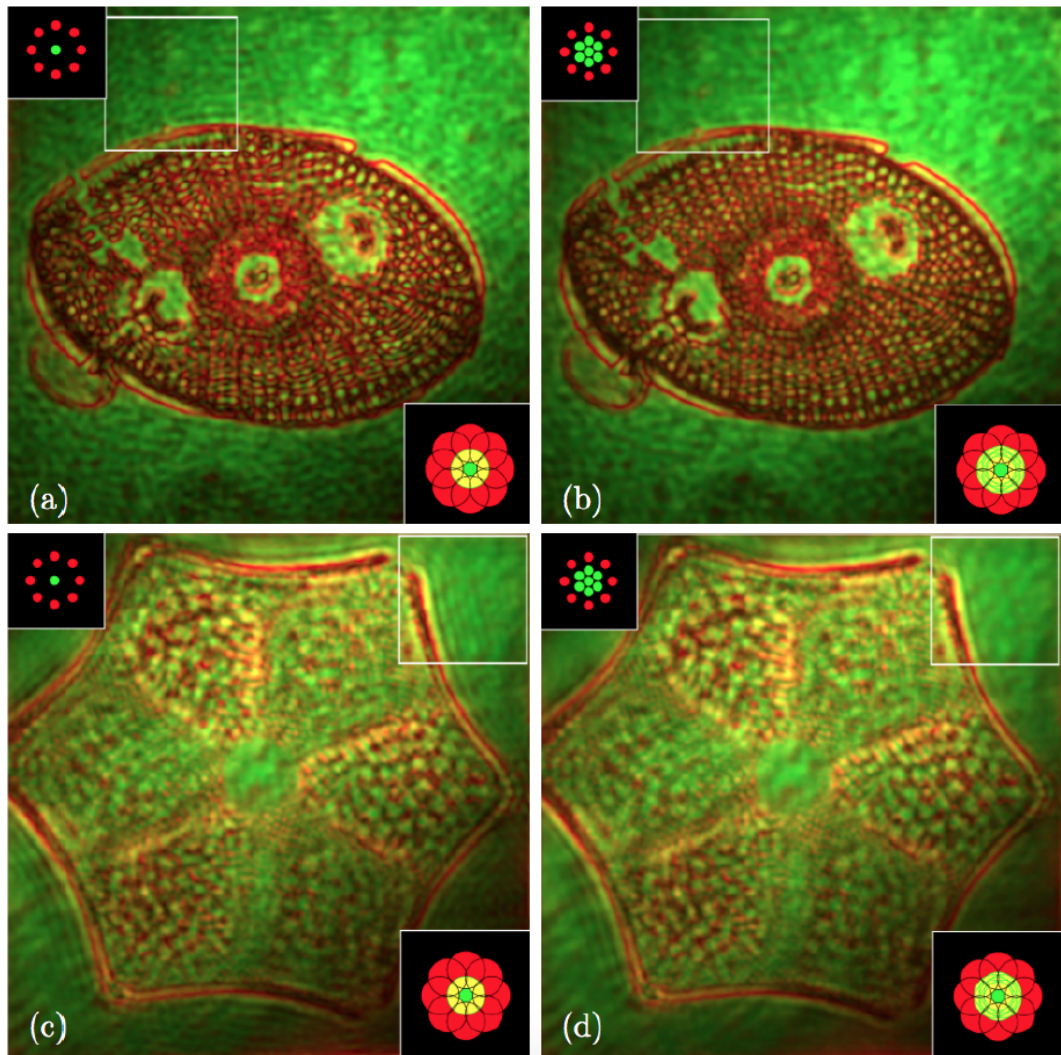


Fig. 6.9 (a) The result of color staining of the first QPI under the conditions of the special case. The color filter is shown in the top left corner and the corresponding filtering masks applied to the DFT are illustrated in the bottom right corner (note: these masks are more accurately illustrated in Fig. 6.4(b)); (b) shows a similar result except in this case a large number of green pinholes are used; due to the (partial) independence of the corresponding masks in the DFT domain, a reduction in spatial coherence is expected; (c) and (d) show the same set of results for the second QPI.

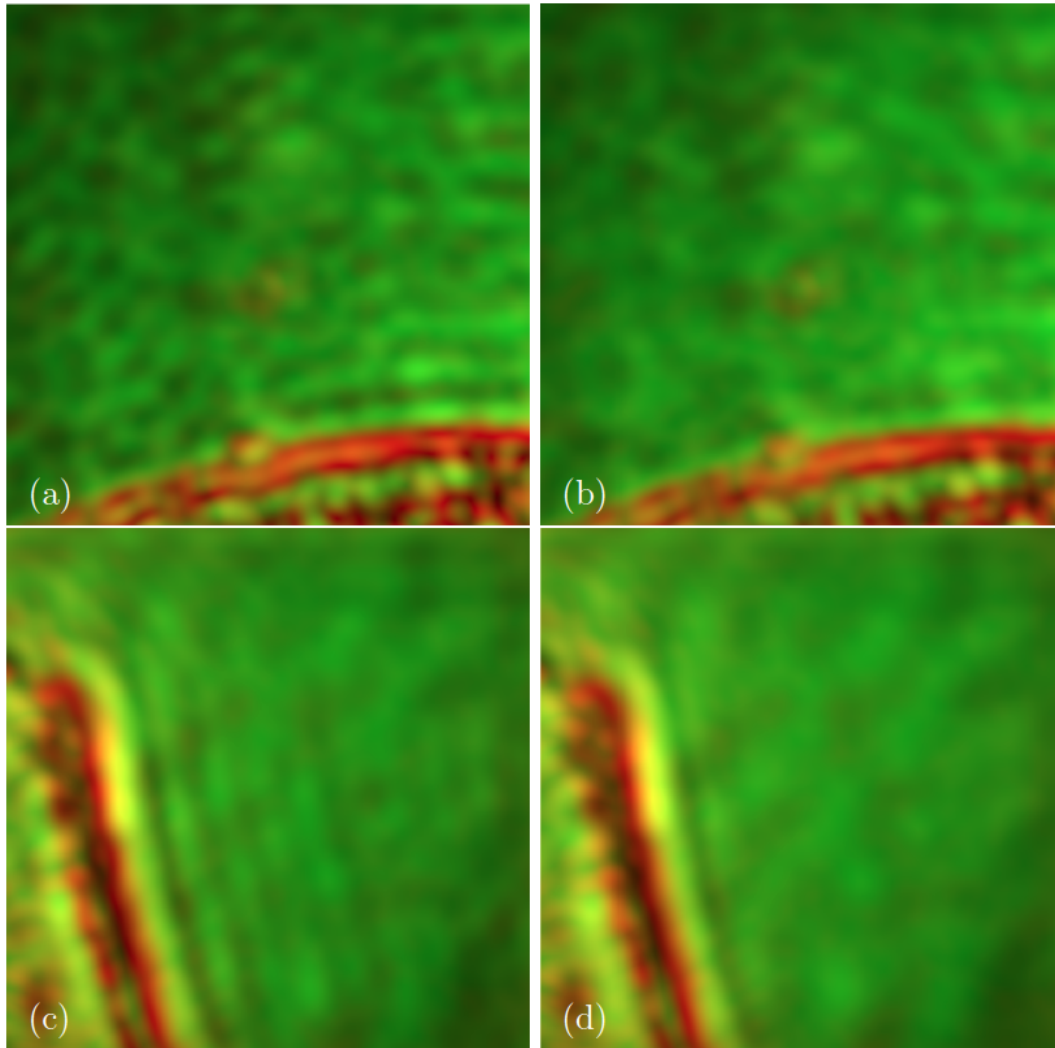


Fig. 6.10 Sections taken from corresponding images shown in the previous figure, highlighting a reduction in spatial coherence (but not resolution) due to the inclusion of additional independent filters.

6.5 Discussion

In this chapter a novel label-free color staining algorithm is proposed that can be applied to microscopic images of cells. A key requirement of the algorithm is the availability of the complex transmittance of the sample, which can be provided by digital holographic microscopy (which, was used to record the images that were processed in this chapter) or some other form of quantitative phase imaging.

It must be noted color coding in DHM/QPI is not new. Color coding of the quantitative phase image is commonly found in the literature. This approach usually involves simple thresholding, where color contrast is applied directly to the phase image based on the value of the phase. This approach should not be confused or conflated with the method proposed here, which is based on using a combination of different filters to generate different red blue and green image components.

As discussed in Chapter 1, the nucleus of the cell is an important focal point for the cytology. Chemical staining is always required for the cytology based diagnostics because cells or other biological samples can appear to be effectively transparent. The approach discussed in this chapter is entirely label free and may offer an alternative approach for nuclear staining.

In this chapter, we stained sub cellular features with colors by simulated Rheinberg illumination. In the following chapter, a new algorithm is proposed for label-free color staining of sub cellular features in a QPI that is considerably simpler in design. This algorithm is purely digital, and is not based on a simulation of an existing optical microscopy system.

Chapter 7

Label-free color staining of quantitative phase images

This chapter is on the preparation to be published as part of the following paper:

- Xin Fan, Kevin o' Dwyer, Bryan M. Hennelly. *Label-free color staining of quantitative phase images.*

7.1 Introduction

The goal of this thesis is to explore the cellular morphology of quantitative phase images of unstained biological samples, which are essentially invisible in ordinary bright-field microscopy, by digital holographic microscopy. In the previous sections, we are able to simulate Rheinberg illumination to color stain sub cellular features with a in-focus hologram of unstained biological samples. In this chapter, we finish our work with a new purely digital algorithm for label-free color staining of sub cellular features in a QPI that is considerably simpler in design with a variety of different results.

As discussed in the previous chapter, a convincing argument to suggest that QPI will replace the traditional dark-field, phase contrast, and DIC functionalities in future life science microscopes, is that the QPI image can be used as input to computational algorithms that calculate the dark field, phase contrast and DIC images with high accuracy [130]; this is in addition to providing direct quantitative information on morphology. Indeed, the availability of the complex transmittance of the sample, i.e. the QPI, permits the simulation of any optical system that could be used to image that sample; in the previous chapter we have demonstrated that it is also possible to simulate optical Rheinberg illumination using the QPI as input [X. Fan, J. J. Healy, B. M. Hennelly, *Adv. Pho., Sep. 2018*] for the purpose of applying label-free color staining to subcellular features. This algorithm was also demonstrated to have the capability to reduce the effect of coherent noise that may be present in the QPI [X. Fan, J. J. Healy, B. M. Hennelly, *Adv. Pho., Sep. 2018*]. In this chapter, a

new algorithm is proposed for label-free color staining of subcellular features in a QPI that is considerably simpler in design. This algorithm is purely digital, and is not based on a simulation of an existing optical microscopy system, as was the case for the previous work on Rheinberg illumination [X. Fan, J. J. Healy, B. M. Hennelly, *Adv. Pho., Sep. 2018*]. However, it is possible to postulate an optical analogue as discussed in Section 7.2. A maximum of four discrete Fourier transforms (DFT) are required, which can be implemented in the order of milliseconds using the fast Fourier transform (FFT) algorithm [38]. The simplicity of the approach facilitates a direct relationship between the color code in the image and the local spatial frequency at each point in the QPI [37, 156], which significantly enhances the usefulness of the method and the interpretation of the staining. We also believe there is significant scope to further develop this type of approach as detailed in the discussion section. The breakdown of this chapter is as follows: in Section 7.2 the method is described and interpreted in terms of local spatial frequency and an optical analogue is discussed; in Section 7.3 a variety of different results are presented supporting different advantages of the method and in Section 7.4 a brief discussion is offered including suggestions for future work.

7.2 Proposed algorithm and optical analogue

Quantitative phase imaging techniques[24, 127, 128, 130, 131, 160, 161, 122, 124] based on a partially coherent illumination[127, 128, 130, 131, 160, 161, 122, 124], and digital holographic microscopy based on coherent illumination[8, 101, 24], both produce a digital image of the specimens complex transmittance, which we denote as QPI, which it is assumed will be available as input to the algorithm under development in this section. In this section the proposed algorithm is defined and a simple optical analogue of this discrete process is discussed based on the optical Fourier transform(OFT)[37]. A brief definition of the Fourier transform as well local spatial frequency in an image is provided in Section 2.6. In Section 7.3 the resulting color-coded image is interpreted using the concept of the local spatial frequency and ray direction[37, 156].

7.2.1 Algorithm

The flowchart for the proposed algorithm is illustrated in Fig. 7.1 (a) and is defined as follows:

1. The first step is to select a color mask, M , with the dimensions $N_x \times N_y \times 3$, where N_x and N_y are the number of pixels in QPI in the two spatial dimensions and will be related to the number of pixels in the digital sensor that was used to record the QPI. The mask contains three separate real valued components, M_R , M_G , and M_B each of size $N_x \times N_y$, which represent the three distinct color

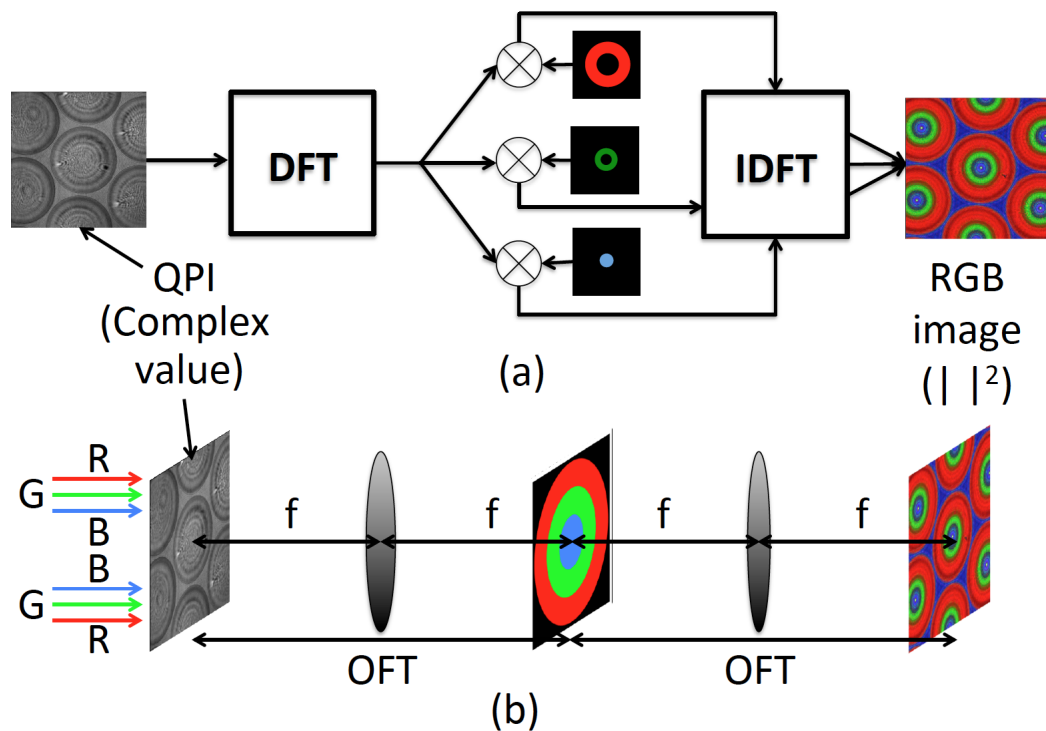


Fig. 7.1 (a) Flowchart of the proposed algorithm. A complex valued QPI is input to a DFT operation and the resultant complex image is separately multiplied by three different real valued filter masks before an inverse DFT operation is applied to each case. The intensity of the three resultant images make up the three RGB color components of the final image. (b) An optical analogue of the proposed algorithm in which three monochromatic coherent plane waves (red, green, and blue) are incident on a hologram representing the complex valued QPI. An OFT is used to transform the QPI to the spatial frequency domain where a multi band absorption filter is located, which contains different spectral responses for the three different wavelengths. A second OFT is used to transform back to the space domain. A color camera can be used to record the final image

filters that are to be applied in the Fourier domain in order to generate the red, green, and blue components of the final color image. The choice of color value selected for each pixel in M depends on the desired results; further details on expected results are given in Section 7.2 and Section 7.3. For the majority of the results presented in this chapter, the real valued masks, M_R , M_G , and M_B are selected to be binary valued and non-overlapping; the reason for selecting such a simple case is clarified in Section 7.2.2

2. The second step is to apply a two-dimensional (2D) DFT to QPI, which produces a complex valued image, $FQPI$, also of size $N_x \times N_y$.
3. The third step is to multiply the complex valued image $FQPI$ by each of the three real valued masks independently to produce three complex images: $FQPI \times M_R$, $FQPI \times M_G$, and $FQPI \times M_B$, where the multiplication symbol represents the multiplication of corresponding pixels, as opposed to matrix multiplication.
4. An inverse DFT operation is applied to each of the three complex images obtained in the previous step.
5. Finally the intensity of each of the resultant complex images is calculated, which are denoted as I_R , I_G , and I_B , and an RGB color image is constructed using these real-valued images as the red, green, and blue components. The three color components are, therefore, defined explicitly as follows:

$$\begin{aligned}
 I_R &= |IDFT\{DFT\{QPI\} \times M_R\}|^2 \\
 I_G &= |IDFT\{DFT\{QPI\} \times M_G\}|^2 \\
 I_B &= |IDFT\{DFT\{QPI\} \times M_B\}|^2,
 \end{aligned} \tag{7.1}$$

7.2.2 Notes on computation

Since the forward DFT operation need be calculated only once, a maximum of four DFTs are required, which require in the order of $(N_x \times N_y)^2$ operations. The fast Fourier transform algorithm can be used to efficiently calculate the DFT in the order of $\log_2(N_x \times N_y)$ calculations[38]. The overall algorithm, therefore, can be computed for most QPI image sizes in less than one second using a modern computer processor. Further speed up can be achieved using parallel computation on graphics processing units[162]. An additional speed-up can also be achieved if only two color components are required in the final image. In this minimum case, three DFT operations are required. It should be noted that there is a requirement to ‘zero pad’ the initial QPI image that is input to the algorithm and $N_x \times N_y$ represents this enlarged image size. This results from the discrete convolution that takes place in the space domain, which is a consequence of multiplication in the spatial frequency

domain in Step 3 above[38]. The enlarged size, $N_x \times N_y$, should be double the size of the original QPI (i.e. 4 times as many pixels). The larger size image will result in longer computation times.

7.2.3 Optical analogue

In Fig. 7.1 (a) an optical analogue of the proposed algorithm is illustrated. Three distinct plane waves are incident on a hologram of the complex valued QPI. These plane waves are coherent and monochromatic with wavelengths in the red, green, and blue regions of the visible spectrum. The QPI hologram is located in front of a convex lens at a distance equal to the focal length of the lens, f . The lens performs an optical Fourier transform (OFT)[37] with the spatial frequency domain located in the back focal plane, in which is placed a multiband filter. This filter contains three individual spectral responses relating to the red, green, and blue wavelengths. A second convex lens performs a second OFT and the space domain is located at the back focal plane in which is placed a color sensor. Digital cameras employing Bayer masks are capable of recording the intensities of the three different spectral components of a wavefield using different spectral filters on adjacent pixels. Although this optical system is not investigated further, it serves as a useful way to physically interpret the proposed algorithm.

7.3 Interpretation of the algorithm in terms of local spatial frequency

In Fig. 7.2 some initial results are presented in order to assist in the interpretation of the algorithm in terms of optical image formation. This description is based on interpreting the results of the color-staining algorithm proposed in Section 7.2, applied to the QPI of a microlens array, in terms of local spatial frequency as well as ray direction. The Fourier transform as well as local spatial frequency in an image using the approach of Goodman[37] is briefly defined in Section 2.6, before applying these concepts to a microlens array.

7.3.1 Local spatial frequencies in a microlens array

Using the thin lens approximation, a lens with focal length f and diameter $2r$ can be described as a (phase-only) two-dimensional chirp function and a microlens array with a pitch of P_x and P_y in x and y can be described as a superposition of a number of such functions uniformly shifted, described as follows:

$$Lens_{f,r}(x,y) = \exp \left[\frac{j\pi}{\lambda f} (x^2 + y^2) \right] circ_r(x,y) \quad (7.2)$$

$$Lens_array(x,y) = \sum_{m_x=-M_x/2}^{M_x/2} \sum_{m_y=-M_y/2}^{M_y/2} Lens_{f,r}(x - m_x P_x, y - m_y P_y) \quad (7.3)$$

where M_x, M_y , are related to the number of lenses appearing in the microlens array in both spatial dimensions, λ is the wavelength of the incident light, and $circ_r(x,y)$ is commonly defined[37] as follows:

$$circ_r(x,y) = \begin{cases} 1 & x^2 + y^2 < r^2 \\ 1/2 & x^2 + y^2 = r^2 \\ 0 & x^2 + y^2 > r^2 \end{cases} \quad (7.4)$$

The Fourier transform of the lens and lens array function that are defined in Eq. 7.2 and Eq. 7.3 can be shown to be defined as follows:

$$F_{Lens}(k_x, k_y) = j\lambda f \exp[-j\pi\lambda f(k_x^2 + k_y^2)] * \frac{J_1\left(\frac{2\pi}{r}\sqrt{k_x^2 + k_y^2}\right)}{\frac{1}{r}\sqrt{k_x^2 + k_y^2}} \quad (7.5)$$

$$F_{Lens_array}(k_x, k_y) = F_{Lens}(k_x, k_y) \sum_{m_x=-M_x/2}^{M_x/2} \sum_{m_y=-M_y/2}^{M_y/2} \exp[-j2\pi(x - m_x P_x, y - m_y P_y)] \quad (7.6)$$

where the asterisk symbol in Eq. 7.5 denotes a two-dimensional convolution operation over k_x and k_y . The term on the left of this asterisk is the Fourier transform of the chirp function in Eq. 2.1 in Section 2.6 and the term on the right side is the Fourier transform of the circ function. J_1 represents a Bessel function of the first kind, order 1. It is notable that this function is circularly symmetrical and could have been written more succinctly using polar coordinates. Eq. 7.5 is derived on the basis that multiplication in the space domain is equivalent to convolution in the spatial frequency domain. Eq. 7.6 is derived using both the shifting and linearity theorems of the Fourier transform[38, 37]. It can be seen from Eq. 7.6 that the Fourier transform of the lens array is identical to that of the lens, which is modulated by the summation term. Each individual term in this summation relates to the shift associated with the position of each individual lens within the array.

The local spatial frequency components of the lens and lens array functions that are defined in Eq. 7.2 and Eq. 7.3 are defined below in Eq. 7.7 and Eq. 7.8 respectively:

$$k_{IX} = \frac{x}{\lambda f} circ_r(x,y) \quad k_{IY} = \frac{y}{\lambda f} circ_r(x,y) \quad (7.7)$$

$$k_{IX} = \sum_{m_x=-M_x/2}^{M_x/2} \sum_{m_y=-M_y/2}^{M_y/2} \frac{(x - m_x P_x)}{\lambda f} circ_r(x - m_x P_x, y - m_y P_y) \quad (7.8)$$

$$k_{IY} = \sum_{m_x=-M_x/2}^{M_x/2} \sum_{m_y=-M_y/2}^{M_y/2} \frac{(y - m_y P_y)}{\lambda f} circ_r(x - m_x P_x, y - m_y P_y)$$

For the case of the lens function, it is clear that the local spatial frequencies depend on the spatial positions; the local spatial frequencies are zero at the centre of the lens and they increase linearly with respect to distance from the centre with a slope of $1/\lambda f$ within the boundary defined by the circ function. For the case of the lens array, a similar dependency of local spatial frequency on spatial positions is seen; in this case, however, it can be seen that these local spatial frequencies are periodic in x and y .

For the case of the lens, the local spatial frequencies defined by Eq. 7.7 are clearly counted by the circ function. One may be tempted to conclude that $F_{Lens}(k_x, k_y)$ must, therefore, be similarly bounded and might even expect the Fourier transform to be flat within this bounded region since each local spatial frequency appears once in Eq. 7.7. Calculation of Eq. 7.5 reveals that this is approximately true; the Fourier transform is approximately bounded by a similar region and is also approximately flat within this region. A similar analysis is provided for the case of a square lens in Chapter 2 in Ref.[37].

In the next section, the QPI of a microlens array is investigated and processed with the algorithm described in Section 7.2. The results are interpreted in the context of the local spatial frequencies defined in Eq. 7.8.

7.3.2 Color staining the QPI of a microlens array

The QPI of a microlens array sample (with lens diameter $2r = 240\mu m$, focal length $f = 8mm$, and pitch $P_x = P_y = 250\mu m$) was recorded using a DHM system, which is described in more detail in Section 7.3. A $20\times$ microscope objective ($NA = 0.4$) was used to record the QPI. In the discussion that follows, no particular attention is given to specific space or spatial frequency coordinates (these can be determined by using the methodology outlined in 7.4); rather, a simple qualitative description is presented with the goal of providing an understanding of the color coding that appears in the final image following application of the algorithm proposed in Section 7.2.1.

Disregarding the point spread function of the recording system, the complex image that is recorded, i.e. the QPI, can be described as the complex function appearing in Eq. 7.3. The amplitude, A , and unwrapped phase, φ , of the microlens array are shown in Fig. 7.2 (a) and (b) respectively, which result from the numerical reconstruction of the digital hologram. A depth map is shown in Fig. 7.2 (c). For the discrete case in which the QPI is recorded using a digital camera sensor, the x and y coordinates in Eq. 7.3 are defined by discrete sample coordinates $x \rightarrow n_x \delta x$, and $y \rightarrow n_y \delta y$ where n_x , and n_y are integer indices representing the discrete sample (pixel) positions and δx , and δy represent the sampling intervals in the x and y directions (δ_x and δ_y) and will be equal to the camera pixel size. The values of n_x , and n_y will take all integer values in the ranges $-N_x/2 \rightarrow N_x/2 - 1$ and $-N_y/2 \rightarrow N_y/2 - 1$, respectively. In Fig. 7.2 (c) the unwrapped phase is shown, as well as the surface

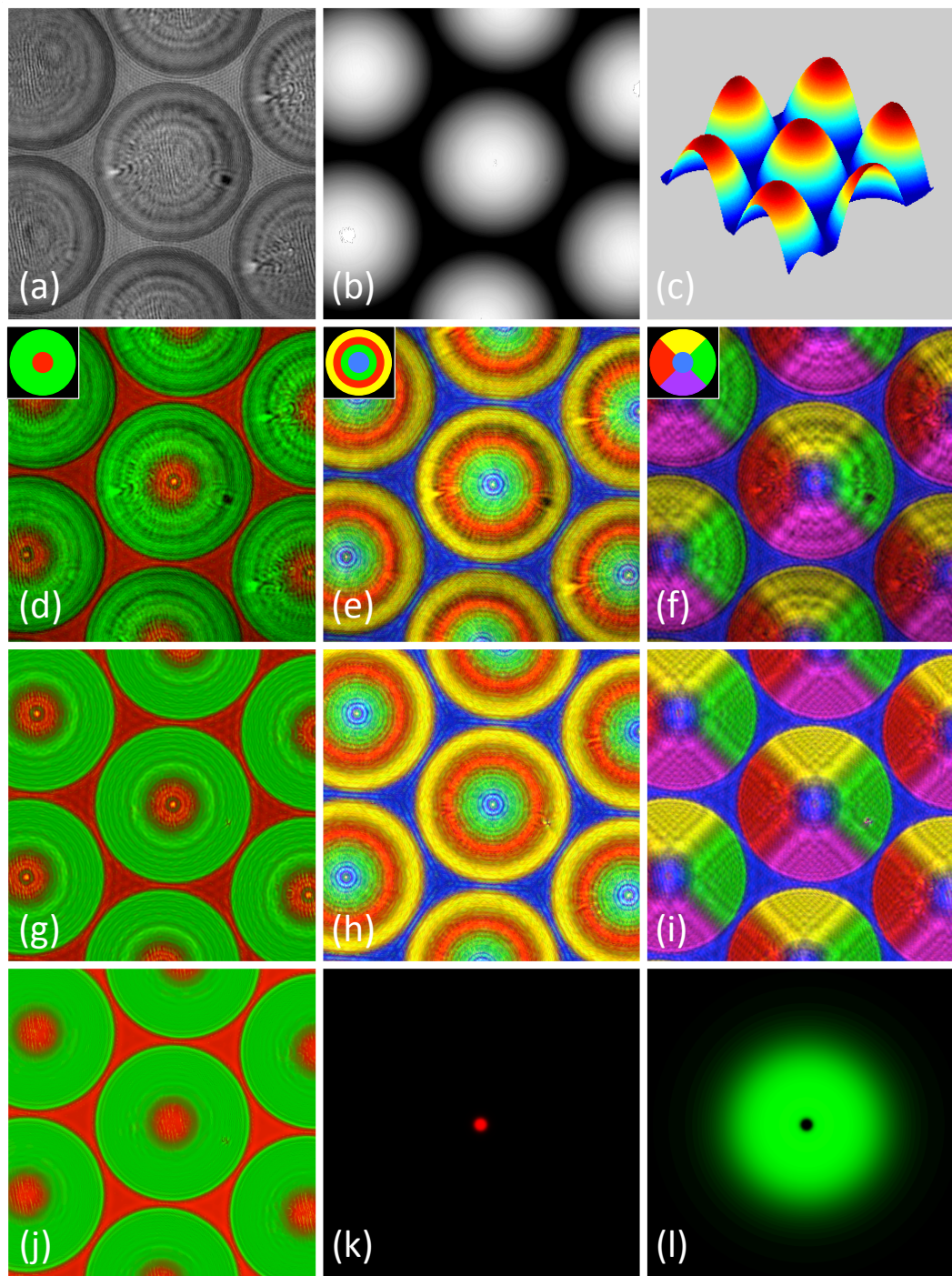


Fig. 7.2 A set of initial results using a QPI of a microlens array (recorded using a $20\times/0.4$ microscope objective) that assist in describing and interpreting the proposed algorithm. (a), (b), and (c) show the amplitude, unwrapped phase, and depth map of the QPI that is input to the algorithm; (d), (e), and (f) are the color stained images resulting from the filters shown in the top left of each image; (g), (h), and (i) show the same set of results for the case where the amplitude of the QPI is normalized before processing.

profile (depth map) that is rendered using the unwrapped phase, as well as the laser wavelength and the refractive index of the material.

Three different color filters were selected to color stain the image, which are applied in the DFT domain; this domain contains $N_x \times N_y$ samples with sampling intervals Δ_x , and Δ_y given by $1/N_x \delta_x$ and $1/N_y \delta_y$. The sample intervals in the space and DFT domains should be divided by, and multiplied by, the magnification of the system respectively, which in this case is 20. The set of initial results of the proposed algorithm are shown in Fig. 7.2 (d), (e), and (f). In the top right corner of each figure the color filter applied in the DFT domain is illustrated. The filter used in Fig. 7.2 (c) is circularly symmetrical and is composed of a central red filter with a radius of 40 samples and a green filter in the shape of green annulus defined by an inner radius of 41 samples and an outer radius of 150 samples, which encompasses the entire spatial frequency support of this QPI.

It can be expected that the background area, for which we can expect low values of local frequency (the rays pass almost straight through with very small angles of refraction), will be colored in red, while all other local frequencies, which correspond to geometrical rays that have been refracted to higher angles are colored in green. The periodicity of the color coding in the resulting image, which is predicted by Eq. 7.8, is clear to see; the areas between the microlenses are colored red and the centre of each microlens is also red, which is expected due to the low rate of change of the phase delay (low rate of change of the height/thickness of the quartz). All other areas in the micro lenses are color coded in green as predicted by Eq. 7.8 for this particular filter. The two filters used in this case were both binary valued.

In Fig. 7.2 (e), a red, green, and blue filter are used. The blue filter is circular with a radius of 40 samples. This blue filter is binary valued while the red and green filters are both ternary valued. The green filter is comprised of two annuli with two different amplitudes; the first annulus has an inner radius of 41 samples and an outer radius of 60 samples and an amplitude of 1, while the second annulus has an inner radius of 121 samples and an outer radius of 150 samples (150 samples encompasses the entire spatial frequency support of this QPI) and an amplitude of 0.5. Similarly the red filter is comprised of two annuli with two different amplitudes; the first annulus has an inner radius of 61 samples and an outer radius of 120 samples and an amplitude of 1, while the second annulus has an inner radius of 121 samples and an outer radius of 150 samples (which therefore overlaps with the second green annulus) and an amplitude of 0.5. Therefore, the filter is comprised of four colors: blue, green, red, and yellow, which is given by the sum of the red and green annuli. This four-part color scheme appears in each of the micro lenses as expected.

The previous examples have employed circularly symmetrical filters, a five part color scheme is used in the filter in Fig. 7.2 (f). In this case the filter is not circularly symmetrical and is comprised of a blue circle of radius 40, which will again correspond to small values of local spatial frequency (background). Beyond

the blue filter the four quadrants are given by red, yellow, green, and purple and extend out beyond the spatial frequency support of the QPI. As expected, this color pattern is repeated in each of the individual micro lenses, once again validating the assumption that the color filters correspond to bands of local spatial frequencies within the image, which in turn relate to solid angles of geometrical rays that are refracted by the sample.

It is notable that the concept of local spatial frequencies relates only to the phase of a function. Therefore we can expect that the amplitude will contribute to the color pattern that makes up the final image. However, the amplitude will overlay the color scheme and may assist in the visualization and interpretation of the image. In some cases, however, it may be preferable to omit the amplitude entirely before applying the color staining algorithm. In Fig. 7.2 (g), (h), and (i) the same set of filters are applied but this time the input to the algorithm is only the phase component of the image, $\exp[\varphi(x,y)]$. A similar set of results are found; however, in this case the color image is improved by removing the amplitude and thereby permitting a clearer view of the local spatial frequencies. This also serves to clarify the unwanted effect of diffraction caused by the hard edges of the binary and ternary valued filters[37]. This unwanted ringing around edges resulting from (in this case the edges are the boundaries between different bands of local spatial frequencies) resulting from ideal filters is sometimes referred to as Gibb's phenomenon in the area of digital signal processing[38]. In order to mitigate this effect, filters with gradual transitions have been developed such as the Butterworth band pass filter[38] which is used to create the image shown in Fig. 7.2 (j). In this case, a third order low-pass circularly symmetrical Butterworth filter (cut-off at 40) was used to generate the red image; this red filter is shown in Fig. 7.2 (k). A third order band-pass Butterworth filter, as shown in Fig. 7.2 (l) was used to generate the green image. The resulting image is significantly improved when compared with Fig. 7.2 (d) and (j) and bands of local spatial frequency are represented in color with greater accuracy. For filters with arbitrary shape such as that used in Fig. 7.2 (f) the design of smoothly varying Butterworth (or similar) filters may not be straightforward.

This latter two results are shown only for discussion and may form the basis of future work; for simplicity, all of the remaining results that follow in this chapter use binary non-overlapping rgb filters. All of the filters that are used are binary and, therefore, hard edged. Furthermore, the full QPI is used in all of the results that follow. i.e. no normalization of the amplitude is applied in advance of color staining.

7.4 Results

All of the QPIs that were used to generate the results in this chapter were recorded using an off-axis DHM with the same architecture as that described in detail in Ref[162]. This system uses a coherent laser with wavelength $633nm$. The CCD

camera has pixel pitch equal to $3.45\mu\text{m}$ in both spatial dimensions and a total pixel count given by 1024×1024 . The complex transmittance is obtained by spatial filtering the real image in the DFT domain as outlined in Ref[160]; for all holograms appearing in this chapter, the real image comprises a circular section in the DFT plane which is isolated using a circular filter of radius 150 samples and centered. For all cases, an inverse DFT is applied, followed by numerical propagation, and aberration compensation to provide the QPI, which is input to the color staining algorithm.

The images were in general not recorded at the exact image plane; the images were refocused using numerical propagation, specifically, using the spectral method outlined in Ref[38, 37] and making use of autofocusing as described in Ref[162] in order to determine the precise propagation distance. Aberration compensation was performed using the method described in Ref[54], which involves capturing the complex transmittance of the illuminating beam (subject to the same processing as described for the sample) and dividing this into the complex transmittance recorded from the sample. This produces the final QPI, which is input to the algorithm described in Section 7.2.

7.4.1 Initial results for a number of biological samples

A QPI of a diatom cell was recorded using a $20\times$ microscope objectives (MO) with $NA = 0.4$. The raw hologram contains 1024×1024 pixels of size $3.45\mu\text{m}$ and, therefore, the DFT of this image contains 1024×1024 pixels of size 0.283mm^{-1} .

Taking into account the $20\times$ magnification, the sampling interval of the image is given by $0.173\mu\text{m}$ and the DFT has a sampling interval of 5.661mm^{-1} . The reconstructed amplitude, A , and unwrapped phase, φ , are shown in Fig. 7.3 (a) and (b). In Fig. 7.3 (c) and (d) are shown the color stained images resulting from applying the two color filters shown in the bottom right corners of the two images. Also shown in the images are enlarged regions that highlight the visualization of subcellular features with significantly improved contrast. The filter in Fig. 7.3 (c) is circularly symmetrical and is composed of a central red filter with a radius of 40 samples and a green filter in the shape of green annulus defined by an inner radius of 41 samples and an outer radius of 150 samples, which encompasses the entire spatial frequency support of this QPI. The background area, for which we can expect low values of local frequency (the rays pass almost straight through with very small angles of refraction), is colored in red, while all other local frequencies are colored in green. The filter in Fig. 7.3 (d) is asymmetrical and is composed of a central blue filter, again with a radius of 40 samples, as well as a red and green filter, which make up the upper and lower half of an annulus the shape of which is once again defined by an inner radius of 41 samples and an outer radius of 150 samples. In this case we can expect the background to be blue, while all higher local spatial frequencies will either be

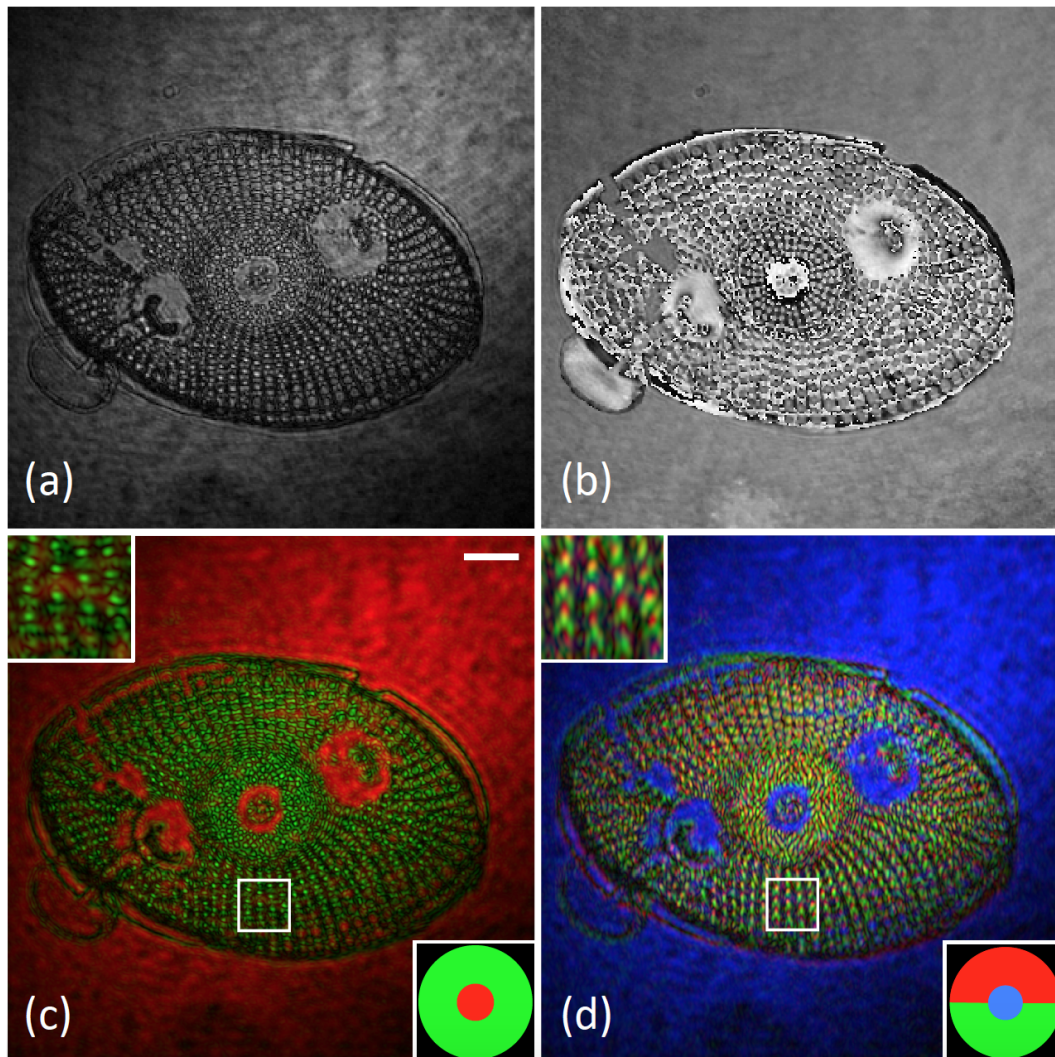


Fig. 7.3 Results for quantitative phase image of a diatom cell recorded with $20\times/0.4$ MO; (a) and (b) are the intensity and phase images of the recorded complex transmittance. (c) shows the result of color staining using the circularly symmetrical filter illustrated in the bottom right corner and (d) shows the result of staining using the red, green, and blue filter. The white resolution bar in part (c) signifies a length of $10\mu\text{m}$.

red or green depending on whether they are positive or negative in k_y . The resulting image enables the subcellular features to be clearly visualized with excellent contrast. For this case, it must be noted that the three color filters do not overlap in the DFT domain and, therefore, it is tempting to expect that only red, green, and blue colors will be visible in the final image; this would be consistent with the idea of unique local spatial frequencies within the image. However, it is clear that other colors exist within the image which result from some mixture of red, green, and blue. This results from either (i) diffraction associated (or Gibb's phenomenon[38]) with the hard edges[37] of the three binary valued filters, and/or (ii) the inconsistency that exists between the true spatial frequencies and the concept of local spatial frequency. Despite the fact that this mixing of colors from the different filters is more difficult to interpret than the basic idea of local frequency, it nevertheless contributes to the contrast in the image and further emphasizes subcellular features. Some further examples are given in Fig. 7.4, which include two more diatom cells recorded using $63 \times /1.3$ (oil immersion) and $20 \times /0.4$ objectives as well as a barley awn and an insect recorded using $10 \times /0.3$ and $2.5/0.08$ objectives. For all four cases the raw hologram contains 1024×1024 pixels of size $3.45 \mu m$ and, therefore, the DFT of this image contains 1024×1024 pixels of size $0.283 mm^{-1}$. In order to take into account the magnification, M , for each specific case, the sampling interval for the image can be recalculated as $3.45/M \mu m$ and for the DFT as $0.283 \times M mm^{-1}$. The color filter shapes and sizes (in terms of DFT samples) are given in Fig. 7.4; for simplicity, binary non-overlapping color filters were used in each case. Not shown here are the original grayscale images of the reconstructed amplitude and phase of each of these four QPIs; these grayscale images contain significantly little contrast when compared with the color coded images shown in Fig. 7.4. One of the most significant features in these images is the color coding of the background, which contains small values of local spatial frequency/ray angle. This enables the sample features to be more easily visualized.

7.4.2 Color coding different spatial frequencies and edge boundaries within cells

In this subsection, some additional properties of the color staining algorithm are briefly investigated. The first of these is the ability to color-code and filter different spatial frequencies within a QPI. Fig. 7.5 (a) the color filter is similar to that used in Fig. 7.3 (c) for the case of a different diatom cell recorded using the same MO. The filter is circularly symmetrical with a red center of radius of 40 surrounded by a green annulus that encompasses the full spatial frequency support of the QPI. Once again, the background area, which corresponds to low values of spatial frequency/ray angle, is colored in red, while higher local frequencies are colored in green. In Fig. 7.5 (b) a different filter is used; this time a central blue disc of radius 40 samples is used,

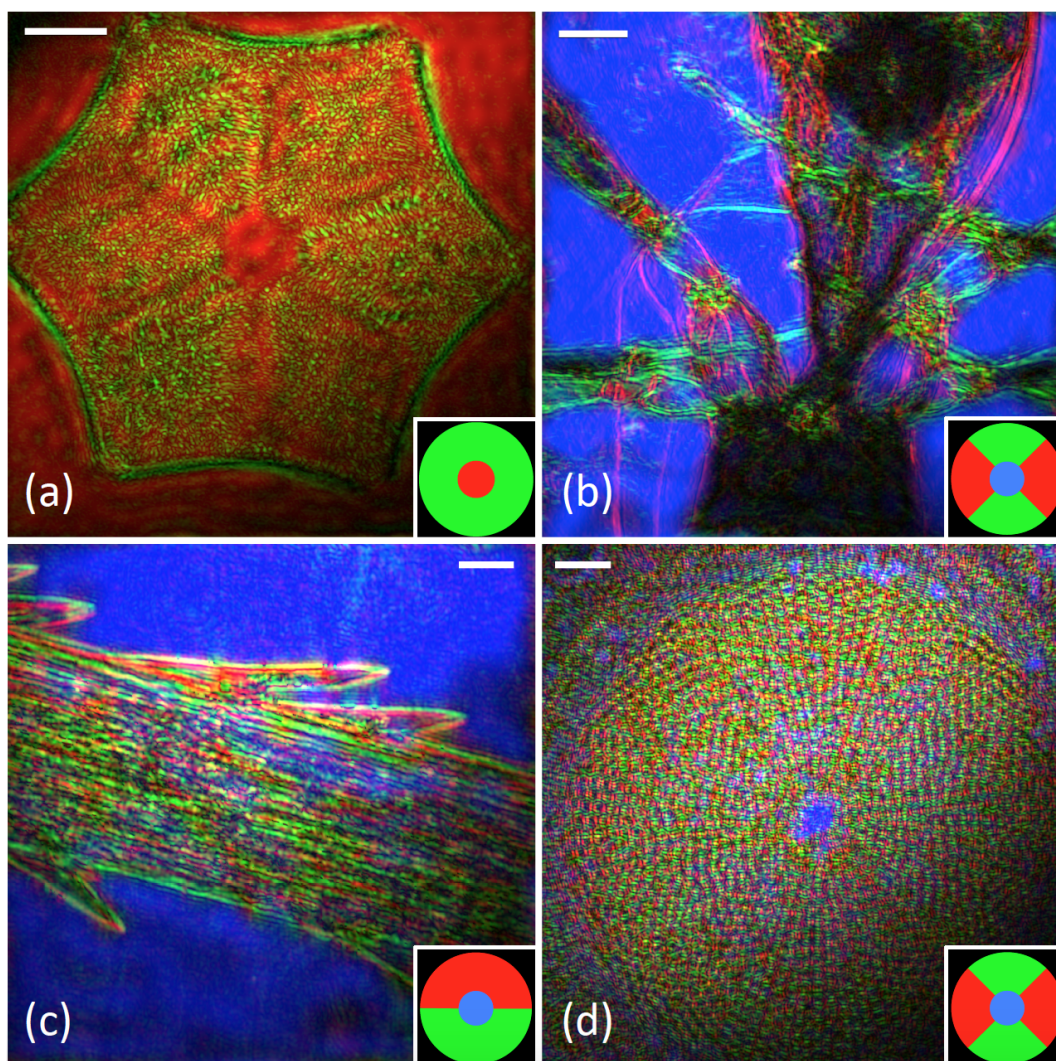


Fig. 7.4 Results for QPIs of a variety of different biological samples; (a) is a diatom recorded using a $63 \times 1.3NA$ MO (resolution bar is $5\mu m$); (b) an insect recorded using a $2.5 \times 0.08NA$ (resolution bar is $100\mu m$); (c) a barley awn recorded using a $10 \times 0.3NA$ MO (resolution bar is $20\mu m$) and (d) a diatom cell recorded using a $20 \times 0.4NA$ MO (resolution bar is $10\mu m$). The color filters used in each case are illustrated in the bottom corner of the image. For cases (a) and (d) the inner circle in the filter has a radius of 40 samples and the outer circle has a radius of 150 samples. For cases (b) and (c) the inner circle in the filter has a radius of 20 samples and the outer circle has a radius of 150 samples.

around which the surrounding annulus is split into four quadrants. The left and right quadrants are red and the top and bottom are green. Therefore, rather than consider local spatial frequencies relating only to ray angles, all vertical spatial frequencies, and all horizontal spatial frequencies, beyond some lower frequency limit will be coded in red and green respectively. This diatom cell contains a subcellular feature that modulates in the horizontal direction and it is clear that this feature is stained in red color. The boundaries of the cell, which are primarily oriented up and down in the vertical direction are coded in green. The end result is an aesthetically pleasing image in which various cellular features are color stained differently and are clearly distinguishable on a blue background. In Fig. 7.5 (c) a filter is applied that eliminates

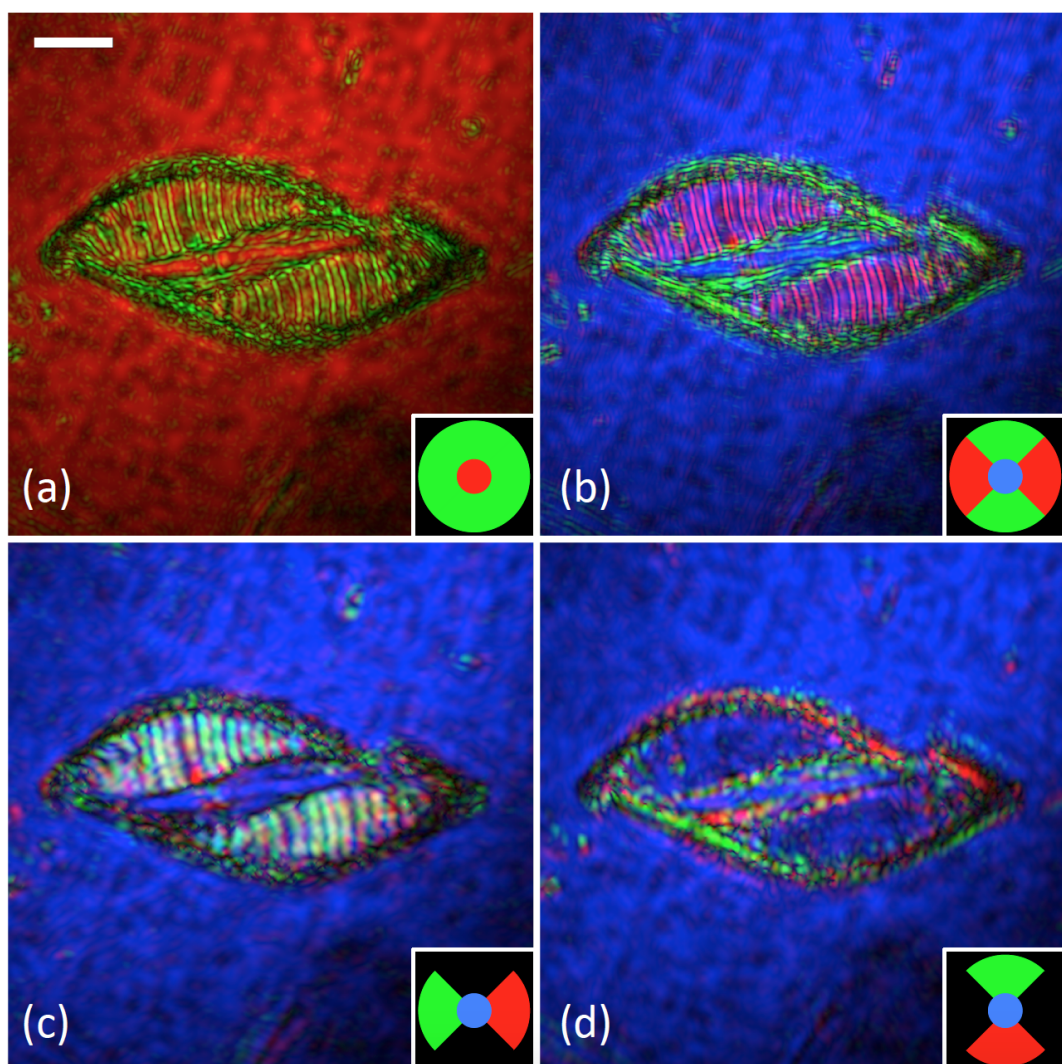


Fig. 7.5 Results for a QPI of a diatom sample containing a prominent spatial frequency; (a)-(d) show the result of four different color filters applied to the QPI is a diatom recorded using a $20 \times 0.4NA$ MO (resolution bar is $10\mu m$); The color filters used in each case are illustrated in the bottom corner of the image. For cases (a) and (d) the inner circle in the filter has a radius of 40 samples and the outer circle has a radius of 150 samples, which extends over the full support of the DFT.

positive and negative spatial frequencies in the y -direction and color codes the positive and negative spatial frequencies in the x -direction in different colors. In this case it can be seen that the edges of the cell vanish since these are related primarily to edges that are oriented in the y -direction. In contrast, in Fig. 7.5 (d) the filter blocks spatial frequencies in the x -direction causing in the central features of the cell to vanish and leaving only the cell boundary.

A final set of results are shown in Fig. 7.6, the goal of which is to demonstrate the capability of the color staining algorithm to highlight in color the boundaries between subcellular features in the QPI or the edges of larger structures in microorganisms. Details regarding the size and shape of the filters are found in the figure and the figure caption. The sample shown in Fig. 7.6 (a)-(d) is a diatom cell recorded using a $63 \times / 1.3$ MO. The first filter, a red disc inside a green annulus, is similar to that used in previous examples and it can be seen that the boundaries of the various subcellular features, which refract the geometrical ray at high angles, are colored in green, while lower local spatial frequencies are coded in red. The second filter in Fig. 7.6 (b) is made up of a blue disc around which the upper half of the annulus is red and lower half is green. For this case it can be seen that the boundaries of the subcellular features that refract the rays in the positive y -direction are coded in red, while the rays in the opposite direction are green. In Fig. 7.6 (c) encodes local frequencies in the x -direction in green and local frequencies in y -direction in red. The result is that vertical boundaries are encoded in red and vertical boundaries are green. In Fig. 7.6 (d) the horizontal boundaries are filtered out by removing the filter in the upper and lower quadrants. Fig. 7.6 (e)-(h) show the result of applying the same set of filters to an insect legs using a $10 \times / 0.3$ MO. Once again different boundaries within the microscopic object can be more clearly visualized using these various filters.

7.5 Conclusion

In this chapter, a novel algorithm has been presented that enables label free color staining to be applied to quantitative phase images recorded from biological cells and microorganisms. By tailoring the color filter that is used in the algorithm it is possible to color stain various subcellular features in the image. In Section 7.2 an optical analogue is also outlined that facilitates in understanding the implementation and behavior of the proposed algorithm in the context of coherent optical processing.

In Section 7.3, the results of the algorithm are interpreted in terms of the local spatial frequencies in the image, which are closely related to the concept of a geometrical ray angle that has been refracted from a point in the sample. To assist in this interpretation, the concept of local spatial frequency is theoretically developed for the case of a microlens array. Following this theoretical analysis, the quantitative phase image of a microlens array is shown, which is recorded using a digital holographic microscope. The initial results of color-coding this image using the proposed

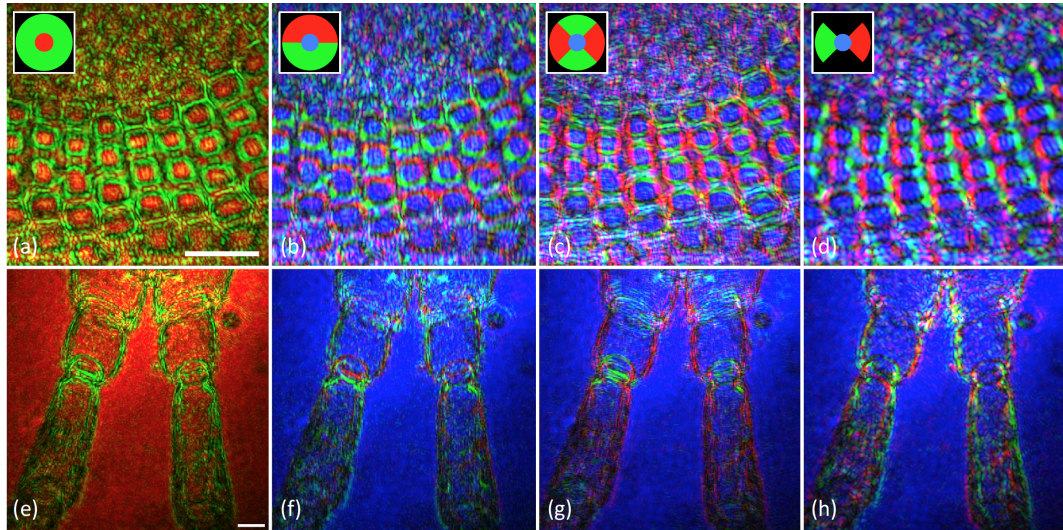


Fig. 7.6 Results of color staining applied to two QPIs of part of a diatom cell recorded using a $63 \times / 1.3$ MO (a)-(d) (resolution bar is $10 \mu m$) and the legs of an insect recorded using a $10 \times / 0.3$ MO (e)-(h) (resolution bar is $20 \mu m$). The color filters used in each column are illustrated in the top corner of each image in the first row. For cases (a)-(d) the inner circle in the filter has a radius of 40 samples and the outer circle has a radius of 150 samples, which extends over the full support of the DFT. For cases (e)-(h) the inner circle in the filter has a radius of 20 samples and the outer circle has a radius of 150 samples, which also extends over the full support of the DFT.

algorithm are also shown for a variety of filters, and these color images can easily be explained using the theoretical description of local spatial frequency. In particular it is possible to interpret how particular colors within the image are related to a solid angle of geometrical ray directions having been refracted by the phase delay of the sample.

It is noted in Section 7.3 that only the phasor part of the QPI is necessary for color coding since it is this part of the complex image that contains local spatial frequencies that relate to geometrical ray angle. By normalizing the amplitude it is shown that detail that appears in the intensity of the QPI can be eliminated, leaving only the color information relating to local spatial frequency. Although this idea will no doubt be the subject of future work, it is only considered in this chapter for the microlens array; all of the remaining QPIs that are tested throughout Section 7.4 make use of the full complex amplitude. Part of the discussion on interpretation using the microlens array also relates to the use of 2D soft edge filters such as the Butterworth or Chebyshev filters in order to eliminate or reduce unwanted effects that appear in the color image, which result from the use of hard-edged binary color filters in the DFT domain. It is demonstrated that the effect of Gibb's phenomenon can be significantly reduced by using a 2D Butterworth filter. Once again, we expect that this idea will be the subject of future work; however, it is only considered in this

chapter for the microlens array; all of the remaining QPIs that are tested throughout Section 7.4 make use of the simple case of hard-edged binary color filters.

All of the QPIs that are processed in this chapter are recorded using digital holographic microscopy. However, the algorithm can be extended to any quantitative phase imaging technique and we expect in due course that the proposed algorithm will be applied using the spatial light interference microscopy technique, the transport of intensity technique, differential phase contrast, as well as lensless microscopy, all of which are briefly discussed in the introduction.

An important point for discussion is the difference between the algorithm proposed in this chapter, and that proposed in the previous chapter. Both algorithms take as input a quantitative phase image and both algorithms produce a label-free color stained image that in some way relates to spatial frequency content. Firstly, it should be pointed out that the work in the previous chapter was based on simulating a process known as ‘optical staining’ or more commonly referred to as Rheinberg illumination. Rheinberg illumination provides a form of label-free optical staining by introducing a multi-color filter into the condenser plane of the microscope and can stain objects depending on their spatial frequency content. In the previous chapter we developed a theory for Rheinberg illumination that formed the basis of a computer algorithm that could color code a QPI. Although the colors in the image could in some way be interpreted as relating to different spatial frequency content in the image, it was not possible to define this relationship in a simple way. The algorithm proposed in this chapter is simpler in design (requires a maximum of four discrete Fourier transform operations) and in its interpretation. Unlike the previous algorithm, however, it cannot be used to reduce the spatial coherence in the image. We expect the algorithm proposed in this chapter to become a useful tool in the quantitative phase imaging community.

We finish this chapter with a similar comment that appeared at the end of the last one; a key application of any label-free color staining algorithm is to color code the nucleus of an epithelial cell. Staining the nucleus is usually achieved chemically and is a necessary step in many clinical histopathological processes. It is not yet clear if the proposed algorithm in these two chapters can successfully stain the nucleus of a cell recorded using quantitative phase imaging but we expect that this will be an active area of future research.

Chapter 8

Conclusion

8.1 Summary of Thesis Achievements

The aim of this chapter is to summarize various contributions that are contained in this thesis. The primary objective of this work is to develop methods that allow us to explore the cellular morphology of unstained biological samples, which are essentially invisible in ordinary bright-field microscopy. All of the contributions relate to quantitative phase imaging techniques, with a key emphasis on the digital holographic microscopy.

It should be noted that the last two chapters, which describe methods for label free color staining of quantitative phase images are applicable to any method of quantitative phase imaging, including lensless microscopy and the various white light techniques that are reviewed in Section 2.8 and 2.9 earlier in the thesis.

This thesis includes five key contributions, each of which are described in one chapter. The first two contributions presented in Chapter 3 and 4 relate to novel optical systems that enable the recording of images using the principles of digital holographic microscopy. Chapter 5 provides a thorough analysis of autofocus algorithms that can be applied to the recorded holograms in order to find the correct focus distance and Chapters 6 and 7 describe image processing techniques that can be applied to the in-focus reconstructed image for the purpose of label-free color staining.

In Chapter 3 a low-cost compact portable module is proposed that can be easily integrated with any existing brightfield microscope in order to record quantitative phase images. The proposed module has several advantages over the traditional off-axis architecture for digital holographic microscopy. Firstly, it is inexpensive since it is simply a low-cost add-on to an existing imaging system. Secondly, the system is greatly simple; by not requiring an additional reference wavefield to be generated by the laser, rather, the image at the output port of the microscope is split into two parts and a pinhole is used in one path to generate the reference. Thirdly, the method provides for a simple method to change the off-axis angle in order to suit

the bandwidth of any camera. Fourthly the method is extremely resilient to vibration and fifthly, because of the common path architecture, changing the sample or MO does not necessitate re aligning the reference in order to account for a path length change.

In Chapter 4 a second novel off-axis DHM system is proposed that has the capability to provide for continuously variable magnification over a range of values from approximately two times up to infinity, by simply moving the position of the sample. The new architecture is partly motivated by Gabor's original system. We used the ray transfer matrix for the system in order to derive the relationship in order to define the numerical aperture of the system for each sample position and magnification and experimental results were provided using a microlens array. We hope that this architecture may in time come to challenge the de facto standard of the past one hundred years which is to swap the microscope objective in order to change the magnification, an approach that is limited to a small discrete number of magnifications and numerical apertures. However, in order for this to happen, it will be necessary to improve on the aberration compensation methods used in the chapter. Significant aberrations are presented due to imaging with the microscope objective at a plane that is far away from the traditional imaging plane.

Chapter 5 is the first of three chapters that deal with numerical methods for the reconstruction of images recorded using digital holographic microscopy. This chapter examines the potential for sparsity metrics to be used for autofocus in digital holographic microscopy. An important result is the discovery that the 32 sparsity metrics investigated in the chapter can be grouped according to similar behavior following high pass filtering. This conclusion is based on evaluating the metrics across a broad range of holograms of diatom cells. We believe that the methodology proposed here for the evaluation and grouping may be applicable to all autofocus metrics and should be the subject of future research. Another important conclusion from this work is that following high pass filtering, the variance of the intensity, perhaps the most commonly used autofocus metric produces almost identical results to the best performing sparsity metrics that were investigated here, in terms of accuracy and reliability. Taking into account the simplicity of the variance metric in terms of computation, we conclude that this may be the metric of choice for DHM.

Chapter 6 is the first of two chapters that develop new image processing techniques for label-free color staining of subcellular features. The first method is based on simulated Rheinberg illumination. A key requirement of the algorithm is the availability of the complex transmittance of the sample, which can be provided by digital holographic microscopy (which was used to record the images that were processed in Chapter 2) or some other form of quantitative phase imaging including white light techniques such as spatial light interference microscopy or methods based on differential phase contrast or transport of intensity. In the chapter, the complete

theory of Rheinberg illumination is derived, from which an algorithm is proposed that can be digitally simulated.

Chapter 7 describes a second label free color staining algorithm. In this case the algorithm is simpler and more efficient in design than that presented in the previous chapter. Once again this algorithm takes as input the quantitative phase image, and produces a color image in which subcellular features are clearly highlighted. The approach is interpreted in terms of the concept of local spatial frequency and results are presented using a microlens array as well as a range of diatom cells.

8.2 Future Work

I would also like to add that with more time, this project could have been developed further to include:

(i) The results presented in Chapter 5 are based on the investigation of a broad range of diatom cells. These cells are unique in terms of high refractive index and more work is needed to confirm the findings herein for more commonly investigated cytological samples, such as epithelial cells and erythrocytes;

(ii) the numerical compensation of optical aberrations, which are an unwanted side-effect of variable magnification, require further attention;

(iii) a software system is under construction using the Java programming language, based on an ImageJ plugin, which will implement the algorithms discussed in this thesis. Together with the Micromanager software package this will provide an easy to use graphical user interface(GUI), once complete. Parallel computation on GPUs will be utilised for real-time implementation of the more intensive image processing components;

(iv) the classification of a range of different epithelial cells by creating a continuous 3D morphology with nanometer accuracy and extracting key morphological features, such as the total cell volume or nucleus to cytoplasm ratio.

References

- [1] J. W. Goodman, *Introduction to Fourier optics*. Roberts and Company Publishers, 2005.
- [2] N. Hurley and S. Rickard, “Comparing measures of sparsity,” *Information theory, IEEE Transactions on*, vol. 55, no. 10, pp. 4723–4741, 2009.
- [3] A. Ruthmann, “Methods in cell research,” 1970.
- [4] K. Uluç, G. C. Kujoth, and M. K. Başkaya, “Operating microscopes: past, present, and future,” *Neurosurgical focus*, vol. 27, no. 3, p. E4, 2009.
- [5] F. Zernike, “Phase contrast, a new method for the microscopic observation of transparent objects,” *Physica*, vol. 9, no. 7, pp. 686–698, 1942.
- [6] P. Marquet, B. Rappaz, P. J. Magistretti, E. Cuche, Y. Emery, T. Colomb, and C. Depeursinge, “Digital holographic microscopy: a noninvasive contrast imaging technique allowing quantitative visualization of living cells with subwavelength axial accuracy,” *Optics letters*, vol. 30, no. 5, pp. 468–470, 2005.
- [7] B. Rappaz, P. Marquet, E. Cuche, Y. Emery, C. Depeursinge, and P. J. Magistretti, “Measurement of the integral refractive index and dynamic cell morphometry of living cells with digital holographic microscopy,” *Optics express*, vol. 13, no. 23, pp. 9361–9373, 2005.
- [8] B. Kemper and G. von Bally, “Digital holographic microscopy for live cell applications and technical inspection,” *Applied optics*, vol. 47, no. 4, pp. A52–A61, 2008.
- [9] D. Carl, B. Kemper, G. Wernicke, and G. von Bally, “Parameter-optimized digital holographic microscope for high-resolution living-cell analysis,” *Applied optics*, vol. 43, no. 36, pp. 6536–6544, 2004.
- [10] P. Langehanenberg, B. Kemper, D. Dirksen, and G. Von Bally, “Autofocusing in digital holographic phase contrast microscopy on pure phase objects for live cell imaging,” *Applied optics*, vol. 47, no. 19, pp. D176–D182, 2008.
- [11] P. Langehanenberg, L. Ivanova, I. Bernhardt, S. Ketelhut, A. Vollmer, D. Dirksen, G. Georgiev, G. von Bally, and B. Kemper, “Automated three-dimensional tracking of living cells by digital holographic microscopy,” *Journal of biomedical optics*, vol. 14, no. 1, pp. 014018–014018, 2009.
- [12] F. Charrière, A. Marian, F. Montfort, J. Kuehn, T. Colomb, E. Cuche, P. Marquet, and C. Depeursinge, “Cell refractive index tomography by digital holographic microscopy,” *Optics letters*, vol. 31, no. 2, pp. 178–180, 2006.
- [13] D. Gabor, “A new microscopic principle,” 1948.

- [14] E. N. Leith and J. Upatnieks, "Reconstructed wavefronts and communication theory," *JOSA*, vol. 52, no. 10, pp. 1123–1130, 1962.
- [15] J. W. Goodman and R. Lawrence, "Digital image formation from electronically detected holograms," *Applied physics letters*, vol. 11, no. 3, pp. 77–79, 1967.
- [16] M. Kronrod, N. Merzlyakov, and L. Yaroslavskii, "Reconstruction of a hologram with a computer," *Soviet Physics Technical Physics*, vol. 17, p. 333, 1972.
- [17] U. Schnars, T. M. Kreis, and W. P. Jüptner, "Digital recording and numerical reconstruction of holograms: reduction of the spatial frequency spectrum," *Optical Engineering*, vol. 35, no. 4, pp. 977–983, 1996.
- [18] E. CuChe, P. Marquet, and C. Depeursinge, "Spatial filtering for zero-order and twin-image elimination in digital off-axis holography," *Applied optics*, vol. 39, no. 23, pp. 4070–4075, 2000.
- [19] I. Yamaguchi and T. Zhang, "Phase-shifting digital holography," *Optics letters*, vol. 22, no. 16, pp. 1268–1270, 1997.
- [20] T. Colomb, E. CuChe, F. Charrière, J. Kühn, N. Aspert, F. Montfort, P. Marquet, and C. Depeursinge, "Automatic procedure for aberration compensation in digital holographic microscopy and applications to specimen shape compensation," *Applied optics*, vol. 45, no. 5, pp. 851–863, 2006.
- [21] B. Kemper, S. Kosmeier, P. Langehanenberg, G. von Bally, I. Bredebusch, W. Domschke, and J. Schnekenburger, "Integral refractive index determination of living suspension cells by multifocus digital holographic phase contrast microscopy," *Journal of biomedical optics*, vol. 12, no. 5, p. 054009, 2007.
- [22] B. Kemper, A. Vollmer, G. von Bally, C. E. Rommel, and J. Schnekenburger, "Simplified approach for quantitative digital holographic phase contrast imaging of living cells," *Journal of biomedical optics*, vol. 16, no. 2, p. 026014, 2011.
- [23] M.-K. Kim, "Applications of digital holography in biomedical microscopy," *Journal of the Optical Society of Korea*, vol. 14, no. 2, pp. 77–89, 2010.
- [24] C. J. Mann, L. Yu, C.-M. Lo, and M. K. Kim, "High-resolution quantitative phase-contrast microscopy by digital holography," *Optics Express*, vol. 13, no. 22, pp. 8693–8698, 2005.
- [25] L. Yu, S. Mohanty, J. Zhang, S. Genc, M. K. Kim, M. W. Berns, and Z. Chen, "Digital holographic microscopy for quantitative cell dynamic evaluation during laser microsurgery," *Optics Express*, vol. 17, no. 14, pp. 12031–12038, 2009.
- [26] X. Yu, M. Cross, C. Liu, D. C. Clark, D. T. Haynie, and M. K. Kim, "Measurement of the traction force of biological cells by digital holography," *Biomedical optics express*, vol. 3, no. 1, pp. 153–159, 2012.
- [27] P. Ferraro, D. Alferi, S. De Nicola, L. De Petrocellis, A. Finizio, and G. Pierattini, "Quantitative phase-contrast microscopy by a lateral shear approach to digital holographic image reconstruction," *Optics letters*, vol. 31, no. 10, pp. 1405–1407, 2006.

- [28] L. Miccio, S. Grilli, A. Finizio, S. De Nicola, L. De Petrocellis, and P. Ferraro, "Lipid particle detection by means digital holography and lateral shear interferometry," in *European Conference on Biomedical Optics*, p. 6631_16, Optical Society of America, 2007.
- [29] F. Merola, L. Miccio, M. Paturzo, A. Finizio, S. Grilli, and P. Ferraro, "Driving and analysis of micro-objects by digital holographic microscope in microfluidics," *Optics letters*, vol. 36, no. 16, pp. 3079–3081, 2011.
- [30] I. Moon, M. Daneshpanah, B. Javidi, and A. Stern, "Automated three-dimensional identification and tracking of micro/nanobiological organisms by computational holographic microscopy," *Proceedings of the IEEE*, vol. 97, no. 6, pp. 990–1010, 2009.
- [31] T. Nomura and B. Javidi, "Object recognition by use of polarimetric phase-shifting digital holography," *Optics letters*, vol. 32, no. 15, pp. 2146–2148, 2007.
- [32] R. Liu, D. K. Dey, D. Boss, P. Marquet, and B. Javidi, "Recognition and classification of red blood cells using digital holographic microscopy and data clustering with discriminant analysis," *JOSA A*, vol. 28, no. 6, pp. 1204–1210, 2011.
- [33] D. L. Donoho, "Compressed sensing," *Information Theory, IEEE Transactions on*, vol. 52, no. 4, pp. 1289–1306, 2006.
- [34] E. J. Candès and M. B. Wakin, "An introduction to compressive sampling," *Signal Processing Magazine, IEEE*, vol. 25, no. 2, pp. 21–30, 2008.
- [35] P. Bofill and M. Zibulevsky, "Underdetermined blind source separation using sparse representations," *Signal processing*, vol. 81, no. 11, pp. 2353–2362, 2001.
- [36] A. Cichocki, S. Amari, *et al.*, "Analysis of sparse representation and blind source separation," *Neural computation*, vol. 16, no. 6, pp. 1193–1234, 2004.
- [37] J. Goodman, "Introduction to fourier optics," 2008.
- [38] R. Bracewell, "The Fourier transform and its applications," *New York*, vol. 5, 1965.
- [39] A. Sommerfeld, "Optics lectures on theoretical physics, vol. iv," *Optics Lectures on Theoretical Physics, Vol. IV by Arnold Sommerfeld New York, NY: Academic Press INC, 1954*, vol. 4, 1954.
- [40] J. C. Maxwell, "Xxv. on physical lines of force: Part i.—the theory of molecular vortices applied to magnetic phenomena," *The London, Edinburgh, and Dublin Philosophical Magazine and Journal of Science*, vol. 21, no. 139, pp. 161–175, 1861.
- [41] S. A. Collins, "Lens-system diffraction integral written in terms of matrix optics," *JOSA*, vol. 60, no. 9, pp. 1168–1177, 1970.
- [42] B. M. Hennelly and J. T. Sheridan, "Generalizing, optimizing, and inventing numerical algorithms for the fractional Fourier, Fresnel, and linear canonical transforms," *JOSA A*, vol. 22, no. 5, pp. 917–927, 2005.

- [43] J. T. Sheridan, B. Hennelly, and D. Kelly, "Motion detection, the wigner distribution function, and the optical fractional fourier transform," *Optics letters*, vol. 28, no. 11, pp. 884–886, 2003.
- [44] D. P. Kelly, B. M. Hennelly, W. T. Rhodes, and J. T. Sheridan, "Analytical and numerical analysis of linear optical systems," *Optical Engineering*, vol. 45, no. 8, p. 088201, 2006.
- [45] M. Pluta and P. Maksymilian, *Advanced light microscopy*, vol. 1. Elsevier Amsterdam, 1988.
- [46] D. B. Murphy, *Fundamentals of light microscopy and electronic imaging*. John Wiley & Sons, 2002.
- [47] C. Burch and J. Stock, "Phase-contrast microscopy," *Journal of Scientific Instruments*, vol. 19, no. 5, p. 71, 1942.
- [48] F. Zernike, "How i discovered phase contrast," *Science*, vol. 121, no. 3141, pp. 345–349, 1955.
- [49] R. Allen and G. David, "The zeiss-nomarski differential interference equipment for transmitted-light microscopy," *Zeitschrift fur wissenschaftliche Mikroskopie und mikroskopische Technik*, vol. 69, no. 4, pp. 193–221, 1969.
- [50] W. Lang, *Nomarski differential interference-contrast microscopy*. Carl Zeiss, 1982.
- [51] D. Murphy and M. Davidson, "Differential interference contrast (dic) microscopy and modulation contrast microscopy," *Fundamentals of light microscopy and digital imaging*, pp. 153–168, 2001.
- [52] J. W. Lichtman and J.-A. Conchello, "Fluorescence microscopy," *Nature methods*, vol. 2, no. 12, p. 910, 2005.
- [53] E. Harlow, D. Lane, *et al.*, "A laboratory manual," *New York: Cold Spring Harbor Laboratory*, vol. 579, 1988.
- [54] J. Rheinberg, "On an addition to the methods of microscopical research, by a new way optically producing color-contrast between an object and its background, or between definite parts of the object itself," *JR Microsc. Soc.*, vol. 16, pp. 373–388, 1896.
- [55] E. C. Samson and C. M. Blanca, "Dynamic contrast enhancement in widefield microscopy using projector-generated illumination patterns," *New Journal of Physics*, vol. 9, no. 10, p. 363, 2007.
- [56] K. F. Webb, "Condenser-free contrast methods for transmitted-light microscopy," *Journal of microscopy*, vol. 257, no. 1, pp. 8–22, 2015.
- [57] C. Zuo, J. Sun, S. Feng, Y. Hu, and Q. Chen, "Programmable colored illumination microscopy (pcim): A practical and flexible optical staining approach for microscopic contrast enhancement," *Optics and Lasers in Engineering*, vol. 78, pp. 35–47, 2016.
- [58] M. Mir, B. Bhaduri, R. Wang, R. Zhu, and G. Popescu, "Quantitative phase imaging," *Progress in Optics*, vol. 57, pp. 133–217, 2012.

- [59] K. Lee, K. Kim, J. Jung, J. Heo, S. Cho, S. Lee, G. Chang, Y. Jo, H. Park, and Y. Park, "Quantitative phase imaging techniques for the study of cell pathophysiology: from principles to applications," *Sensors*, vol. 13, no. 4, pp. 4170–4191, 2013.
- [60] G. Coppola, P. Ferraro, M. Iodice, S. De Nicola, A. Finizio, and S. Grilli, "A digital holographic microscope for complete characterization of microelectromechanical systems," *Measurement Science and Technology*, vol. 15, no. 3, p. 529, 2004.
- [61] Y. Fu, G. Pedrini, B. M. Hennelly, R. M. Groves, and W. Osten, "Dual-wavelength image-plane digital holography for dynamic measurement," *Optics and Lasers in Engineering*, vol. 47, no. 5, pp. 552–557, 2009.
- [62] F. Charrière, J. Kühn, T. Colomb, F. Montfort, E. Cuhe, Y. Emery, K. Weible, P. Marquet, and C. Depeursinge, "Characterization of microlenses by digital holographic microscopy," *Applied optics*, vol. 45, no. 5, pp. 829–835, 2006.
- [63] B. M. Hennelly, D. P. Kelly, N. Pandey, and D. S. Monaghan, "Review of twin reduction and twin removal techniques in holography," 2009.
- [64] B. M. Hennelly, D. P. Kelly, D. S. Monaghan, and N. Pandey, "Zoom algorithms for digital holography," in *Information Optics and Photonics*, pp. 187–204, Springer, 2010.
- [65] D. Kelly, B. Hennelly, C. McElhinney, and T. Naughton, "A practical guide to digital holography and generalized sampling," in *Optical Engineering+ Applications*, pp. 707215–707215, International Society for Optics and Photonics, 2008.
- [66] D. P. Kelly, B. M. Hennelly, N. Pandey, T. J. Naughton, and W. T. Rhodes, "Resolution limits in practical digital holographic systems," *Optical engineering*, vol. 48, no. 9, pp. 095801–095801, 2009.
- [67] M. D. Pritt and D. C. Ghiglia, *Two-dimensional phase unwrapping: theory, algorithms, and software*. Wiley, 1998.
- [68] M. A. Herráez, D. R. Burton, M. J. Lalor, and M. A. Gdeisat, "Fast two-dimensional phase-unwrapping algorithm based on sorting by reliability following a noncontinuous path," *Applied optics*, vol. 41, no. 35, pp. 7437–7444, 2002.
- [69] L. Aiello, D. Riccio, P. Ferraro, S. Grilli, L. Sansone, G. Coppola, S. De Nicola, and A. Finizio, "Green's formulation for robust phase unwrapping in digital holography," *Optics and lasers in engineering*, vol. 45, no. 6, pp. 750–755, 2007.
- [70] D. C. Ghiglia and L. A. Romero, "Minimum lp-norm two-dimensional phase unwrapping," *JOSA A*, vol. 13, no. 10, pp. 1999–2013, 1996.
- [71] W. Xu and I. Cumming, "A region-growing algorithm for insar phase unwrapping," *IEEE Transactions on Geoscience and Remote Sensing*, vol. 37, no. 1, pp. 124–134, 1999.
- [72] R. Bamler and P. Hartl, "Synthetic aperture radar interferometry," *Inverse problems*, vol. 14, no. 4, p. R1, 1998.
- [73] L. Axel and D. Morton, "Correction of phase wrapping in magnetic resonance imaging," *Medical physics*, vol. 16, no. 2, pp. 284–287, 1989.

- [74] T. Kreis, "Digital holographic interference-phase measurement using the fourier-transform method," *JOSA A*, vol. 3, no. 6, pp. 847–855, 1986.
- [75] D. C. Ghiglia and L. A. Romero, "Robust two-dimensional weighted and unweighted phase unwrapping that uses fast transforms and iterative methods," *JOSA A*, vol. 11, no. 1, pp. 107–117, 1994.
- [76] A. Pepe and R. Lanari, "On the extension of the minimum cost flow algorithm for phase unwrapping of multitemporal differential sar interferograms," *IEEE Transactions on Geoscience and remote sensing*, vol. 44, no. 9, pp. 2374–2383, 2006.
- [77] L. Ma, H. Wang, Y. Li, and H. Jin, "Numerical reconstruction of digital holograms for three-dimensional shape measurement," *Journal of optics A: Pure and applied optics*, vol. 6, no. 4, p. 396, 2004.
- [78] M. L. Tachiki, M. Itoh, and T. Yatagai, "Simultaneous depth determination of multiple objects by focus analysis in digital holography," *Applied optics*, vol. 47, no. 19, pp. D144–D153, 2008.
- [79] M. Liebling and M. Unser, "Autofocus for digital Fresnel holograms by use of a Fresnelet-sparsity criterion," *JOSA A*, vol. 21, no. 12, pp. 2424–2430, 2004.
- [80] W. Li, N. C. Loomis, Q. Hu, and C. S. Davis, "Focus detection from digital in-line holograms based on spectral ℓ_1 norms," *JOSA A*, vol. 24, no. 10, pp. 3054–3062, 2007.
- [81] S. Lee, J. Y. Lee, W. Yang, and D. Y. Kim, "Autofocusing and edge detection schemes in cell volume measurements with quantitative phase microscopy," *Optics express*, vol. 17, no. 8, pp. 6476–6486, 2009.
- [82] M. F. Toy, S. Richard, J. Kühn, A. Franco-Obregón, M. Egli, and C. Depeursinge, "Enhanced robustness digital holographic microscopy for demanding environment of space biology," *Biomedical optics express*, vol. 3, no. 2, pp. 313–326, 2012.
- [83] F. Dubois, C. Schockaert, N. Callens, and C. Yourassowsky, "Focus plane detection criteria in digital holography microscopy by amplitude analysis," *Optics express*, vol. 14, no. 13, pp. 5895–5908, 2006.
- [84] P. Langehanenberg, G. von Bally, and B. Kemper, "Autofocusing in digital holographic microscopy," *3D Research*, vol. 2, no. 1, pp. 1–11, 2011.
- [85] Y. Yang, B. Kang, and Y. Choo, "Application of the correlation coefficient method for determination of the focal plane to digital particle holography," *Applied optics*, vol. 47, no. 6, pp. 817–824, 2008.
- [86] P. Memmolo, C. Distanto, M. Paturzo, A. Finizio, P. Ferraro, and B. Javidi, "Automatic focusing in digital holography and its application to stretched holograms," *Optics letters*, vol. 36, no. 10, pp. 1945–1947, 2011.
- [87] V. Dyomin and D. Kamenev, "A comparison of methods for evaluating the location of the best focusing planes of particle images reconstructed from digital holograms," *Russian physics journal*, vol. 56, no. 7, pp. 822–830, 2013.
- [88] C. A. Trujillo and J. GarciaSucerquia, "Automatic method for focusing biological specimens in digital lensless holographic microscopy," *Optics letters*, vol. 39, no. 9, pp. 2569–2572, 2014.

- [89] C. Trujillo and J. Garcia-Sucerquia, "Comparative analysis of the modified enclosed energy metric for self-focusing holograms from digital lensless holographic microscopy," *Applied optics*, vol. 54, no. 16, pp. 5102–5108, 2015.
- [90] J. Kostencka, T. Kozacki, and K. Lizewski, "Autofocusing method for tilted image plane detection in digital holographic microscopy," *Optics Communications*, vol. 297, pp. 20–26, 2013.
- [91] N. Dugan, J. J. Healy, J. P. Ryle, and B. M. Hennelly, "Gpu accelerated holographic microscopy for the inspection of quickly moving fluids for applications in pharmaceutical manufacturing," in *SPIE Photonics Europe*, pp. 91311A–91311A, International Society for Optics and Photonics, 2014.
- [92] M. F. Toy, J. Kühn, S. Richard, J. Parent, M. Egli, and C. Depeursinge, "Accelerated autofocusing of off-axis holograms using critical sampling," *Optics letters*, vol. 37, no. 24, pp. 5094–5096, 2012.
- [93] P. Memmolo, M. Paturzo, B. Javidi, P. A. Netti, and P. Ferraro, "Refocusing criterion via sparsity measurements in digital holography," *Optics letters*, vol. 39, no. 16, pp. 4719–4722, 2014.
- [94] X. Fan, J. Healy, and B. Hennelly, "Sparsity metrics for autofocus in digital holographic microscopy," in *SPIE Photonics Europe*, pp. 989619–989619, International Society for Optics and Photonics, 2016.
- [95] E. S. Fonseca, P. T. Fiadeiro, M. Pereira, and A. Pinheiro, "Comparative analysis of autofocus functions in digital in-line phase-shifting holography," *Applied Optics*, vol. 55, no. 27, pp. 7663–7674, 2016.
- [96] F. C. Groen, I. T. Young, and G. Ligthart, "A comparison of different focus functions for use in autofocus algorithms," *Cytometry*, vol. 6, no. 2, pp. 81–91, 1985.
- [97] P. Memmolo, L. Miccio, M. Paturzo, G. Di Caprio, G. Coppola, P. A. Netti, and P. Ferraro, "Recent advances in holographic 3d particle tracking," *Advances in Optics and Photonics*, vol. 7, no. 4, pp. 713–755, 2015.
- [98] A. Stadelmaier and J. H. Massig, "Compensation of lens aberrations in digital holography," *Optics letters*, vol. 25, no. 22, pp. 1630–1632, 2000.
- [99] S. Grilli, P. Ferraro, S. De Nicola, A. Finizio, G. Pierattini, and R. Meucci, "Whole optical wavefields reconstruction by digital holography," *Optics Express*, vol. 9, no. 6, pp. 294–302, 2001.
- [100] S. De Nicola, A. Finizio, G. Pierattini, P. Ferraro, and D. Alfieri, "Angular spectrum method with correction of anamorphism for numerical reconstruction of digital holograms on tilted planes," *Optics express*, vol. 13, no. 24, pp. 9935–9940, 2005.
- [101] E. Cuhe, P. Marquet, and C. Depeursinge, "Simultaneous amplitude-contrast and quantitative phase-contrast microscopy by numerical reconstruction of fresnel off-axis holograms," *Applied optics*, vol. 38, no. 34, pp. 6994–7001, 1999.
- [102] G. Pedrini, S. Schedin, and H. J. Tiziani, "Aberration compensation in digital holographic reconstruction of microscopic objects," *Journal of modern optics*, vol. 48, no. 6, pp. 1035–1041, 2001.

- [103] P. Ferraro, S. De Nicola, A. Finizio, G. Coppola, S. Grilli, C. Magro, and G. Pierattini, "Compensation of the inherent wave front curvature in digital holographic coherent microscopy for quantitative phase-contrast imaging," *Applied optics*, vol. 42, no. 11, pp. 1938–1946, 2003.
- [104] T. Colomb, J. Kühn, F. Charriere, C. Depeursinge, P. Marquet, and N. Aspert, "Total aberrations compensation in digital holographic microscopy with a reference conjugated hologram," *Optics express*, vol. 14, no. 10, pp. 4300–4306, 2006.
- [105] T. Colomb, F. Montfort, J. Kühn, N. Aspert, E. Cuche, A. Marian, F. Charrière, S. Bourquin, P. Marquet, and C. Depeursinge, "Numerical parametric lens for shifting, magnification, and complete aberration compensation in digital holographic microscopy," *JOSA A*, vol. 23, no. 12, pp. 3177–3190, 2006.
- [106] C. Mann and M. Kim, "Quantitative phase-contrast microscopy by angular spectrum digital holography," in *Three-Dimensional and Multidimensional Microscopy: Image Acquisition and Processing XIII*, vol. 6090, p. 60900B, International Society for Optics and Photonics, 2006.
- [107] W. Qu, C. O. Choo, V. R. Singh, Y. Yingjie, and A. Asundi, "Quasi-physical phase compensation in digital holographic microscopy," *JOSA A*, vol. 26, no. 9, pp. 2005–2011, 2009.
- [108] E. N. Leith and J. Upatnieks, "Wavefront reconstruction with diffused illumination and three-dimensional objects," *Josa*, vol. 54, no. 11, pp. 1295–1301, 1964.
- [109] T. Kreis, *Handbook of holographic interferometry: optical and digital methods*. John Wiley & Sons, 2006.
- [110] U. Schnars, C. Falldorf, J. Watson, and W. Jüptner, "Digital holography," in *Digital Holography and Wavefront Sensing*, pp. 39–68, Springer, 2015.
- [111] P. Picart and J. Leval, "General theoretical formulation of image formation in digital fresnel holography," *JOSA A*, vol. 25, no. 7, pp. 1744–1761, 2008.
- [112] G. Pedrini, P. Fröning, H. Fessler, and H. J. Tiziani, "In-line digital holographic interferometry," *Applied optics*, vol. 37, no. 26, pp. 6262–6269, 1998.
- [113] J. Garcia-Sucerquia, W. Xu, S. K. Jericho, P. Klages, M. H. Jericho, and H. J. Kreuzer, "Digital in-line holographic microscopy," *Applied optics*, vol. 45, no. 5, pp. 836–850, 2006.
- [114] J. Garcia-Sucerquia, W. Xu, M. Jericho, and H. J. Kreuzer, "Immersion digital in-line holographic microscopy," *Optics letters*, vol. 31, no. 9, pp. 1211–1213, 2006.
- [115] S. Jericho, J. Garcia-Sucerquia, W. Xu, M. Jericho, and H. Kreuzer, "Submersible digital in-line holographic microscope," *Review of scientific instruments*, vol. 77, no. 4, p. 043706, 2006.
- [116] J. Garcia-Sucerquia, "Color lensless digital holographic microscopy with micrometer resolution," *Optics letters*, vol. 37, no. 10, pp. 1724–1726, 2012.
- [117] H. J. Kreuzer, "Holographic microscope and method of hologram reconstruction," June 25 2002. US Patent 6,411,406.

- [118] K. M. Molony, B. M. Hennelly, D. P. Kelly, and T. J. Naughton, "Reconstruction algorithms applied to in-line gabor digital holographic microscopy," *Optics Communications*, vol. 283, no. 6, pp. 903–909, 2010.
- [119] T. Latychevskaia and H.-W. Fink, "Solution to the twin image problem in holography," *Physical review letters*, vol. 98, no. 23, p. 233901, 2007.
- [120] A. Greenbaum and A. Ozcan, "Maskless imaging of dense samples using pixel super-resolution based multi-height lensfree on-chip microscopy," *Optics express*, vol. 20, no. 3, pp. 3129–3143, 2012.
- [121] L. Waller, Y. Luo, S. Y. Yang, and G. Barbastathis, "Transport of intensity phase imaging in a volume holographic microscope," *Optics letters*, vol. 35, no. 17, pp. 2961–2963, 2010.
- [122] W. Luo, Y. Zhang, Z. Göröcs, A. Feizi, and A. Ozcan, "Propagation phasor approach for holographic image reconstruction," *Scientific reports*, vol. 6, p. 22738, 2016.
- [123] A. Ozcan and A. Greenbaum, "Maskless imaging of dense samples using multi-height lensfree microscope," July 25 2017. US Patent 9,715,099.
- [124] Y. Rivenson, Y. Zhang, H. Günaydın, D. Teng, and A. Ozcan, "Phase recovery and holographic image reconstruction using deep learning in neural networks," *Light: Science & Applications*, vol. 7, no. 2, p. 17141, 2018.
- [125] A. Sinha, J. Lee, S. Li, and G. Barbastathis, "Lensless computational imaging through deep learning," *Optica*, vol. 4, no. 9, pp. 1117–1125, 2017.
- [126] W. Bishara, T.-W. Su, A. F. Coskun, and A. Ozcan, "Lensfree on-chip microscopy over a wide field-of-view using pixel super-resolution," *Optics express*, vol. 18, no. 11, pp. 11181–11191, 2010.
- [127] Z. Wang, L. Millet, M. Mir, H. Ding, S. Unarunotai, J. Rogers, M. U. Gillette, and G. Popescu, "Spatial light interference microscopy (slim)," *Optics express*, vol. 19, no. 2, pp. 1016–1026, 2011.
- [128] B. Bhaduri, H. Pham, M. Mir, and G. Popescu, "Diffraction phase microscopy with white light," *Optics letters*, vol. 37, no. 6, pp. 1094–1096, 2012.
- [129] A. Barty, K. Nugent, D. Paganin, and A. Roberts, "Quantitative optical phase microscopy," *Optics Letters*, vol. 23, no. 11, pp. 817–819, 1998.
- [130] C. Zuo, J. Sun, J. Li, J. Zhang, A. Asundi, and Q. Chen, "High-resolution transport-of-intensity quantitative phase microscopy with annular illumination," *Scientific reports*, vol. 7, no. 1, p. 7654, 2017.
- [131] C. Zuo, Q. Chen, W. Qu, and A. Asundi, "High-speed transport-of-intensity phase microscopy with an electrically tunable lens," *Optics express*, vol. 21, no. 20, pp. 24060–24075, 2013.
- [132] C. Zuo, Q. Chen, W. Qu, and A. Asundi, "Noninterferometric single-shot quantitative phase microscopy," *Optics letters*, vol. 38, no. 18, pp. 3538–3541, 2013.
- [133] G. Popescu, T. Ikeda, R. R. Dasari, and M. S. Feld, "Diffraction phase microscopy for quantifying cell structure and dynamics," *Optics letters*, vol. 31, no. 6, pp. 775–777, 2006.

- [134] H. Ding and G. Popescu, “Instantaneous spatial light interference microscopy,” *Optics express*, vol. 18, no. 2, pp. 1569–1575, 2010.
- [135] J. Jang, C. Y. Bae, J.-K. Park, and J. C. Ye, “Self-reference quantitative phase microscopy for microfluidic devices,” *Optics letters*, vol. 35, no. 4, pp. 514–516, 2010.
- [136] G. Coppola, G. Di Caprio, M. Gioffré, R. Puglisi, D. Balduzzi, A. Galli, L. Miccio, M. Paturzo, S. Grilli, A. Finizio, *et al.*, “Digital self-referencing quantitative phase microscopy by wavefront folding in holographic image reconstruction,” *Optics letters*, vol. 35, no. 20, pp. 3390–3392, 2010.
- [137] V. Mico, Z. Zalevsky, and J. García, “Common-path phase-shifting digital holographic microscopy: a way to quantitative phase imaging and superresolution,” *Optics Communications*, vol. 281, no. 17, pp. 4273–4281, 2008.
- [138] P. Bon, G. Maucort, B. Wattellier, and S. Monneret, “Quadriwave lateral shearing interferometry for quantitative phase microscopy of living cells,” *Optics express*, vol. 17, no. 15, pp. 13080–13094, 2009.
- [139] N. T. Shaked, Y. Zhu, N. Badie, N. Bursac, and A. P. Wax, “Reflective interferometric chamber for quantitative phase imaging of biological sample dynamics,” *Journal of biomedical optics*, vol. 15, no. 3, p. 030503, 2010.
- [140] N. T. Shaked, “Quantitative phase microscopy of biological samples using a portable interferometer,” *Optics letters*, vol. 37, no. 11, pp. 2016–2018, 2012.
- [141] P. Girshovitz and N. T. Shaked, “Compact and portable low-coherence interferometer with off-axis geometry for quantitative phase microscopy and nanoscopy,” *Optics express*, vol. 21, no. 5, pp. 5701–5714, 2013.
- [142] A. Nativ and N. T. Shaked, “Compact interferometric module for full-field interferometric phase microscopy with low spatial coherence illumination,” *Optics letters*, vol. 42, no. 8, pp. 1492–1495, 2017.
- [143] J. W. Goodman, *Introduction to Fourier Optics*. Roberts & Company Publishers, 2004.
- [144] D. Mendlovic, Z. Zalevsky, and N. Konforti, “Computation considerations and fast algorithms for calculating the diffraction integral,” *Journal of Modern Optics*, vol. 44, no. 2, pp. 407–414, 1997.
- [145] D. Mas, J. Garcia, C. Ferreira, L. M. Bernardo, and F. Marinho, “Fast algorithms for free-space diffraction patterns calculation,” *Optics Communications*, vol. 164, no. 4-6, pp. 233–245, 1999.
- [146] K. Huang and S. Aviyente, “Sparse representation for signal classification,” in *Advances in neural information processing systems*, pp. 609–616, 2006.
- [147] J. Karvanen and A. Cichocki, “Measuring sparseness of noisy signals,” in *4th International Symposium on Independent Component Analysis and Blind Signal Separation*, pp. 125–130, 2003.
- [148] C. Gini, “Measurement of inequality of incomes,” *The economic journal*, vol. 31, no. 121, pp. 124–126, 1921.
- [149] H. Shalit and S. Yitzhaki, “The mean-Gini efficient portfolio frontier,” *Journal of financial research*, vol. 28, no. 1, pp. 59–75, 2005.

- [150] R. Aaberge, “Axiomatic characterization of the Gini coefficient and Lorenz curve orderings,” *Journal of economic theory*, vol. 101, no. 1, pp. 115–132, 2001.
- [151] M. O. Lorenz, “Methods of measuring the concentration of wealth,” *Publications of the American statistical association*, vol. 9, no. 70, pp. 209–219, 1905.
- [152] S. Rickard and M. Fallon, “The Gini index of speech,” in *Proceedings of the 38th Conference on Information Science and Systems (CISS04)*, 2004.
- [153] D. Zonoobi, A. A. Kassim, and Y. V. Venkatesh, “Gini index as sparsity measure for signal reconstruction from compressive samples,” *Selected Topics in Signal Processing, IEEE Journal of*, vol. 5, no. 5, pp. 927–932, 2011.
- [154] P. Ferraro, S. Grilli, D. Alfieri, S. De Nicola, A. Finizio, G. Pierattini, B. Javidi, G. Coppola, and V. Striano, “Extended focused image in microscopy by digital holography,” *Optics express*, vol. 13, no. 18, pp. 6738–6749, 2005.
- [155] A. Savitzky and M. J. Golay, “Smoothing and differentiation of data by simplified least squares procedures.,” *Analytical chemistry*, vol. 36, no. 8, pp. 1627–1639, 1964.
- [156] M. Born and E. Wolf, *Principles of optics: electromagnetic theory of propagation, interference and diffraction of light*. Elsevier, 2013.
- [157] H. H. Hopkins, “On the diffraction theory of optical images,” *Proc. R. Soc. Lond. A*, vol. 217, no. 1130, pp. 408–432, 1953.
- [158] C. Sheppard and A. Choudhury, “Image formation in the scanning microscope,” *Optica Acta: International Journal of Optics*, vol. 24, no. 10, pp. 1051–1073, 1977.
- [159] X. Fan, J. J. Healy, and B. M. Hennelly, “Investigation of sparsity metrics for autofocusing in digital holographic microscopy,” *Optical Engineering*, vol. 56, no. 5, p. 053112, 2017.
- [160] L. Tian, J. Wang, and L. Waller, “3d differential phase-contrast microscopy with computational illumination using an led array,” *Optics letters*, vol. 39, no. 5, pp. 1326–1329, 2014.
- [161] Z. F. Phillips, M. Chen, and L. Waller, “Single-shot quantitative phase microscopy with color-multiplexed differential phase contrast (cdpc),” *PloS one*, vol. 12, no. 2, p. e0171228, 2017.
- [162] L. Ahrenberg, A. J. Page, B. M. Hennelly, J. B. McDonald, and T. J. Naughton, “Using commodity graphics hardware for real-time digital hologram view-reconstruction,” *Journal of display technology*, vol. 5, no. 4, pp. 111–119, 2009.

